Digital hologram recording systems: some performance improvements

Nitesh Pandey

Department of Computer Science

National University of Ireland, Maynooth

A thesis submitted for the degree of

PhilosophiæDoctor (PhD)

2011 June

1. Reviewer: Dr.Giancarlo Pedrini

2. Reviewer: Dr. Charles Markham

Day of the defense:

Signature from head of PhD committee:

Abstract

The work presented in this thesis was performed under the EU's Framework 7 (FP7) project, 'REAL3D'. The aim of this project is to develop methods based on digital holography for real time capture and display of 3D objects. This thesis forms a small subset of all the work done in this project. Much of the research work was aimed towards fulfilling our part of the requirements of the REAL3D project. The central theme of the research presented in this thesis is that of improving the performance of the digital holographic imaging system for its use in 3D display. This encompasses research into speed up of reconstruction algorithms, understanding the influence of noise and developing techniques to increase resolution and angular perspective range in reconstructions.

The main original contributions of this research work presented in this thesis are:

- **A computer-interfaced automatic digital holographic imaging system employing 'phase shifting' has been built.** This system is capable of recording high-quality digital holograms of a real world 3D object. The object can be rotated on a rotational stage and a full 360° range of perspectives can be recorded. Speckle reduction using moving diffusers can be performed to improve the image quality of the reconstructed images. A LabView based user friendly interface has been developed.
- **Novel methods based on space-time tradeoff and fixed point arithmetic have been developed and implemented for speeding up the reconstruction algorithm** used in digital holography. This has resulted in the publication of one peer-reviewed journal publication and one conference proceeding [1, 2].

- **The influence of additive noise, particularly quantization noise in digital holography has been studied in detail.** A model has been developed to understand the influence of noise on the reconstructed image quality. Based on this model, a method has been developed to suppress quantization noise in a memory efficient manner. This work led to the publication of two peer-reviewed journal publications [3, 4].
- **A novel method of removing the twin image has been developed.**
- **Methods to increase the perspectives in holography based on synthetic aperture have been implemented.**

Apart from these primary contributions, the author of this thesis has also contributed in the form of assisting in experiments, creating figures for various papers, writing computer programs and discussions during group meetings. In total, 6 peer-reviewed journal papers (3 being primary author) have been published and 6 conference proceedings (3 being primary author) have been published. Additionally, 2 talks have been given at international conferences.

To my family

Acknowledgements

I am obliged to my supervisor, Bryan Hennelly, for his constant support, guidance, encouragement and for all the fruitful discussions we had during the course of this project.

I am also indebted to the staff of the Dept. of Computer science especially Charles Markham, John McDonald and Adam Winstanley for their support.

I sincerely thank John Sherdian and Tom Naughton for their encouragement and advice.

The research leading to these results has received funding from the European Community's Seventh Framework Programme FP7/2007-2013 under grant agreement no. 216105 and also Science Foundation Ireland under the National Development Plan.

Contents

List of Figures

List of Tables

1

Introduction

Three dimensional capture and display of images and objects is widely expected to be the next revolution in display technology. The human visual system interprets the third dimension of depth in images using both physiological and psychological depth cues [5]. These include binocular parallax, monocular movement parallax, accommodation and convergence. The most important depth cue is that of binocular parallax and this refers to seeing a different image of the same object with each eye. It was first investigated by Wheatstone [6] in the 1830's. He was the first to explain the principles of stereo-vision and invented a stereo-viewer, an apparatus to see images in 3D. Using this instrument, he was able to scientifically establish the relationship between binocular parallax and depth perception. Wheatstone's apparatus was also arguably the world's first 3D display device. The second half of the 19th century saw several remarkable developments in the field of photography and techniques for perceiving depth in images. In 1850, Brewster perfected the stereoscope [7] and adapted it to stereo-photography and by 1853, Rollmann [8] had shown a method to make anaglyph images for stereoscopy. In 1861, the first colour photograph, was shown by Maxwell [9, 10] in a lecture to the Royal Society of Great Britain. By 1862, du Hauron and Cros working independently had demonstrated several methods for making three colour anaglyph photographs [11]. Important contributions were made by Lippmann [12, 13] in 1891 through the development of a interference based color photography technique for accurate reproduction of the color. Lippmann also developed concepts for three-dimensional display based on integral imaging. For the development of the interference based color photography method, Lippman was awarded the Nobel prize in 1908. The Eastman Kodak Company was founded by Eastman in 1892 and led to the development and commercialization of many new photographic films and simplified cameras [14]. Various advances have since been made in the area of photography and stereoscopy and today the most popular technology for generating a 3D effect is still based on achieving binocular parallax using stereoscopy. Variations of the stereoscopic technique include colour (or polarization) coded (anaglyphic) displays in which each perspective is encoded with a different color or polarization, interlaced displays or shutter-glasses which block one eye at the time and are synchronized with a high frame rate display give a 3D impression to the observer. For further information on the many variations of stereoscopy and other 3D display techniques, the reader is referred to [15, 16, 17, 18, 19] and the references within. Stereoscopy based 3D display however has a number of disadvantages [20]. Eye-wear is cumbersome for many viewers and the synthesized binocular parallax creates a mismatch between the various depth cues in human perception. This causes discomfort to many viewers. Thus there is an increasing need to have a 'real 3D', eye-wear free display technology. It is here that holography based techniques have shown a strong prospect.

The technique of holography was invented by Gabor in the late 1940's [21] when he was trying to improve the resolution of the electron microscope. He was awarded the Nobel prize in physics in 1971 for this invention. However, widespread application of this technique required coherent light sources and thus it did not become practically feasible until the invention of the laser in 1960. Gabor's original technique was an in-line recording technique in which weakly scattered light from a transmissive object was made to interfere with the strong reference wave. The interference pattern contains both the amplitude and phase of the object. This idea has found immense modern applications in x-ray imaging of crystallographic structure [22, 23], electron microscopy [24] and gamma ray holography [25, 26].

The reconstructed image from the in-line architecture was noisy due to the presence of the twin image of the object. The twin-image was and still is a classical problem in holographic imaging and several methods were proposed to eliminate or suppress it in the reconstruction. In 1951, Bragg and Rogers developed a solution to subtract the twin image by recording a conjugated second hologram of the object at twice the distance from the first[27]. Related subtraction based techniques were reported in the late 1950s in the works of Kirkpatrick and El-Sum [28]. However these techniques relied on more than one recording and were not easy to implement. The reader is referred to a review of the various developments regarding twin-image reduction in holography Hennelly et al. [29].

An important breakthrough in holography came in the form of the off-axis recording technique developed in 1960s by Leith and Upatnieks [30] and Lohmann [31]. This technique was the result of looking at holography and interferometry as an 'enterprise in optical information processing' [32]. The off-axis technique led to the complete separation of the twin image and the object image in the reconstructions and led to developments in the field of color display holography through the works of Leith and Upatnieks [33], Mandel [34] and Pennington and Lin [35]. Particularly important developments were the Denisyuk method of recording white light viewable reflection holograms [36] and Benton's rainbow holograms [37] which could be mass produced using hot stamping. These developments made holography popular as an art form and among the general public.

The inter-disciplinary approach to holography coupled with advances in coherent light sources and photosensitive materials such as photographic films [38, 39], photopolymers [40], photorefracrive crystals [41] and even light sensitive bacteria [42] led to the revivial of holography and fields such as display holography and optical information processing. The development of powerful digital computers and high resolution printing led to the field of computer generated holograms and digital recording of holograms. Goodman and Lawrence [43], Konrod et.al [44] and Yaroslavskii [45] were among the first to propose the idea of recording and reconstructing holograms digitally. With the development and subsequent cost reduction of high resolution CCD (charge coupled device) technology, this idea was further developed by Schnars and Juptner [46].

Today holography has become a wide spread discipline of modern optics and finds many practical applications like fabrication of optical elements [47], holographic data storage [48], optical computation [49], non-destructive testing of materials [50, 51], 3D shape measurement [52], phase contrast microscopy [53, 54] and 3D display [18] to name a few. Display devices using some form of holography have been around since 1980s and the reader is referred to [55, 56] for a review on holographic displays. The work presented in this thesis deals with digital holography for recording and display of real world 3D objects. This was done as a part of the FP7 project, 'REAL3D'. The aim of this project was to investigate the potential of technologies based on digital holography for the purpose of 3D display. In this context, it is interesting to note that Gabor had already envisioned the possibility of the holographic technique to record 3D objects. In the conclusion of his 1949 paper [21], he writes,

'*probably the most interesting feature of the new method for light-optical applications is the possibility of recording in one photograph the data of three-dimensional objects. In the reconstruction one plane after the other can be focused, as if the object were in position, though the disturbing effect of the parts of the object outside the sharply focused plane is stronger in coherent light than in incoherent illumination.*'

The project was funded by the European Community's Seventh Framework Programme FP7/2007-2013 under grant agreement 216105. It consisted of seven academic universities and two industrial partners. The project was sub-divided into four work packages comprising of (i) the full 360 degrees of perspectives of reflective macroscopic 3D scenes, (ii) microscopic reflective 3D scenes, (iii) transmissive or partially transmissive microscopic 3D scenes, and (iv) capture of 3D scenes at infra-red wavelengths. The work presented in this thesis was done primarily as a part of the first scenario. The journal papers [1, 3, 4, 57, 58, 59] and the conference papers [2, 60, 61] were published as part of this PhD thesis.

The outline of the thesis is as follows. We begin with a brief and concise information to the principles of interference, diffraction and holography in Chapter 2. We discuss the application of digital holography for 3D display [57]. This is followed by an introduction to digital holography and the associated numerical algorithms in Chapter 3. Here, some of the features and issues surrounding the digital holographic imaging system are discussed. The basics of imaging objects using digital holography are introduced. The idea of recording and reconstructing holograms on a digital sensor is introduced and the basic optical setup of a digital hologram interferometer is shown. The parameters effecting the resolution in the image and the size of the object to be recorded in digital holography are discussed. The fast algorithms for reconstruction which are derived by approximating the Fresnel-Kirchoff diffraction equation are explained. The various features of digital holography like the twin image, ability to refocus the image to different depths, ability to reconstruct from partial holographic data and the issue of speckle noise are explained. This is followed by a discussion on two different architectures for digital holography, Fresnel, Fourier and phase shifting digital holography and the optical reconstruction of digital holograms. An investigation into the resolution limits of digital holographic imaging can be found in [58].

In Chapter 4, methods to speed up the execution time and reduce the memory usage of the reconstruction algorithms used in digital holography are discussed. The ideas of pre-computation and compression of the chirp matrices [2] and fixed point implementation [1] of the reconstruction algorithm are introduced. Lowering of memory usage in digital holography directly leads us to a detailed study of the influence of quantization noise [3] in Chapter 5. A model is developed for the influence of quantization noise on the reconstructed image and experimentally verify it. The same ideas are extended to study the influence of shot noise [4]. In Chapter 6, the observations made regarding the nature of quantization noise are used to implement noise reduction techniques to improve the image quality [59]. Memory efficient noise reduction techniques [61] and a novel method to remove the twin image from inline-Fresnel holograms are implemented. Finally Chapter 7 discusses the concept of synthetic aperture in optical imaging and implement a two different methods of synthesis of a bigger aperture in digital holography.

2

Scalar Diffraction, Fresnel transform and holography

2.1 Introduction

The aim of this chapter is to introduce and summarize the concepts of interference, scalar diffraction and holography. These concepts are important to gain a complete picture of digital holography. This chapter begins with an introduction to Scalar diffraction theory in Section 2.2 where we briefly describe diffraction and interference of light. This leads us to a discussion of the Fresnel transform in Section 2.3. We then conclude this chapter with an introduction to Holography in Section 2.4.

2.2 Scalar Diffraction

Diffraction is observed in the shadow of an obstacle when coherent light is blocked by it. In such a case, there is no sharp shadow but some fringes are observed around the edges. It is also observed when coherent light travels through a (partially) transmissive object that affects the phase of the field. Physically, this is a manifestation of the wave nature of light. It becomes more pronounced when the obstacle's size is comparable to the wavelength of light. Diffraction is an important tool for studying the geometry of microscopic and nanoscopic objects. For example, the double helix structure of DNA was discovered by studying the pattern of diffraction of X-rays by the nucleic acid polymer. The phenomenon of diffraction was first observed and published by Grimaldi in 1665 [62]. Based on this and the ideas of Robert Hooke, Huygens proposed the wave nature of light in 1678. From this hypothesis, Huygens deduced the laws of reflection and refraction, explained the phenomenon of birefringence in calcite crystal and did experimental studies on polarization. The wave theory of light received further impetus through the introduction of the concept of interference by Young's double slit experiment [63]. In 1818, Fresnel brought together these concepts and derived the expressions to calculate diffraction patterns from simple shapes accurately. A significant advance in the study of wave nature of light was the establishment of the electromagnetic nature of light by Maxwell in 1860 [64, 65, 66]. This led to a refined versions of the Huygens-Fresnel principle in the form of the Fresnel-Kirchoff diffraction formula and the Rayleigh-Sommerfeld diffraction integral.

Light can be described both as an electromagnetic wave or as a stream of particles called photons. This duality of light [67] is necessary to explain the various experimentally observed phenomena of light. For example, the interaction of light with matter at the atomic scale, like the photoelectric effect, is suitably described by considering the photon nature of light. Phenomena like refraction, diffraction, interference are explained by a wave nature of light which is based on the theory of classical electromagnetism formulated by J.C Maxwell . The phenomenon of diffraction can lead to some interesting observations like the Poisson spot (a bright spot in the center of a circular obstacle or a dark spot in the center of a circular aperture Fig. 2.1).

The wave equation which can be derived from the Maxwell's equations lead to the description of the electric field of a propagating light wave.

$$\nabla^2 \vec{E} - \frac{1}{c^2}\frac{\partial^2 \vec{E}}{\partial t^2} = 0 \tag{2.1}$$

Here $\vec{E}$ is the electric field vector and ∇^2 is the Laplacian operator and c is the speed of light in vacuum and t is the time parameter. In the case of linearly polarized light, the electric field vibrates only in one plane perpendicular to the propagation direction and the wave equation reduces to the scalar wave equation

$$\frac{\partial^2 E}{\partial z^2} - \frac{1}{c^2}\frac{\partial^2 E}{\partial t^2} = 0 \tag{2.2}$$

which gives a linearly polarized, harmonic plane wave as a solution.

$$E(x, y, z, t) = a \exp[i(\omega t - \vec{k}\vec{r} - \phi)] \tag{2.3}$$

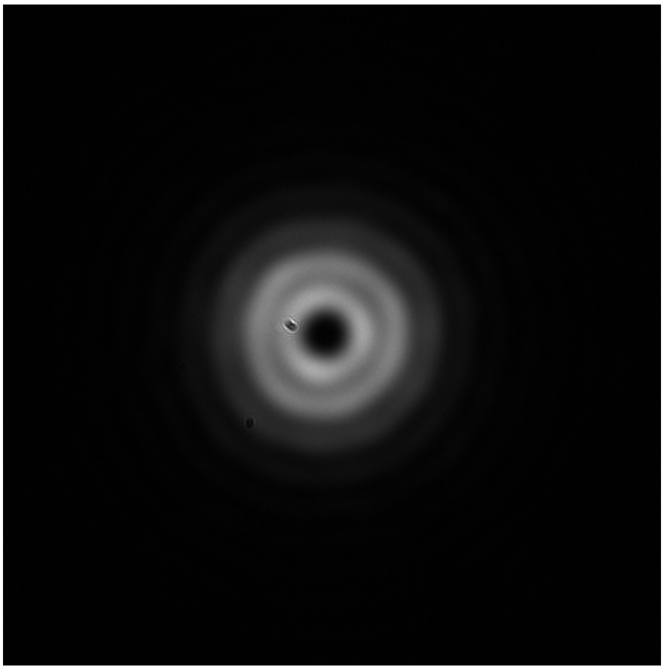

Figure 2.1: Diffraction pattern showing the Poisson spot. A dark spot was observed in the center of an open aperture.

$E(x, y, z, t)$ is the modulus of the electrical field vector at the point with the spatial vector $\vec{r} = (x, y, z)$ at the time t. i is defined as $\sqrt{(}-1)$. The physical wave is represented in the real part of Equation 2.3. The quantity a is the amplitude and $\vec{k}$ represents the propagation direction of the wave. The wavenumber is the modulus of the propagation vector $\vec{k}$

$$|\vec{k}| = \frac{2\pi}{\lambda} \tag{2.4}$$

The angular frequency ω, the frequency f of the light and the wavelength, λ are related by the speed of light c as

$$\omega = 2\pi f \tag{2.5}$$

and

$$c = \lambda f \tag{2.6}$$

The visible light occupies a wavelength range from 380nm to 780nm which corresponds to a frequency of 7.5×10^{14}Hz to 3.8×10^{14}Hz. This is an extremely fast variation of the electric field and cannot be directly measured by any currently available device.

Light sensors such as photographic film, CCD chips etc respond only to the the intensity of light which is the time-average of the square of the electric field. Moreover, in many applications, the spatial distribution of the electric field is of interest and we can ignore the time varying part and consider only the spatial part of the complex wave. The plane wave can then be represented as

$$E = Aexp(i\vec{k}.\vec{r}) \tag{2.7}$$

Using this representation of the spatially varying electric field, we can study the phenomenon of interference and diffraction. Interference refers to the superposition of two or more mutually coherent light waves and is one of the most important consequence of the wave nature of light. The phenomenon of interference was first studied by T.Young [63]. When such a superposition occurs, the electric field at any point is the vector sum of all the individual fields due to all the interfering waves. We consider here the simplest case of interference between two plane waves.

Let $W_1 = A_1 \exp(i\vec{k_1}.\vec{r})$ and $W_2 = A_2 \exp(i\vec{k_2}.\vec{r})$ represent the two plane waves with amplitudes A_1 and A_2 respectively and angle θ between them. If these two plane waves are superimposed on each other in space, the net intensity of the superimposition can be written as

$$I = A_1^2 + A_2^2 + A_1 \exp(i\vec{k_1}.\vec{r}) A_2^* \exp(-i\vec{k_2}.\vec{r}) + A_1^* \exp(-i\vec{k_1}.\vec{r}) A_2 \exp(i\vec{k_2}.\vec{r}) \tag{2.8}$$

Since A_1 and A_2 are real, this can be simplified to

$$I = A_1^2 + A_2^2 + 2A_1A_2 \cos(|(\vec{k_1} - \vec{k_2}).\vec{r}|) \tag{2.9}$$

The third term in the resulting intensity pattern represents a sinusoidal modulation in space and is the interference fringe pattern. The 'grating vector' is $\vec{k} = \vec{k_1} - \vec{k_2}$ and the spatial frequency of the fringes is

$$|k| = |\vec{k_1} - \vec{k_2}| = \frac{2\pi}{\wedge} \tag{2.10}$$

and

$$\wedge = \frac{\lambda}{2\sin(\frac{\theta}{2})} \tag{2.11}$$

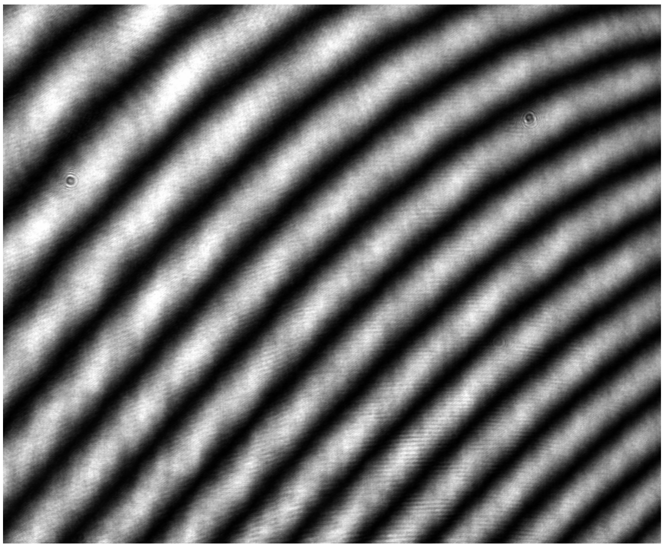

Figure 2.2: Experimentally obtained interference fringes between two plane waves

where $\wedge$ is the spatial freuqnecy.

Fig. 2.2 shows the interference fringes obtained in our experimental setup which is described in Chapter 3. To observe a stable interference pattern, however, the interfering waves must be mutually coherent with one another. Coherence of light can be classified into a spatial and temporal nature. Spatial coherence relates to the finite spatial extent of the light source while temporal coherence is related to the finite bandwidth of the source. A detailed analysis of coherence of light is beyond the scope of this thesis and can be found in [68].

2.3 Fresnel transform

The Huygens-Fresnel principle of diffraction states that every unobstructed point on the wavefront of the light wave at any instance acts as a source of spherical wavelets in both amplitude and phase. The amplitude of the optical fields is then the superposition of all these wavelets in both amplitude and phase [69]. The Huygen's principle however allows the secondary wavelets to propagate not only in the forward direction but also in the direction backward to the source. This issue is taken care of in the Fresnel-Kirchoff integral by the introduction of an obliquity term, Q which allows for propagation only in the forward direction. The Fresnel-Kirchoff integral relates the amplitude at a point

(ξ, η) in the $x^{'}, y^{'}$ plane to the amplitude distribution in the (x, y) plane [46, 70].

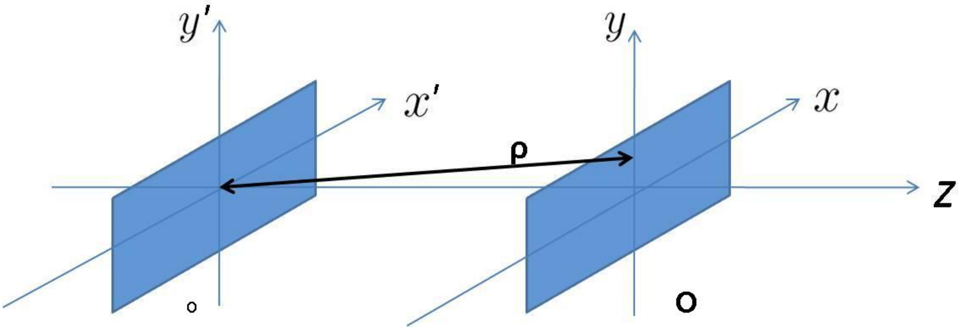

Figure 2.3: Co-ordinate system for the Fresnel-Kirchoff diffraction model between two planes $(x^{'}, y^{'})$ and (x, y)

$$o(\xi, \eta) = \frac{i}{\lambda} \int_{-\infty}^{\infty} \int_{-\infty}^{\infty} O(x, y) Q \frac{1}{\rho} \exp\left(\frac{-i2\pi\rho}{\lambda}\right) dxdy \tag{2.12}$$

where λ is the wavelength and ρ is the distance between For the purposes of digital holography, Q is effectively 1 [46] (more information about the obliquity factor Q, can be found in [62])and Equation 2.12 can be written as

$$o(\xi, \eta) = \frac{i}{\lambda} \int_{-\infty}^{\infty} \int_{-\infty}^{\infty} O(x, y) \frac{1}{\rho} \exp\left(\frac{-i2\pi\rho}{\lambda}\right) dxdy \tag{2.13}$$

ρ can be written as

$$\rho = \sqrt{(x - \xi)^2 + (y - \eta)^2 + z^2} \tag{2.14}$$

The distance, z at which the object is placed is typically order of magnitude or more larger than ξ and η. We can thus use the approximation $(1 + x)^{\frac{1}{2}} \approx 1 + \frac{x}{2}$ to write ρ as

$$\rho = z \left[1 + \frac{(x - \xi)^2 + (y - \eta)^2}{z^2}\right]^{\frac{1}{2}} \tag{2.15}$$

By substituting the value of ρ and approximating the denominator as z, we arrive at the Fresnel transform.

$$\rho = z + \frac{(x - \xi)^2 + (y - \eta)^2}{2z} \tag{2.16}$$

$$o(\xi, \eta) = \frac{i}{\lambda} \int_{-\infty}^{\infty} \int_{-\infty}^{\infty} O(x, y) exp \left\{ \frac{-i2\pi}{\lambda} [z + \frac{(x - \xi)^2 + (y - \eta)^2}{2z}] \right\} \frac{1}{z} \tag{2.17}$$

By expanding ρ in Equation 2.16 and substituting in Equation 2.17, we arrive the equation

$$o(\xi,\eta) = \frac{i}{\lambda z}\exp\left(-i\frac{\pi}{\lambda z}(\xi^2+\eta^2)\right)$$
$$\int_{-\infty}^{\infty}\int_{-\infty}^{\infty} O(x,y)\exp\left[-i\frac{\pi}{\lambda z}(x^2+y^2)\right]\exp\left(i\frac{2\pi}{\lambda z}(x\xi+y\eta)\right)dxdy \tag{2.18}$$

This is called the Fresnel transform and it describes the propagation between two planes (x,y), the hologram and the reconstruction plane, $(x^{'},y^{'})$. As it can be seen, the Fresnel transform of the hologram $O(x,y)$ is obtained by first multiplying it by a quadratic phase factor and then taking a Fourier transform of the result. In practical digital holography we sample the propagated field using a digital camera and thus we routinely deal with a discrete version of the Fresnel Transform. This is discussed in more detail in chapter 3.

2.4 Holography

An interference pattern between two plane waves resulting is straight fringes can be considered to be the simplest hologram. In general however, a hologram refers to the interference pattern between the light scattered by a 3D object and a mutually coherent reference beam. The amplitude and phase information is encoded in the fringe structure of the hologram and can be recovered and used for many applications. Mathematically the concept of mapping the phase variation to intensity variations can be understood if we consider two wavefields given by $O\exp[i\phi_O(x,y)]$ and $R(x,y)\exp[i\phi_R(x,y)]$ where $O(x,y)$ is the amplitude and $\phi_o(x,y)$ is the phase distribution of the light reflected/transmitted from an object, $R(x,y)$ and $\phi_R(x,y)$ are the reference wave's amplitude and phase distribution respectively. The intensity distribution in the hologram formed by interference of these two waves is given by

$$H(x,y) = |O(x,y)+R(x,y)|^2 \tag{2.19}$$

$$H(x,y) = [O(x,y)+R(x,y)][O(x,y)+R(x,y)]^* \tag{2.20}$$

$$H(x,y) = O(x,y)O^*(x,y)+R(x,y)R^*(x,y)+O(x,y)R^*(x,y)+O^*(x,y)R(x,y) \tag{2.21}$$

$$H(x,y) = |O(x,y)|^2 + |R(x,y)|^2 + O(x,y)R^*(x,y) + O^*(x,y)R(x,y) \tag{2.22}$$

$$h(x,y) = |O(x,y)|^2 + |R(x,y)|^2 + 2O(x,y)R(x,y)\cos[\phi_o(x,y) - \phi_r(x,y)] \tag{2.23}$$

The last equation in the above series is the fundamental equation of holography. It can be rewritten in terms of the phase and amplitude of the reference and object wavefields as follows. If the reference wave is a plane wave and is incident in-line with the recording plane, i.e the propagation vector of the plane wave is perpendicular to the recording plane, then we can consider $R(x,y)$ to be a constant, $r(x,y) = r$ and $\phi_r(x,y) = 0$. The hologram then becomes

$$h(x,y) = |O(x,y)|^2 + |R|^2 + 2O(x,y)R\cos[\phi_o(x,y)] \tag{2.24}$$

$$h(x,y) = |O(x,y)|^2 + |R|^2 + RO(x,y)\exp[i\phi_O(x,y)] + RO(x,y)\exp[-i\phi_o(x,y)] \tag{2.25}$$

It can be seen from this equation the third term contains $O(x,y)\exp[i\phi_O(x,y)]$ which is the complex object wave. Thus the hologram contains the complex object wave and both the amplitude and phase of the object are recorded. However, there are three additional terms namely, $|O(x,y)|^2$, $|R|^2$ which are the zero-order terms and $RO(x,y)\exp[-i\phi_O(x,y)]$ which is the classical twin-image in holography. The twin image is discussed in more detail in Chapter 3.

These terms are unwanted and one of the major turning points in holography was the development of the 'off-axis technique' to separate these terms by Leith and Upatnieks. This technique made it possible to record high quality holograms of 3D objects. Gabor's original technique involved the use of a point source to illuminate a weakly modulated transparent object and the weakly scattered signal interferes with the strong background signal. As a result, four terms are created, the object intensity term (which is weak by nature of the object) the reference intensity and the two interference terms. These two interference terms overlie each other and when the object wavefield is 'replayed' it is marred by the presence of the out of focus twin image. In the off-axis technique, the reference beam is made to interfere at an angle so as to induce a linear phase shift in the terms and hence a spatial separation of the object and twin image in the reconstruction . In off axis Fresnel holography the DC and twin terms are separated by using a reference wave that is incident at a small angle θ. We can describe the reference to be defined as follows

$$r(x,y) = \exp\left\{(i\frac{2\pi}{\lambda}[xsin(\theta_x) + ysin(\theta_y)]\right\} \tag{2.26}$$

There are now many variations of making holograms. The reader is referred to chapter 9 in [62] and the references within for more information.

2.5 Conclusion

We discussed the concepts of diffraction and interference which are critical in the field of holography. We also dicussed the Fresnel transform which relates the diffracting complex fields between two planes under the paraxial approximation. We showed the derivation of the Fresnel transform from the Huygens-Fresnel principle. In the next chapter, we apply these concepts to the area of digital holography. Some other features of holography such as the twin image and the different recording architectures are also discussed in the next chapter.

3

Digital holographic imaging

3.1 Introduction

In this chapter, the basics of imaging objects using digital holography are introduced. In Section 3.2, the optical setup of a digital hologram interferometer, the parameters effecting the resolution in the image and the size of the object that can be recorded in digital holography are discussed. In Section 3.3, fast algorithms for reconstruction are derived by numerically approximating the Fresnel-Kirchoff diffraction equation. The direct method and the convolutional method of reconstruction are explained. Section 3.4 deals with the various features of digital holography like the twin image, the capability to refocus the image to different depths, the capability to reconstruct from partial holographic data and also the issue of speckle noise. This is followed in Section 3.5 by a discussion on the different architectures for digital holography that were employed in the work on this thesis, Fresnel, Fourier and phase shifting digital holography. The chapter is concluded by discussing the optical reconstruction of digital holograms in Section 3.6.

3.2 Recording of digital holograms

In digital holography, a coherent reference wave is incident on a 2D image sensor where it forms an interference pattern with coherent light reflected from or transmitted through an object of interest. The resulting interference pattern, called the digital hologram (DH), contains encoded information about the 3D topographic features of the object. The basic concept of digital holography can be understood from the two figures, Fig. 3.1 and, Fig. 3.2. Fig. 3.1 shows a simple conventional single lens imaging system where the object is in front of lens and an image is formed which an be recorded or viewed. Such one lens imaging systems are well understood [70] and they serve as a good starting point for understanding digital holographic systems. One lens imaging systems as shown in Fig. 3.1 require that the object lens distance z_1, the lens image distance z_2, and the lens focal length f, can be related by the classical lens law of geometrical optics (i.e. $1/z_1 + 1/z_2 = 1/f$). If this is the case we can expect an image of the object at a plane z_1 in front of the lens to be produced at a plane z_2 behind the lens. The image will have a magnification of $-z_2/z_1$ where the minus indicates that the image will be inverted. If we wanted to focus on a different plane, i.e. a different z_1 (as might be the case in scanning a 3D object) we would have to change either or both the values of f or z_2 which would require physical changes to the imaging system. We note that with one lens imaging systems the image that is produced in the image plane is not 'ideal' in the sense that there exists a residual quadratic phase factor ('chirp') overlying the image. This phase factor is not observed by intensity sensitive materials and is therefore never a factor of consideration in one lens imaging systems. Fig. 3.2 shows a digital holographic imaging system where the object is indirectly imaged by recording a hologram.

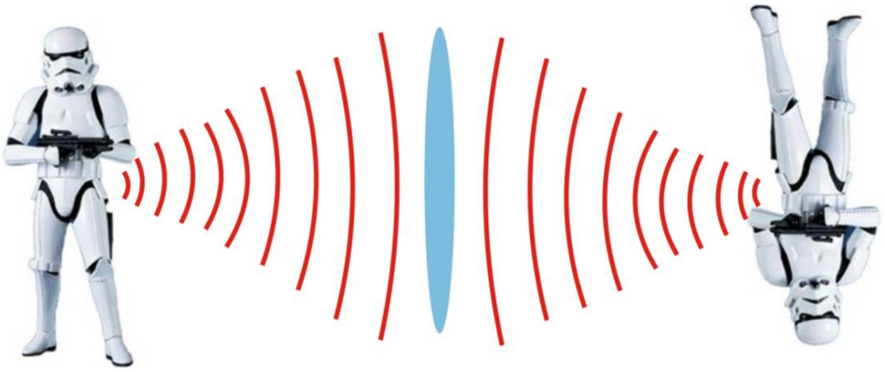

Figure 3.1: Conventional single lens imaging

The object is placed in front of a 2D image sensor array and is illuminated with a coherent beam of light. The scattered radiation is then made to interfere with a mutually coherent reference beam and a hologram is recorded. This digital hologram contains the complex object information along with the zero order scattered light and the twin image term. The digital hologram is then input to a numerical algorithm

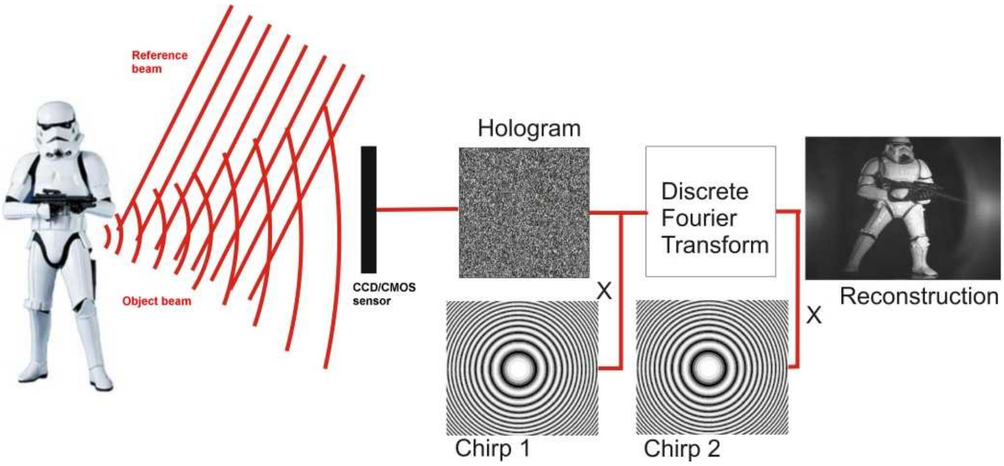

Figure 3.2: Digital holographic imaging

which calculates an image. We note a similarity between the one lens system in Fig. 3.1 and the DH system shown in Fig. 3.2. The first part of both systems is identical where the light that is scattered by an object is propagated through free space and passes through an aperture, a lens aperture in the first case and a camera aperture in the second. In the first case the image is produced by multiplication of the wavefront with a quadratic phase factor induced by the lens followed by free space propagation to the image plane. In the second case the image is formed by numerically simulating the free space propagation of the light backwards to get to the image plane. It can be shown that this numerical simulation is equivalent to simulating the effect of the lens and the forward propagation that exists in case 1.

It should be noted in this description of DH there is no physical lens used for the imaging part, only a ‘numerical lens’ used to create the image of the object from the hologram. In other arrangements such as digital holographic microscopy, the object information is picked up by a microscope objective and lenses are used in other parts of the optical assembly but the imaging from the hologram plane to the object plane can be done numerically without a physical lens. There are a number of noteworthy advantages to the DH system over the one lens system; Firstly we can numerically focus on an image plane without introducing any physical changes to the optical system. In fact we can do this using a single recorded digital hologram. Secondly we also obtain the phase of the image as well as the intensity. This phase information is very useful for metrology applications where we can calculate nanometer deformations of the object under investigation. An interesting aspect of the digital hologram is that it can be transmitted remotely to another place and the 3D object can be reconstructed and displayed remotely.

Fig. 3.3 shows the optical schematic of the digital holographic process.

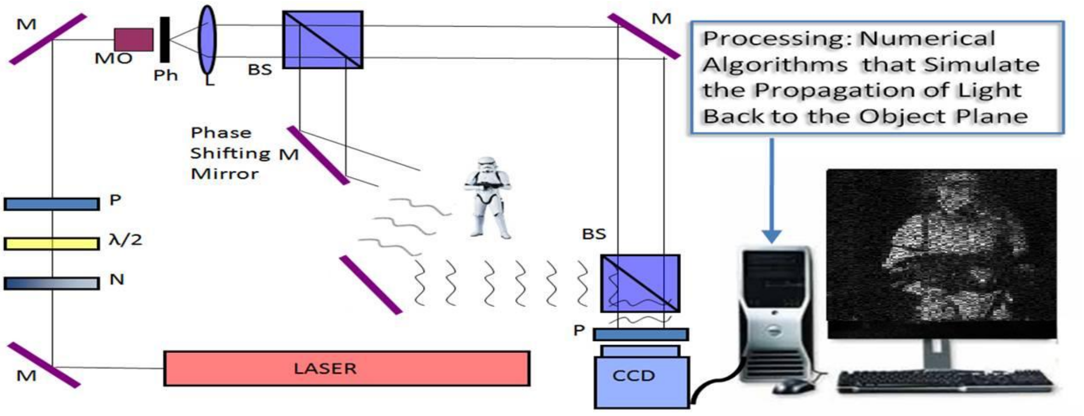

Figure 3.3: Optical setup used for digital holography. M(mirrors), N(Neutral density filter), $\lambda/2$ Half-wave plate, P(Polarizers), MO(microscope objective), Ph(pin hole), BS(beam splitter)

3.2.1 Resolution and size of the object

When a digital hologram is acquired with a discrete CCD/CMOS sensor and reconstructed digitally, at least five physical effects impact on the image formation and image quality in the reconstruction plane. They are

1. The camera aperture size which determines the point spread function of the imaging system. The aperture size controls the maximum spatial frequency recordable in the imaging system which is equal to $D/(\lambda z)$.

2. The averaging effect of the intensity over each pixel's area to one value.

3. The pixel pitch or sampling rate determines the distance between overlapping copies caused by sampling. They are separated by integer multiples of $\lambda z/T$. Pixel pitches in modern industrial cameras are in the range of 2-8μm.

4. The quantization of the pixel values. i.e. the pixel values are then quantized in accordance with the bit-depth of the memory registers in the detection system. The bit-depth in modern cameras is typically 8-12 bits per pixel.

5. Degradation of the image quality due to speckle noise.

For a detailed discussion on various parameters which effect the image quality and the resolution limits in digital holography, the reader is referred to [58, 71].

3.2.2 Experimental setup used in this thesis

The basic experimental set up used is illustrated above in Fig. 3.3. A full description of the practical implementation as well as details on the optical elements is can be found in Appendix A. Here we briefly describe a few features. We use a Mach-Zehnder interferometer employing a diode pumped solid state laser (λ=785nm) to record digital holograms. This is described in more detail in Appendix A. It was used to record holograms of numerous objects for full 360 degree range of perspectives and in different configurations like lensless Fourier and synthetic aperture. A Labview interface was developed for fully automated recording and a novel phase shift calibration algorithm was developed. These are described in Appendices B and C. Some modifications to the setup are also described in other chapters. Reconstruction of holograms recorded for the Real3D project are shown in Appendix D.

Fig. 3.5 shows a typical inline hologram captured from the setup and 3.6 shows the reconstruction which results from the direct application of the Fresnel transform on the hologram. A photograph of the object used is shown in Fig. 3.4. As it can be seen, there is a significant amount of noise present in the reconstructed image. The central rectangular block is the zero-order term and the surrounding haze of noise is the result of speckle and twin-image noise which are discussed in more detail in Section 3.4.

3.3 Reconstruction algorithms

In this section, we discuss the two most widely used methods for the implementation of the Fresnel transform for reconstructing digital holograms. An integral part of these implementations is the discrete Fourier transform (DFT). This is efficiently implemented using the Fast Fourier transform algorithm. For the moment we assume that we can

Figure 3.4: One of the objects used for recording digital holograms in this thesis. A stormtrooper figurine (approximately 5cm tall).

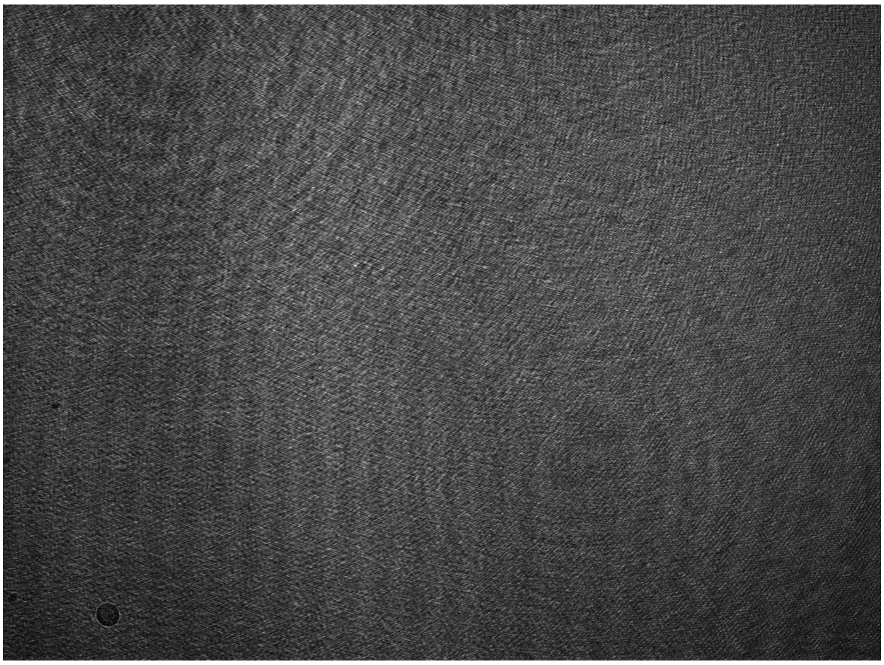

Figure 3.5: An in-line Fresnel digital hologram

Figure 3.6: Reconstruction from an in-line Fresnel digital hologram

extract the (discretised) complex object wavefield from the interference pattern, i.e. that we can remove the three unwanted terms that were discussed in Section 2.4 . We will discuss how this is done later.

The Fourier transform is used to transform a continuous signal from the time (or spatial) domain into the frequency (or spatial frequency) domain. The Fourier transform $U(f)$ of the function $f(t)$ is defined as

$$U(f) = \int_{-\infty}^{-\infty} u(x)\exp(-i2\pi fx)dx \tag{3.1}$$

The inverse fourier transform is defined as

$$u(x) = \int_{-\infty}^{-\infty} U(f)\exp(i2\pi fx)df \tag{3.2}$$

We can define an operator F for the Fourier transform and similarly F^{-1} for the inverse Fourier transform

When dealing with digital acquisitions of a continuous signal, one deals with discrete matrices and the corresponding implementation of the continuous Fourier transform is the discrete Fourier transform. For a discrete matrix, $u(nT)$ where $n = 0, 1, ...$ is the index and T is the sampling interval, the DFT is defined as

$$U(k) = \sum_{n=1}^{N-1} u(n)\exp(i2\pi kn/N) \tag{3.3}$$

The most computationally efficient method of implementing the DFT is the Fast Fourier transform. The basic version of the FFT algorithm is the original radix-2 implementation by Cooley and Tukey [72]. It is based on the Danielson-Lanczos lemma which links two $N/2$ sized FFTs to a single N size FFT. Using this, the FFT of a N size matrix can be computed in $O[N\log(N)]$ computational cycles. As we will shortly demonstrate the DFT (and therefore the FFT) play a central role in reconstructing digital holograms.

If we now consider the object signal as $u(x')$ where x' refers to the coordinate space in the object plane which is located a distance z away from the camera. For simplicity, we consider a 1-dimensional representation. In the plane of the CCD this signal is denoted by $u_z(x)$. The relationship between these two planes can be described by the Fresnel Transform, which models free space propagation of a scalar wave field under the paraxial approximation and was derived in Chapter 2. For simplicity in this section we limit ourselves to the 1D integral form which is defined below. Extension of the results to 2D is straightforward.

$$o(x) = F_z\{O(x')\}(x) = A_z \int_{-\infty}^{\infty} O(x') \exp\left[\left(j\frac{\pi}{\lambda z}\left(x - x'\right)^2\right)\right] dx' \tag{3.4}$$

where A_z is the constant phase factor $(i/\lambda z)$. The sampling of the digital camera may be accounted for by multiplying by a train of Dirac delta functionals. Thus we obtain a sampled version of $O(x)$, which we can write as $u_z(x)\sum_{n=-\infty}^{\infty}\delta(x - nT)$. We can write this in a shortened form as $O(nT)$ where $-N/2 \leq n \leq N/2 - 1$ and T is the sampling period of the camera. The reason we end up with a finite sum of delta functions is due to the finite width of the camera, and the finite number of pixels therein.

3.3.1 The Direct Method

The digital recording process allows one to obtain $O(nT)$. Discretizing the input and output variables of the Fresnel Transform, i.e. setting $x \to nT$ and $x' \to mT''$, we get

$$\begin{aligned} o(mT'') = {} & A_z \exp\left[\frac{j2\pi\left(mT''\right)^2}{\lambda z}\right] \\ & \times \sum_{n=-N/2}^{N/2-1}\left[O(nT)\exp\left[\frac{j2\pi\left(nT\right)^2}{\lambda z}\right]\right]\exp\left[\frac{-j2\pi nmTT''}{\lambda z}\right] \end{aligned} \tag{3.5}$$

Focusing on the last term in Equation 3.5, if we fix the output sampling (in the image plane) period as follows

$$T'' = \frac{\lambda z}{NT} = \frac{\lambda z}{W_{CCD}} \tag{3.6}$$

and if we interest ourselves with only a finite range of x'', (x'' denotes the image plane), where corresponding to the range of samples defined by $-N/2 \leq m \leq N/2 - 1$, then Equation 3.5 may be reduced into the form of the DFT,

$$\begin{aligned} o(mT'') &= DIRECT\left\{O(nT), T, z, \lambda\right\} = \\ & A_z \exp\left[\frac{j\pi\left(mT''\right)^2}{\lambda z}\right] DFT\left\{O(nT)\exp\left[\frac{j\pi\left(nT\right)^2}{\lambda z}\right]\right\}(mT'') \end{aligned} \tag{3.7}$$

It is very useful to have this equation in the form of the DFT because the DFT may be implemented in a computationally efficient manner ($N\log N$ computations compared with N^2) by employing an FFT algorithm. The resulting numerical algorithm, derived

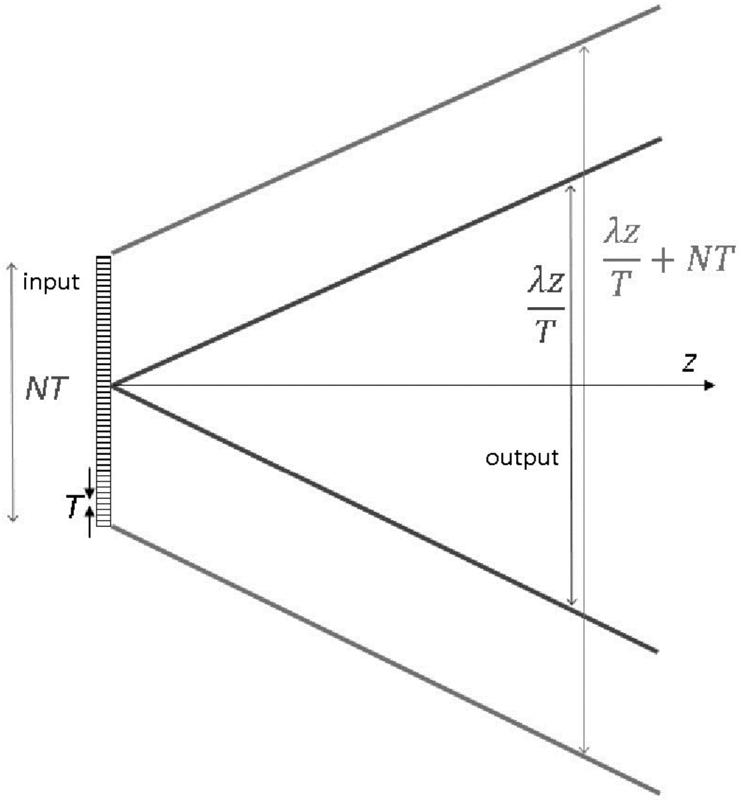

Figure 3.7: Input and Output widths of images obtained by reconstructing holograms using the direct method for simulating the Fresnel transform.

from Equation 3.7 is known as the direct method and is made up of three parts (i) multiply the hologram by a discrete quadratic phase factor; (ii) Implement the DFT using an FFT algorithm and; (iii) Multiply the result by a second discrete chirp function.

The output distribution spans a width of NT'' pixels which we can calculate to be $\frac{\lambda z}{T}$. In Fig. 3.7 we illustrate the dependence of the output reconstruction width on the distance parameter. The inner lines show the window obtained by the direct method for a range of different distances. The outer lines show the maximum possible width of a discrete signal with these characteristics using the Fresnel approximation. In Fig. 3.8 we further illustrate this point by showing the reconstructed images of digital holograms of the same object recorded at four different distances.

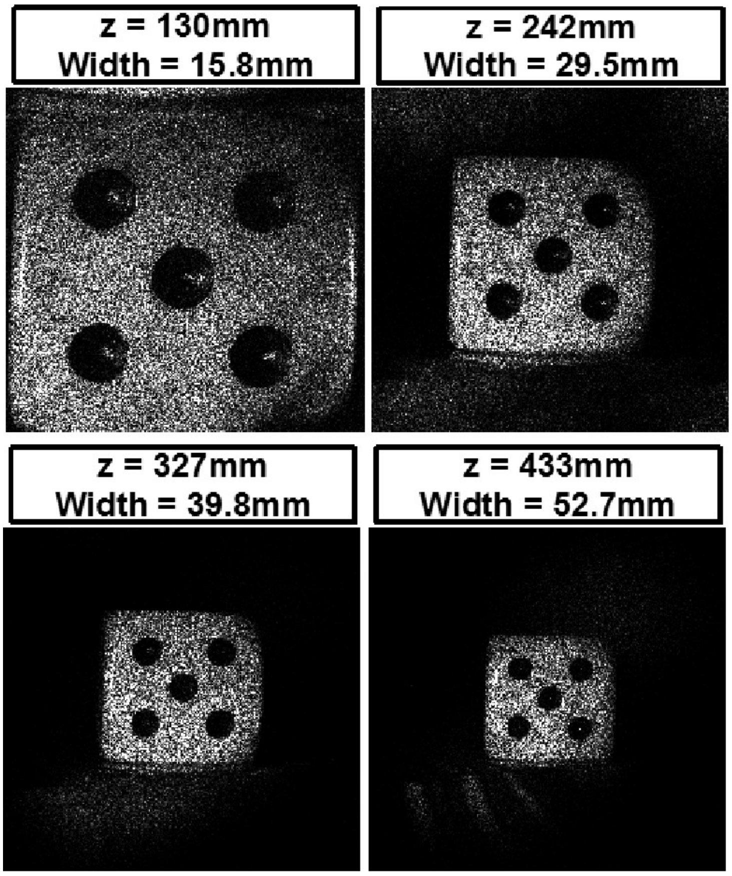

Figure 3.8: Reconstructions from direct method when the object is placed at four different distances and reconstructed using the appropriate distance from the sensor. Clearly as we increase the value for z we also increase the output reconstruction width.

3.3.2 The Spectral Method

Another method for simulating the Fresnel transform is known as the spectral method. This method is based on the fact that the Fresnel transform is a convolution and may be written as a product with a chirp function in the frequency domain. The Fresnel transform may be written as

$$o(x') = A_z F^{-1}\left\{F\left\{O(x)\exp\left(j2\pi\lambda z k^2\right)\right\}\right\} \tag{3.8}$$

where $\Im$ is the Fourier transform and transforms the signal into the frequency, k, domain and A_z is a constant. The following algorithm for simulating Fresnel transform may be derived from this expression.

$$\begin{aligned} o(mT'') = SPECTRAL\left\{O(nT), T, z, \lambda\right\} = \\ A_z IDFT\left\{DFT\left\{O(nT)\right\}\exp\left[j2\pi\lambda z\left(\frac{l}{NT}\right)^2\right]\right\} \end{aligned} \tag{3.9}$$

where the integers n, m and l all have ranges from $-N/2 \leq n, m, l \leq N/2-1$ and where IDFT represents the inverse DFT. The IDFT can also be implemented by a FFT. The result is that we obtain samples of our reconstruction with a pitch $T'' = T$. Unlike in the previous case of the direct method the output spatial width is not proportional to the reconstruction distance z and remains at a constant value of $NT'' = W_{CCD}$. In Fig. 3.9 we illustrate this point showing the constancy of the output window width from the spectral method, regardless of distance. An important point arises if the actual object size is greater than the output window width. In this case we zeropad the input hologram up to a size equal to that of the object. For the dice object used in the current experiments we have $N = 1392$, $T = 6.45\mu$ m and W_{OBJ}=1.5cm. Thus, our hologram size (and therefore our output window size) is W_{CCD}=9mm and is considerably smaller than the object size. We therefore 'zeropad' (by embedding the hologram matrix a larger matrix of zeros) our hologram up to a value of $N = 2700$ and we reconstruct this new enlarged hologram. For the sake of comparison we do this to the four holograms previously reconstructed by the direct method in Fig. 3.8 corresponding to the same object recorded at four different distances. The width in pixels is converted to units in distance by multiplication by corresponding pixel pitch in the reconstruction plane. The result is shown in Fig. 3.10. We expect to see the same output window size in all four cases. However, it is noticeable that the object appears to be different sizes in all four

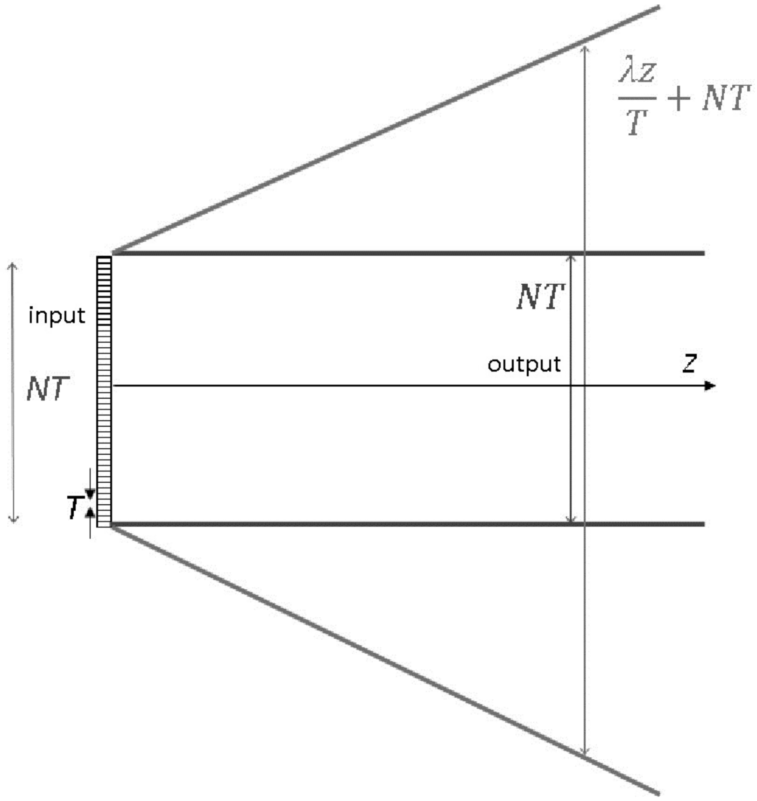

Figure 3.9: Input and Output widths of images obtained by reconstructing holograms using the spectral method for simulating the Fresnel transform.

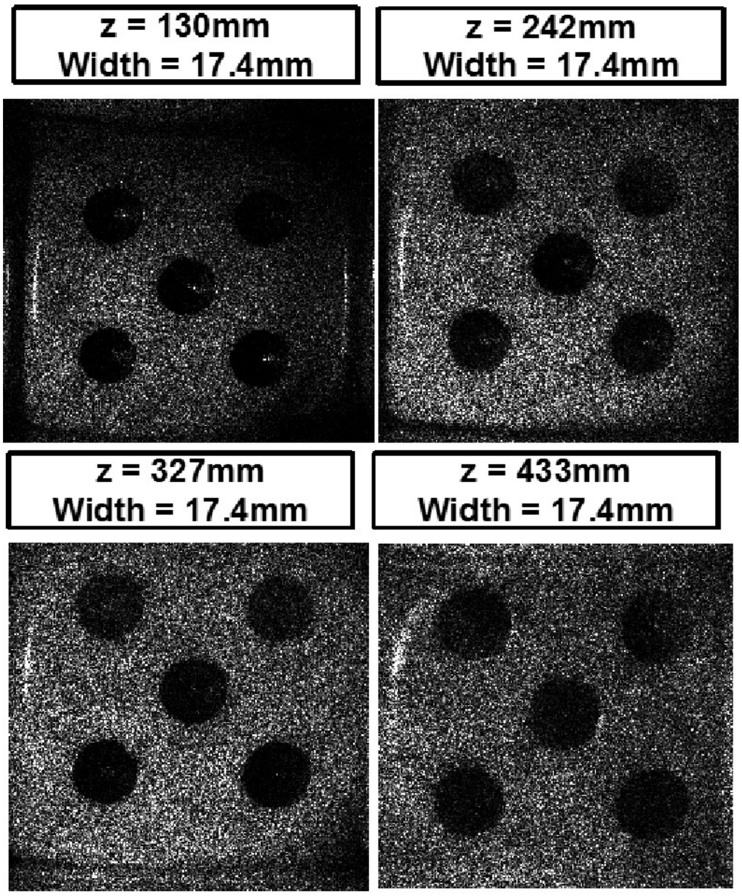

Figure 3.10: Reconstructions from spectral method when the object is placed at four different distances from the camera and reconstructed using the appropriate distance parameter..

holograms and appears to be larger for increasing recording distance. This is attributed to the presence of a slight spherical curvature on the reference beam which brings about an effective magnification in reconstruction. We now examine the impact of failing to zeropad the hologram sufficiently and we reconstruct the dice hologram (at distance z = 130 mm) for varying amounts of zeropadding. Four different reconstructions are shown in Fig. 3.11. We can see that for no zeropadding the object is not reconstructed at all. The aliased copies begin to separate out as we increase the amount of zeropadding up to the point where we have full separation when the zeropadding is sufficient to bring the effective hologram size up to that of the object. We note that increasing the number of samples in this way has a detrimental effect on the time taken to reconstruct. For this reason the direct method is often the method of choice if there is a better match between its output window width at the appropriate reconstruction distance and the physical size of the object.

3.4 Features of digital holograms

3.4.1 The zero order and the twin image

As discussed in Chapter 2, the digital hologram consists of 4 different terms. When the digital hologram is reconstructed, these 4 terms give rise to 4 different entities in the reconstruction plane. The terms due to the object and the reference give rise to the zero order in the reconstruction. The zero order term due to the reference beam is always located on the axis at the center of the reconstructed image. The two remaining terms are conjugate to each other. One term represents the object image itself and the other term is called the twin image. The twin image noise is a fundamental problem in holography and removing it from reconstructions of holograms is still a very active area of research. Leith and Upatnieks adapted a technique from synthetic aperture radar and applied it to optical holography to separate the object and the twin image spatially [30]. This was termed the off-axis technique and it involves the use of an off-axis reference beam instead of an inline one. The off-axis reference beam induces a linear phase shift in the hologram plane and thereby induces a spatial shift in the reconstruction plane. In many non-optical applications of holography such as electron holography and x-ray holography, in-line holography is still the architecture of choice due to lack of optical

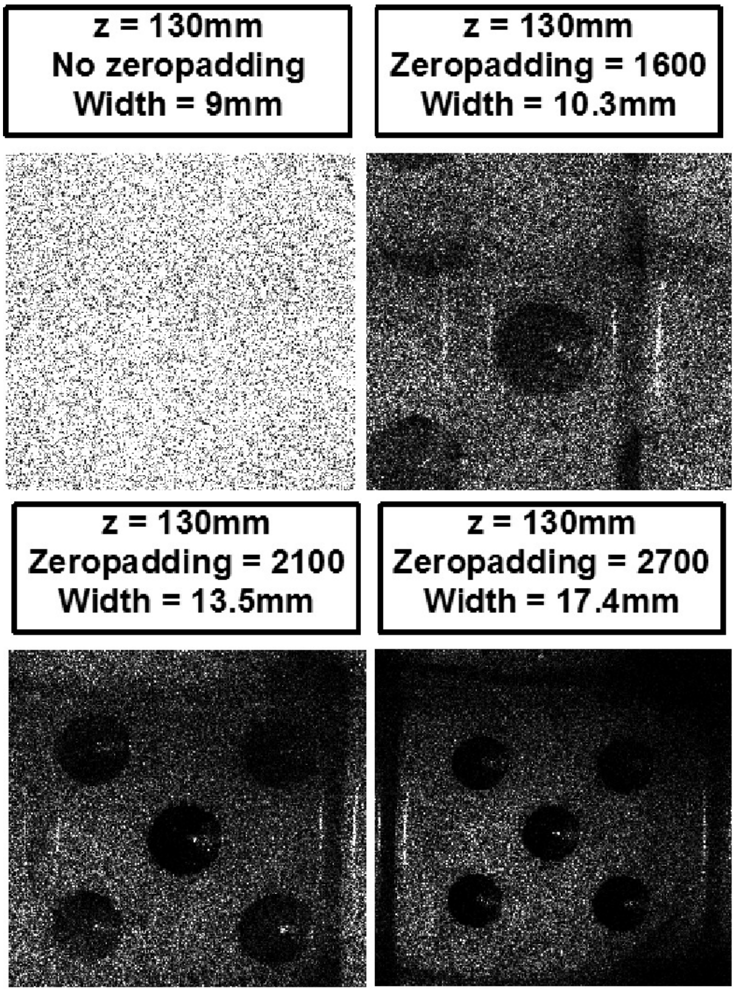

Figure 3.11: Reconstructions from spectral method using varying amounts of zeropadding.

elements to divert such beams. In the case of Fresnel in-line holography, the twin image manifests itself as an out-of focus speckle like pattern overlying the object image.

3.4.2 Numerical refocussing

In digital holography, we use a numerical lens to propagate the complex object wave and create the image. An important advantage with this is the ability to refocus the image at a different distance. Given a digital hologram and the wavelength and camera used to record it (specifically the pixel pitch), we can numerically propagate the wavefield and detect the distance at which the object comes into focus. Fig. 3.12 shows a complex hologram being propagated to 3 different planes, one of which is the right focussing plane. The correct focussing distance can be detected by using a focussing metric such as variance which is defined in Equation 3.10 where x_i are the pixel values and μ is the mean of the section of the hologram. Another metric which can be used is the energy in a high frequency region in the Fourier transform of the reconstruction intensity. This approach works on objects having sharp edges and features.

$$V = \sigma^2 = \frac{\sum_{i=1}^{N}(x_i - \mu)^2}{N} \tag{3.10}$$

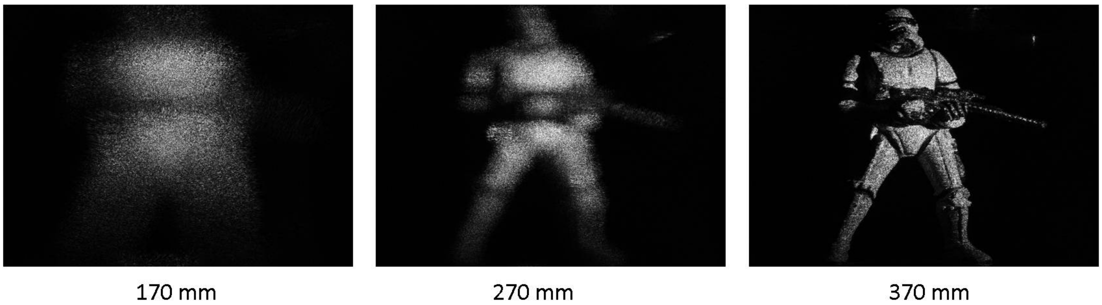
170 mm 270 mm 370 mm

Figure 3.12: Reconstruction of the digital hologram at 3 different distances. Hologram was propagated using the direct method.

When the object is in focus, the edges and the sharp features of the object stand out and cause an increase in variance or the energy of high frequencies. Fig. 3.13 shows a focussing curve using variance in the reconstructed image as a focussing metric. As it can be seen, the variance peaks when the object is sharply in focus and the correct focussing distance can be recovered. The focussing curve also reveals the depth of focus and thereby the effective numerical aperture of the system. The depth of focus typically varies as $\approx \frac{\lambda}{NA^2}$ [63]. The narrower the width of the focussing curve, the larger the aperture of the digital holographic imaging system .

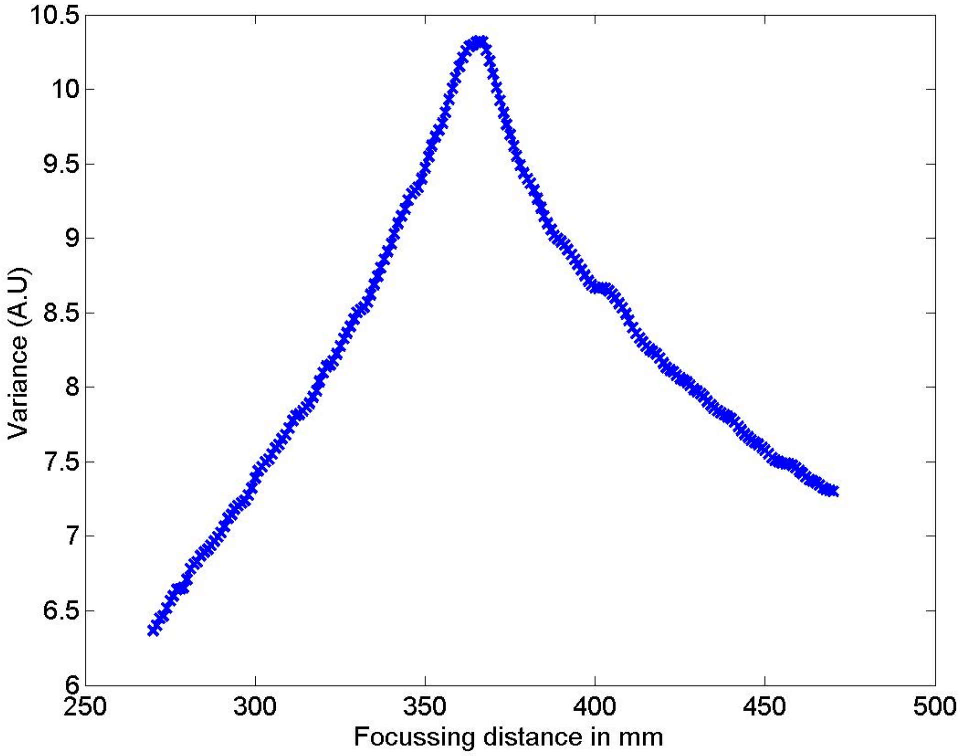

Figure 3.13: Plot of variance in a section of the reconstruction vs focussing distance. The hologram was propagated using the direct method.

3.4.3 Reconstructions from partial holographic data

An important feature of holography is the distributive nature of the holographic data. The hologram is recorded in a Fresnel transform plane where each pixel in the hologram is the result of a complex sum of all the coherent light emitted from all the points on the object. Thus the object can be reconstructed, albeit with lower resolution, with only partial data taken from the hologram. This also gives us the ability to get different view-points or perspectives of the 3D object in the reconstruction. The ability to get perspectives of the 3D object is critical for the use of digital holography in 3D display. The hologram is recorded on a sensor with finite area and each region of the sensor observes a different viewpoint of the object. Thus different perspectives can be reconstructed by isolating different areas from the hologram and reconstructing them. Fig. 3.14 shows the reconstructions obtained from two different regions from a digital hologram.

The distributive nature of the holographic data can also be seen when holograms are quantized. i.e. the number of bits used per pixel to store the information of the hologram is reduced. We see that even for highly quantized holograms, the object can be reconstructed. We show some examples in Section 3.6 and discuss this in detail in Chapter 5.

3.4.4 Speckle

Digital holographic imaging requires the use of a coherent light source. When coherent light reflects from a rough surface or is transmitted through a medium with random refractive index inhomogenities, the resulting pattern of light is called a speckle pattern. Speckle is a very important area of study in optics. As mentioned in [73], phenomenon related to speckle arise in other regions of the electromagnetic spectrum like scattering of X-rays, radar noise and scattering of electrons by carbon films. In optics, speckle is observed mainly in laser based coherent imaging and in astronomy. Techniques involving the use of speckle have many applications, a few of them being speckle interferometry [74], stellar speckle interferometry [75], testing of optical components [76], doppler vibrometry [77], etc. Speckle emanating from an object's surface carries important information about the surface properties and is thus not always a source of noise. In the case of coherent imaging of diffuse objects (as is done in digital holography), speckle tends to degrade the image quality.

The average speckle size, Δ in the reconstructed image plane[46] is given by

$$\Delta = \frac{\lambda d}{NP} = \frac{\lambda d}{W_{CCD}} \tag{3.11}$$

where W_{CCD} is the size of the detector in number of pixels and P is the pixel size and W_{CCD} is the width of the camera. There are several methods to reduce the degrading influence of speckle [78]. A very effective method to remove speckle is by using a moving diffuser. In this method, the object is illuminated with light passed

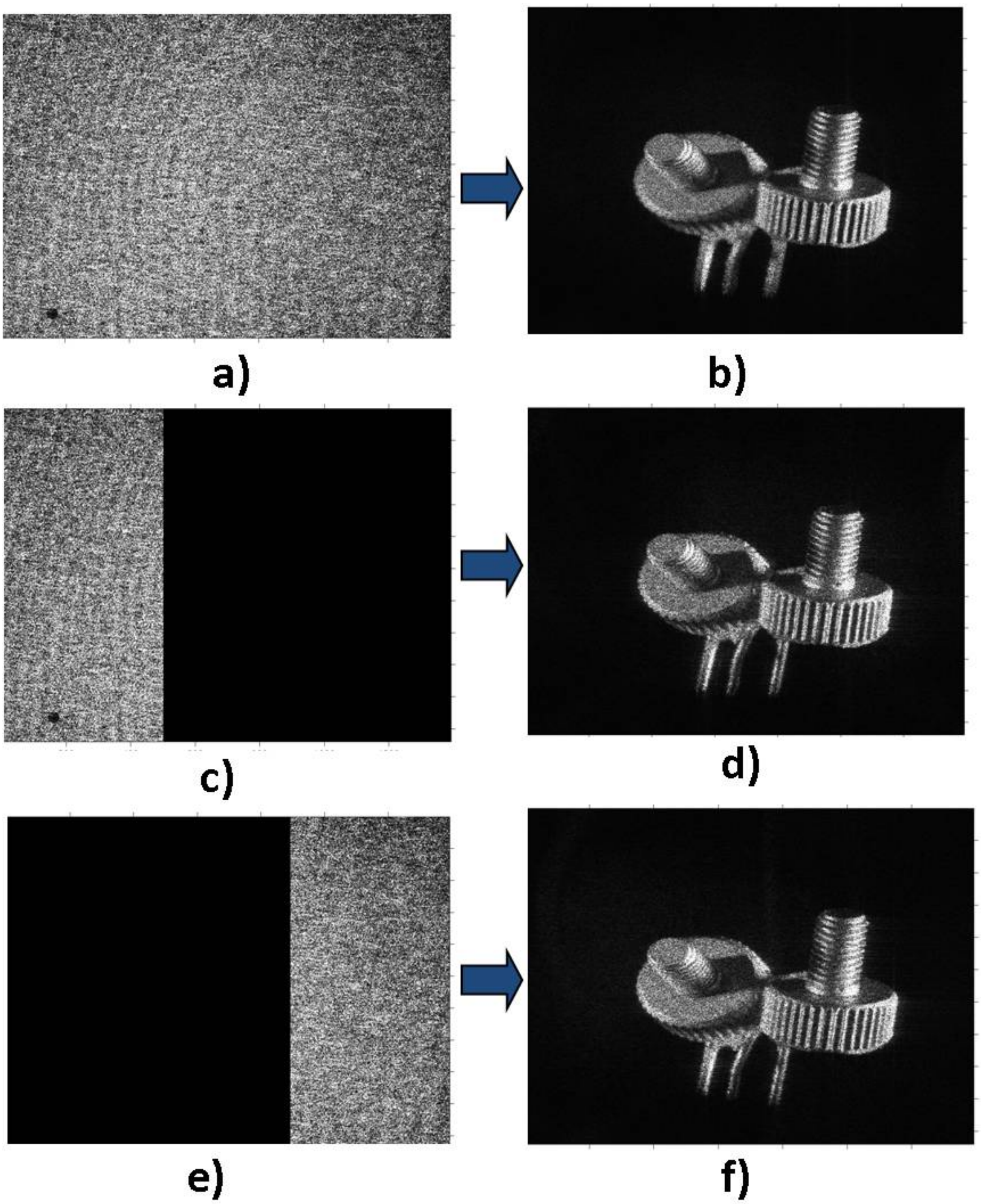

Figure 3.14: Perspectives obtained from different sections of the hologram a) shows the full reconstruction and b) and c) show the reconstructions obtained from only part of the hologram. This figure shows that the object can be reconstructed even from partial holographic data. The angular perspective in digital holography is typically 2-3 degrees and it is thus difficult to perceive in the above reconstructions.

through a diffuser. This generates a speckled image of the object. The diffuser is then moved to generate a different illumination pattern on the object and thus a different speckle pattern in the image. The different images obtained by moving the diffusers are added together [46, 73, 79, 80, 81]. The resulting image has less speckle than the original image but a lower resolution.

3.5 Architectures for digital holography

Depending on the reference beam, there can be a different architectures of a digital holographic interferometer. If the reference beam is a plane wave, then the reconstruction is obtained by a Fresnel transform. If the reference beam is a spherical wave originating from the same distance as that of the object, then the reconstruction is obtained by a Fourier transform resulting in what is called a lensless Fourier imaging system. Even though we show the various architectures for recording digital holograms of relatively large macroscopic objects, the same experimental setups can be used to perform digital holographic microscopy by placing suitable lenses like objectives for magnification at the appropriate place in the object beam.

3.5.1 Fresnel

A digital hologram can be represented by a sum of four interference terms. If O and R represent the reference wave field and the complex amplitude of the object wave at the hologram plane respectively, then the hologram, H can be represented by

$$H(x) = |O(x)|^2 + |R(x)|^2 + O(x)R(x)^* + R(x)O(x)^* \tag{3.12}$$

For simplicity, we use a one dimensional (1D) representation. The hologram, H contains the object information, O in the third term. When the reconstruction operation is performed on H, the other three terms contribute to the zero order noise and the twin image. The relationship between the wavefield at the hologram plane, O, and the object plane, o, is given by the Fresnel transform under the paraxial approximation.

$$O(x) = \exp\left(\frac{j\pi x^2}{\lambda d}\right) F\left\{o(x^{'})\left(\exp\frac{j\pi x^{'2}}{\lambda d}\right)\right\}(x) \tag{3.13}$$

In the case of a plane reference beam, the reconstruction is obtained by a numerical simulation of the Fresnel Transform as described in Section 3.2. The input to the numerical propagation algorithm is the digital hologram. It is shown in Equation 3.13 for a 1D case. The simpler of the two reconstruction methods discussed previously was the Direct method which involves the multiplication of the hologram, $O(x)$ by a numerical quadratic phase factor or chirp and then taking a Fourier transform of the product. In the Fresnel case, the twin image noise occurs as an out-of-focus noise in the reconstructed image. A Fresnel system can be in-line or off-axis depending on the tilt of the plane reference wave. Fig. 3.15 shows the reconstruction with an inline Fresnel system and Fig. 3.16 shows the reconstruction with an off-axis reference wave. As it can be seen, in the off-axis case, the twin image noise does not overlap with the object.

Figure 3.15: Reconstruction from an in-line Fresnel digital hologram after zero-order filtering.

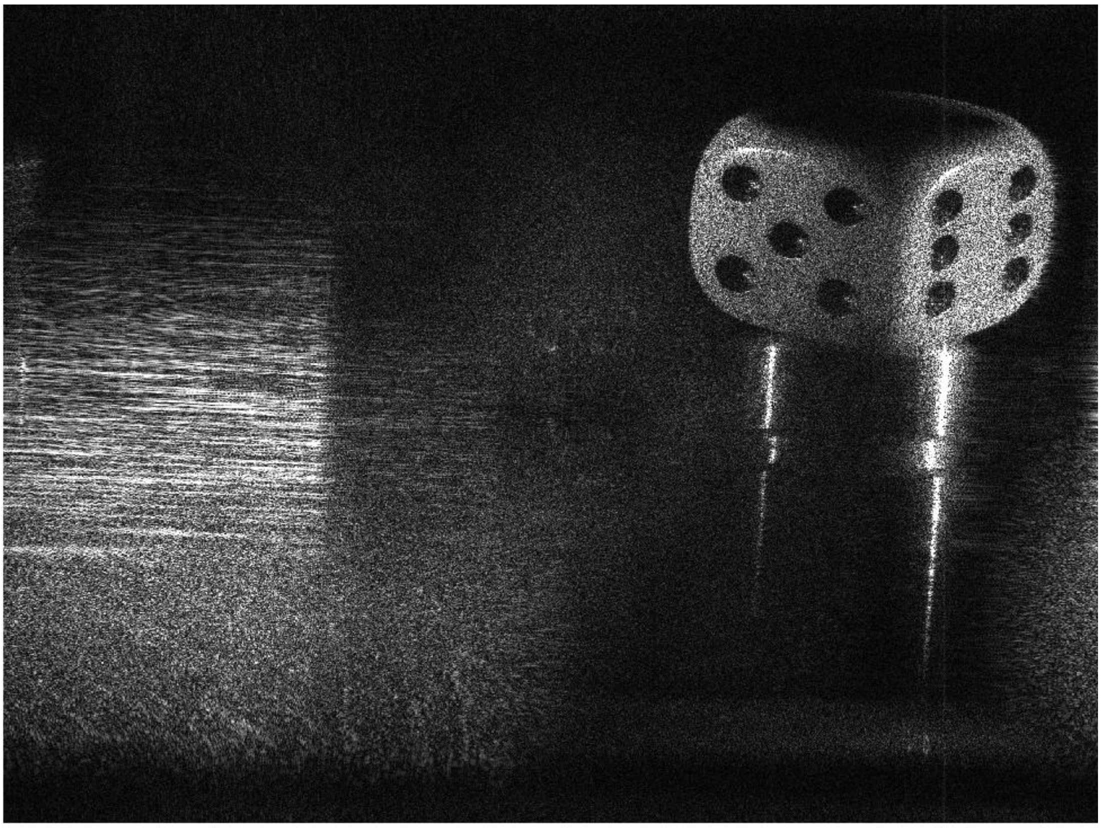

Figure 3.16: Reconstruction from an off-axis Fresnel digital hologram after zero-order filtering.

3.5.2 Lensless Fourier

Lensless Fourier digital holography involves the interference of the object wavefield with a spherical reference wave originating from a point source located at the same distance away from the sensor as the object. The basic idea is that we optically multiply the hologram with a quadratic phase factor so that it is not necessary to do it numerically. The Fresnel transform then becomes the Fourier transform aside from some constant phase factors. The reference wave from a point source displaced laterally by ξ and placed at a distance d away is represented by $R = exp\left[\frac{i\pi(x-\xi)^2}{\lambda d}\right]$. The reconstruction can be written as follows

$$\begin{aligned} F\left\{H(x)\right\}(x^{'}) = F\left\{|O(x)|^2\right\}(x^{'}) + \delta(x^{'}) \\ +o^{*}(\xi - x^{'})\exp\left[\frac{j\pi(\xi - x^{'})^2}{\lambda d}\right] \\ +o(x^{'} - \xi)\exp\left[\frac{-j\pi(x^{'} - \xi)^2}{\lambda d}\right] \end{aligned} \tag{3.14}$$

The Fourier transform of the reference beam is a Dirac delta function, $\delta(x^{'})$. So long as $o(x^{'})$ has a finite extent and ξ is sufficiently large we can expect the latter two terms to be spatially separated from the zero order terms and which occupy an area in the center of our reconstruction. In this way the complex object wavefield $o(x^{'})$ can be recovered. The reconstructed complex image, aside from a quadratic phase factor is thus given by the inverse Fourier transform of the hologram. This is achieved by calculating the DFT using the FFT algorithm. A comprehensive analysis of the extent of these four terms in Equation 3.14 can be found in [62].

A schematic for the experimental setup for lensless Fourier digital holography is shown in Fig. 3.17. The spherical reference beam is generated by placing a lens (focal length 10cm) in the path of a plane collimated reference beam such that the lens generates a point source at the same distance as the object is from the camera. Fig. 3.18 shows the reconstruction from an off-axis hologram. In Fourier digital holography, both the object and twin image appear in focus in the reconstruction plane but they are inverted. In Fig 3.2 the object DC term actually occupies the entire reconstruction plane and thus we have not ensured a correct spatial separation. However in this case we have lowered the power of the object term sufficiently that the object DC is weak relative to the other terms.

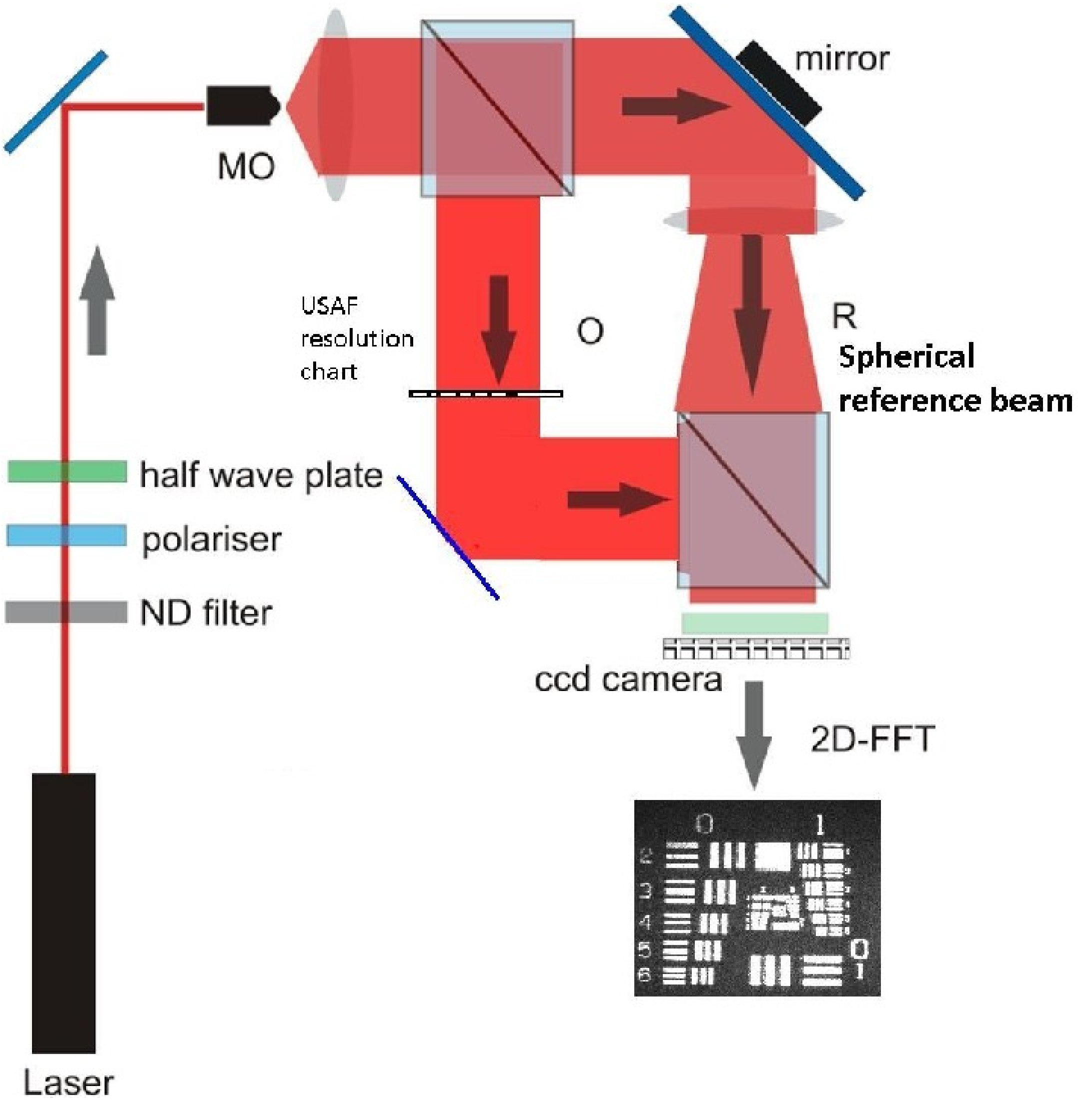

Figure 3.17: Schematic for lensless Fourier digital holography. This experimental set up was used to generate the some of the results for Chapter 5 in this thesis.

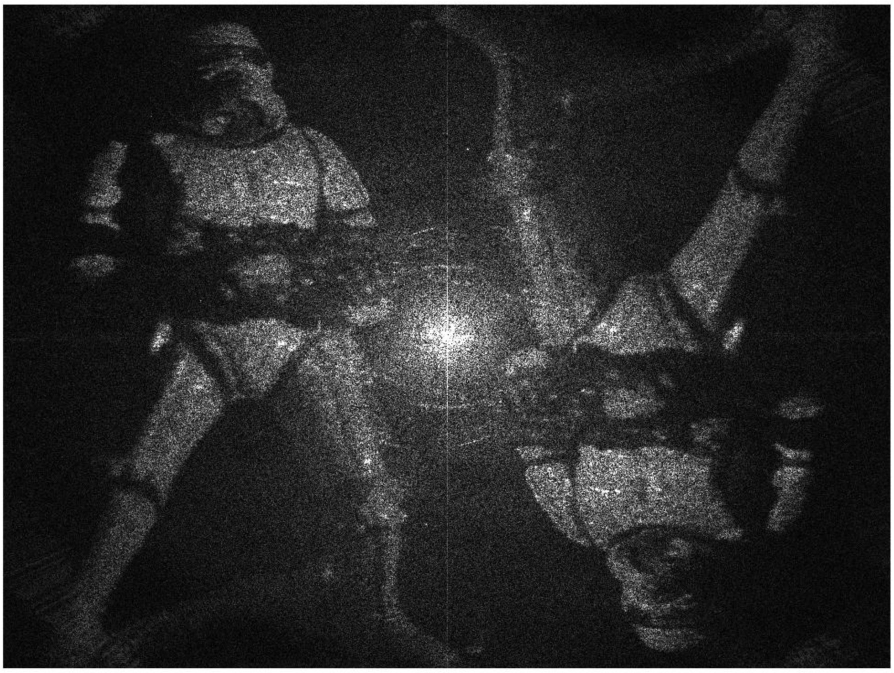

Figure 3.18: Reconstruction from an off-axis Fourier digital hologram

3.5.3 Phase shifting digital holography

The idea of using phase shifted holograms was first applied to digital holography by Yamaguchi [82] and can be explained as follows. Using a piezo-electric actuator which can precisely move to nanometer accuracy we can introduce systematic phase differences in the reference beam. In the commonly used four step phase shifting interferometry technique, four interferograms are captured with a $\pi/2$ phase shift between the interfering wavefields. The object wave field is computed from these four images.

Let I_1 be the hologram recorded from the camera.

$$I_1 = |o(x)|^2 + |r|^2 + 2ro(x)\cos(\phi_o(x)) \tag{3.15}$$

If three additional holograms, I_2, I_3 and I_4 are captured after inducing a phase shift, corresponding to $\pi/2$, π and $3\pi/2$ respectively in the object beam, then the new holograms can be written as

$$\begin{aligned} I_2 &= |o(x)|^2 + |r|^2 + 2r[o(x)\cos(\phi_o(x) + \pi/2)] \\ &= |o(x)|^2 + |r|^2 - 2r[o(x)\sin(\phi_o(x))] \end{aligned} \tag{3.16}$$

$$\begin{aligned} I_3 &= |o(x)|^2 + |r|^2 + 2ro(x)\cos(\phi_o(x) + \pi) \\ &= |o(x)|^2 + |r|^2 - 2ro(x)\cos(\phi_o(x)) \end{aligned} \tag{3.17}$$

$$\begin{aligned} I_4 &= |o(x)|^2 + |r|^2 + 2ro(x)\cos(\phi_o(x) + 3\pi/2) \\ &= |o(x)|^2 + |r|^2 + 2ro(x)\sin(\phi_o(x)) \end{aligned} \tag{3.18}$$

Now, we have 4 interferograms and the phase term, $\phi_o(x)$ can be calculated as

$$\phi_o(x) = \frac{I_4 - I_2}{I_1 - I_3} \tag{3.19}$$

and the amplitude term, $ro(x)$ can be calculated as

$$ro(x) = \sqrt{(I_4 - I_2)^2 + I_3 - I_1)^2} \tag{3.20}$$

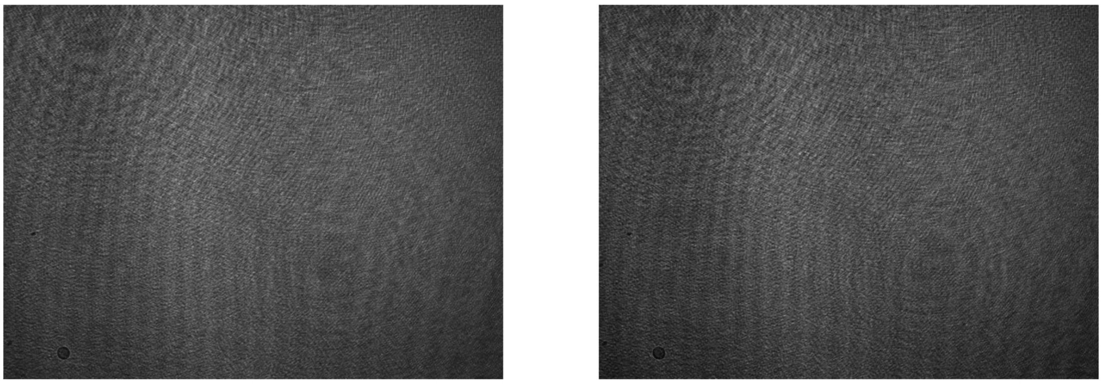

0° phase shift **90° phase shift**

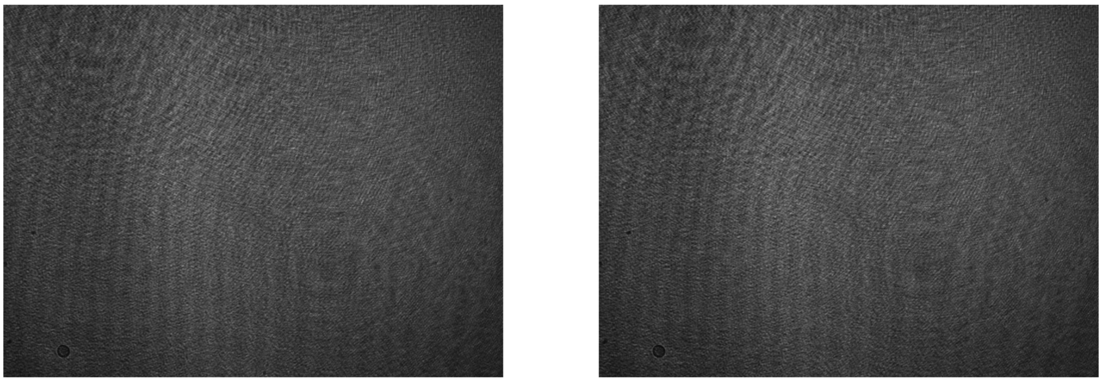

180° phase shift **270° phase shift**

Figure 3.19: The 4 holograms obtained using 4 step phase shifting.

Figure 3.20: Reconstruction from complex wavefield obtained using phase shifting. The exposure time was kept the same for all the holograms compared.

We have implemented phase shifting in our experimental setup and Fig. 3.19 shows the 4 interferograms obtained experimentally. Fig. 3.20 shows the reconstruction obtained from the phase shifting technique and Fig. 3.21 shows a comparison of the reconstructions from ordinary in-line with phase shifting. The improvement in image quality can clearly be seen.

3.6 Optical reconstruction of digital holograms

Digital holograms can not only be reconstructed numerically but also optically. This can be done by using light modulating devices like Spatial light modulators (SLMs). The FP7 funded REAL3D project is centered around developing technologies based on digital holography for 3D display purposes. Spatial light modulators can be either amplitude or phase modulating in nature. Phase modulating SLMs are more suitable for digital holography because most of the information is present in the phase of the hologram.

Fig. 3.24 illustrates the concept of optical replay of digital holograms. The hologram values are addressed to the pixels of the SLM and a coherent beam of light is made to illuminate the device. The wavefield embedded in the hologram is diffracted from the pixels of the SLM and an observing viewer can see the 3D object when viewing through the SLM. As a partner university in the REAL3D project, we have provided a number of high quality digital holograms of various objects to other project members. We have also experimented with optically replaying the holograms captured with our experimental setup. A replay setup shown in Fig. 3.22 was built at NUIM and a real-time 3D capture, transfer and replay setup was implemented. Digital holograms were recorded and were transferred using the local ethernet connection and replayed on the replay setup. The SLM used was a HoloEye LCOS reflective (model HEO1080P) with 1920 x 1080 pixels and a pitch of 8 μm. The laser used was a fiber coupled 532nm diode pumped solid state laser. Digital holograms of an object were captured using phase shifting and displayed on the SLM. Fig. 3.23 shows the numerical reconstructions before and after phase shifting. Fig. 3.24 shows the reconstruction obtained when replayed on the SLM.

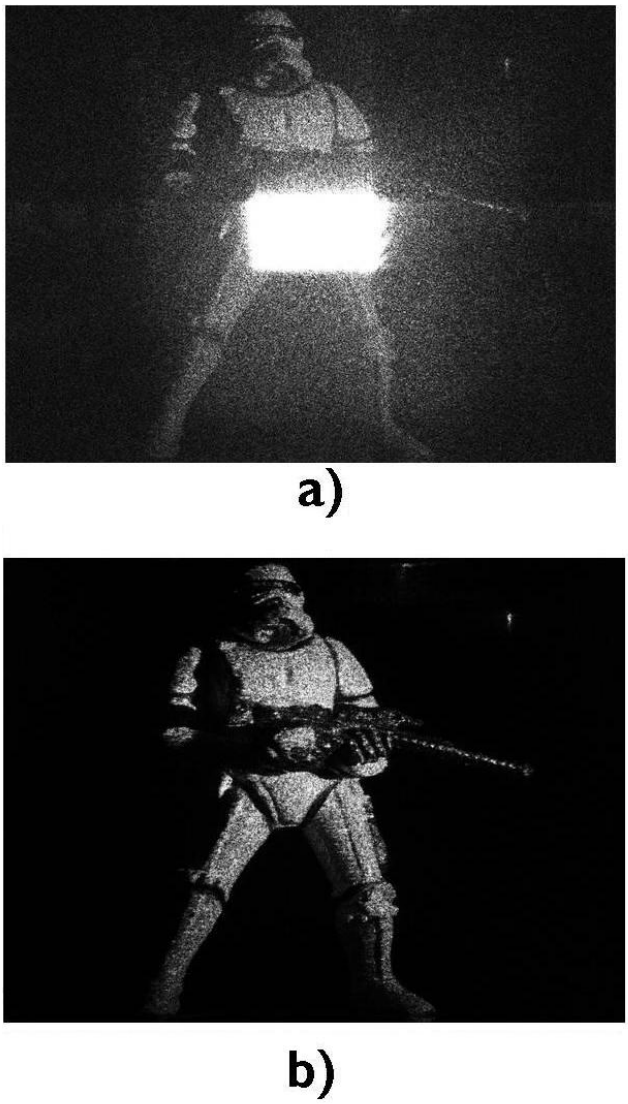

Figure 3.21: Comparison of PSI with inline-holograms. a) is the reconstruction from in-line hologram without filtering and b) is the reconstruction from the phase obtained by phase shifting.

Figure 3.22: Experimental setup for reconstructing digital holograms. Built by Gregorz Finke of Warsaw University of Technology in our lab at NUIM.

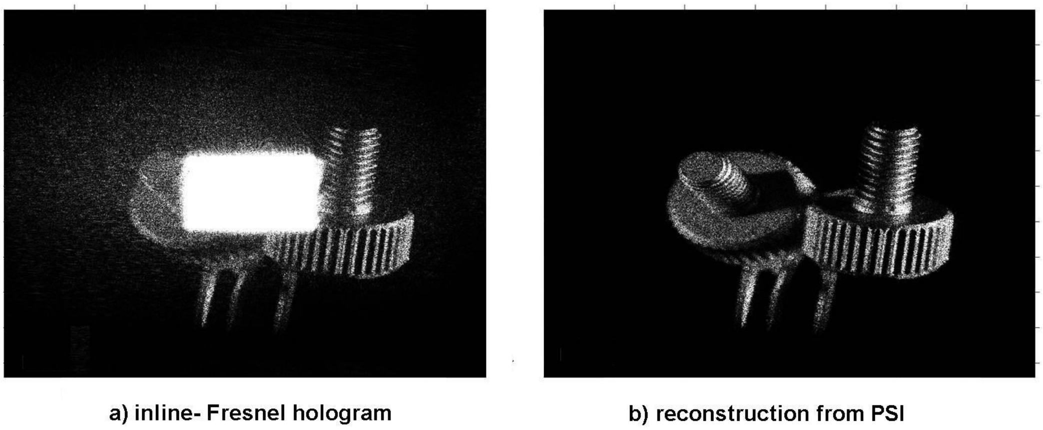

a) inline- Fresnel hologram

b) reconstruction from PSI

Figure 3.23: Numerical reconstructions of the 'screws' object. The screws are each approximately 2cm long. (a) Reconstruction from the original hologram. (b) Reconstruction obtained after phase shifting

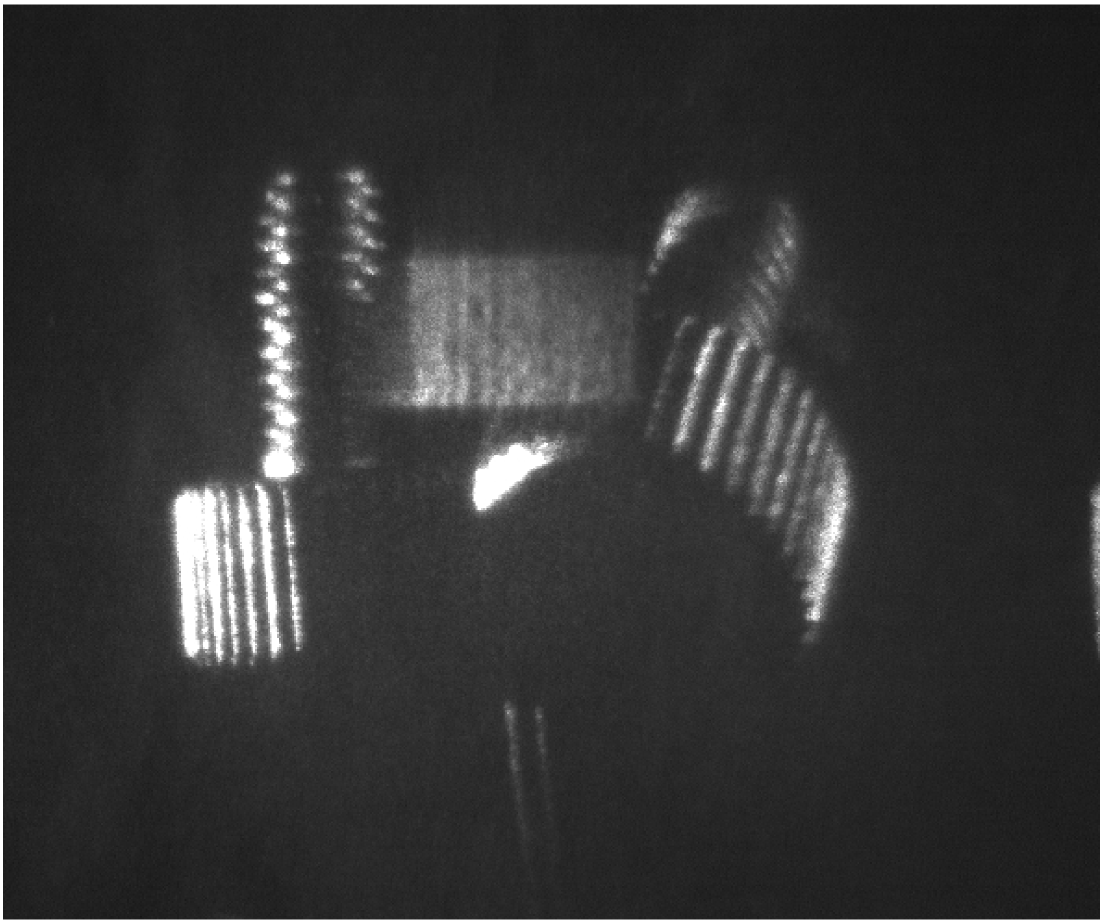

Figure 3.24: Optical reconstructions of the ‘screws’ object

3.7 Conclusion

In this chapter, we have discussed the most important features of the digital holographic imaging system. We discussed the issues which arise in digital holography such as the twin image noise and speckle noise. We derived the two important algorithms, the direct method and the spectral method which are used to reconstruct digital holograms. We also discussed the three different architectures which can be used to record digital holograms. We concluded by mentioning the optical reconstruction of digital holograms which forms the basis for the Real3D project. In the next chapter, we show some methods which we developed for the speed up of the reconstruction of digital holograms.

4

Speed up of reconstruction algorithms for digital holography

4.1 Introduction

In the previous chapters, the digital holographic imaging system and the reconstruction algorithms was discussed. In this chapter, we discuss some ways to speed up the computations involved in the reconstruction algorithms. For applications like real time digital holographic microscopy (DHM) and digital holographic interferometry of fast changing events, it is useful to decrease the reconstruction time of the digital holograms. Recently the use of graphics cards for general purpose computing is becoming popular [83, 84, 85]. These methods exploit the parallel many-core capability of the GPU (graphics Processing unit) to offer a significant speedup (5x-20x) over CPUs (central processing unit). GPGPU (General purpose computing on GPU) has been used to increase the speed of reconstruction of holograms on the GPU architecture. These hardware approaches require extra hardware and programming effort. Another way to decrease processing time is to reduce the numerical complexity of the algorithm by reducing the memory usage. As imaging sensor technology grows towards larger CCDs/CMOS and higher bit-depth cameras and digital holography finds more practical applications, such studies are very practical. In this chapter, we investigate two novel approaches to reduce the reconstruction time and the computational complexity of the reconstruction algorithms in digital holography. In Section 4.2 we introduce the idea of fixed point arithmetic for digital holographic microscopy and in Section 4.3 we discuss pre-computation and quantization of chirp matrices to decrease the reconstruction time. The work presented in this chapter led to the publication of a journal paper [1] and a conference paper [2].

4.2 Fixed point arithmetic based implementation

The numerical reconstruction process that is used both for digital holography in industry and in the research community employs floating point arithmetic. There are two major formats for representing real numbers in bit-sequences of 0s and 1s; floating point and fixed point. Computationally fixed point arithmetic is less demanding than floating point arithmetic. Fixed point devices have a simpler architecture with fewer gates and transistors and thus have smaller cycle clock time and are faster. Additionally fixed point processors consume less power and generate less heat than floating point processors and are thus well suited to portable devices where battery life is more important. Most embedded systems and handheld units have fixed point processors [86]. Already there are variants of DHM that do entail some degree of portability in the recording side such as submersible-digital inline microscopes for detection of life forms in remote inaccessible areas [87], holographic on-chip cytometry [88], plankton sampling [89] etc. In scenarios like these, it is essential to optimize the numerical reconstruction process so that it takes up as minimum resources as possible if reconstruction is to be carried out on site.

A floating point bit sequence in binary can be broken into two smaller bit sequences, the signed mantissa and the signed exponent. In the IEEE floating point notation[90] a number is represented by $N = (-1)^s \times m \times 2^{(e-127)}$ where s is the sign bit, m, the standard binary number represented by the (normalized) fractional mantissa and e the (biased) exponent. Employing a mantissa and an exponent allows the radix point to 'move' within the string of digits and thus floating-point notation allows calculations over a wide range of magnitudes, using the same number of digits as a fixed point notation. By convention, the mantissa varies between 0.5 and 1. The spacing between the numbers in a floating point representation is not uniform. Smaller numbers are closer to each other and larger numbers have larger separation.

Fixed point notation is simpler and is used in low end microprocessors where there is no floating point unit. The most common fixed point notation is the 'two's complement'.

In two's complement, positive numbers always start with a 0 and negative numbers start with a 1. If the first bit of a two's complement number is 0, the value is obtained by calculating the standard binary value of the number. If the leading bit of a two's complement number is 1, the value is obtained by assuming that the leftmost bit is negative, and then calculating the binary value of the number. The spacing between all the numbers is uniform and thus fixed point notation can be viewed simply as a scaled integer. The position of the radix point is fixed. A thorough description of fixed point and floating point arithmetic can be found in [91].

The setup for a typical DHM is shown in Fig. 4.1. An algorithm is presented for Fresnel propagation of complex phase data for phase contrast microscopy that is entirely based on fixed point arithmetic.

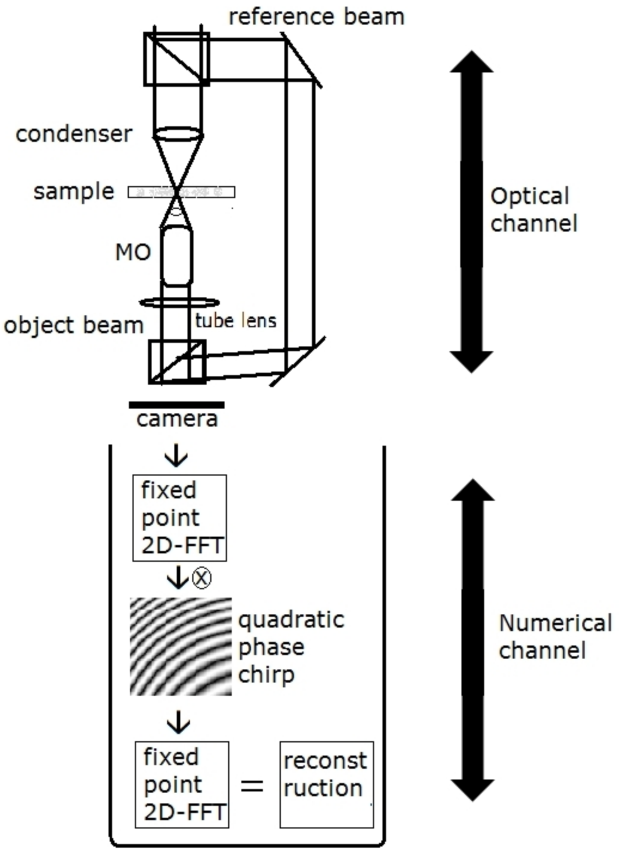

Figure 4.1: Setup for digital holographic microscopy. The optical and the numerical channel in digital holographic imaging are shown.

In addition the fixed point algorithm is tested on experimentally recorded digital holograms of a micro-lens array. The phase contrast microscopic images obtained allow us to investigate the quality of the phase reconstructions and to determine the minimum number of bits that give good reconstruction of the quantitative phase information. Previous studies on quantization have focused on reducing the number of bits only in the digital hologram for compression [92] [93]. By limiting the number of bits for every stage in the reconstruction algorithm, effectively all the variables in the reconstruction channel are quantized. In these experiments, a commercially available digital holographic microscope (DHM-T1000) from LynceeTec Inc is used. Using this microscope, the wrapped phase hologram of a microlens from a microlens array is recorded. An offaxis architecture is employed and the hologram is captured with a microscope objective of power 10x and NA 0.25. The camera in this microscope is a 1392 × 1040 pixels firewire camera and the laser is a monochromatic 682.5nm laser source. The object under investigation is a microlens array.

As discussed in Chapter 3, different algorithms exist that simulate the Fresnel transform. These different algorithms are derived from different expressions for the Fresnel transform. The study in this chapter is limited to the fixed point implementation of the convolutional method to reconstruct microscopic specimens using Matlab's fixed point toolbox. This is done because the convolution method is usually the reconstruction method of choice for DHM.

The key step in this implementation is the 2D-fixed point FFT algorithm. For this study an 'in-place' radix-2 fixed point as described in [72] is implemented. All the variables involved in all the stages of the reconstruction process (the phase hologram, the FFT twiddle factors and the chirp matrix elements) are essentially sines and cosines (fractions lying between -1 and 1). They can be represented by choosing n bits where one bit is assigned to the sign of the number and the remaining *n-1* bits are assigned to representing the fractional part. Sines and cosines are calculated by the Taylor series expansion in fixed point processors. This is computationally expensive as each element requires many multiplications and additions and can be speeded up using a precalculated table. For this reason almost all DSP systems employ a precalculated table of sines called the Look up table (LUT). The fixed point reconstruction algorithm is as follows:

- Convert discrete phase signal P into the chosen fixed point notation of n bits.
- Perform discrete 2D fixed point FFT of P. A = fixedptfft2(P);
- Calculate grid of the X-Y plane. $(m,n) = (m\Delta x, n\Delta y)$ for m = $-\frac{M}{2}$ to $\frac{M}{2} - 1$ and n = -$\frac{N}{2}$ to $\frac{N}{2} - 1$
- Calculate B = $\exp[\frac{i2\pi}{\lambda d}]\exp[-i\pi\lambda d(\frac{m}{Mdy})^2 + (\frac{n}{Ndx})^2]$ in fixed point precision using a look-up table where λ is the wavelength, d is the specimen distance, dy and dx are the pixel pitches of the sensor.
- Convert B into the chosen fixed point notation of n-bits.
- Calculate C = A.*B; where .* represents element by element multiplication.
- Perform discrete 2D fixed point FFT of C. D = fixedptfft2(C);

To compare the performance of the fixed point reconstructions with that of the floating point reconstructions, the reconstructed phase is unwrapped using the discrete cosine transform method [94]. The phase reconstruction becomes perceptible after 18 bits of representing data and shape of the microlens is completely perceptible at 20 bits Fig. 4.2 (a). The RMSE error in the surface height at 20 bits is 140nm. At 24 bits it is 6.28nm Fig. 4.2 (b) and at 32 bits it is 0.028nm. The floating point reconstruction is shown in Fig. 4.2 (c) for comparison.

The time taken by a version implemented on hardware is dependent on the total number of computations involved in the algorithm which can be calculated approximately. The total number of operational cycles required for multiplying a *'p'* bit word with a *'q'* bit word is pq and the total number of operational cycles required for the addition of a *'p'* bit word to a *'q'* bit word is $max(p,q)$ [95]. A radix-2 FFT takes $2N\log N$ multiplications and $3N\log N$ additions [72]. If we have a hologram of size N pixels and all the variables required for the numerical reconstruction at *'b'* bits, then the total computational cycles required for reconstruction will be $b^2(4N\log N + N) + b(6N\log N)$. The number of computational cycles and the resulting error in the surface height for a 512x512 hologram is shown in Fig. 4.3. The latter is calculated by comparing the unwrapped phase from reconstructions from the fixed point algorithm against 'ideal' reconstruction from the floating point algorithm. The '*' line shows the increase in

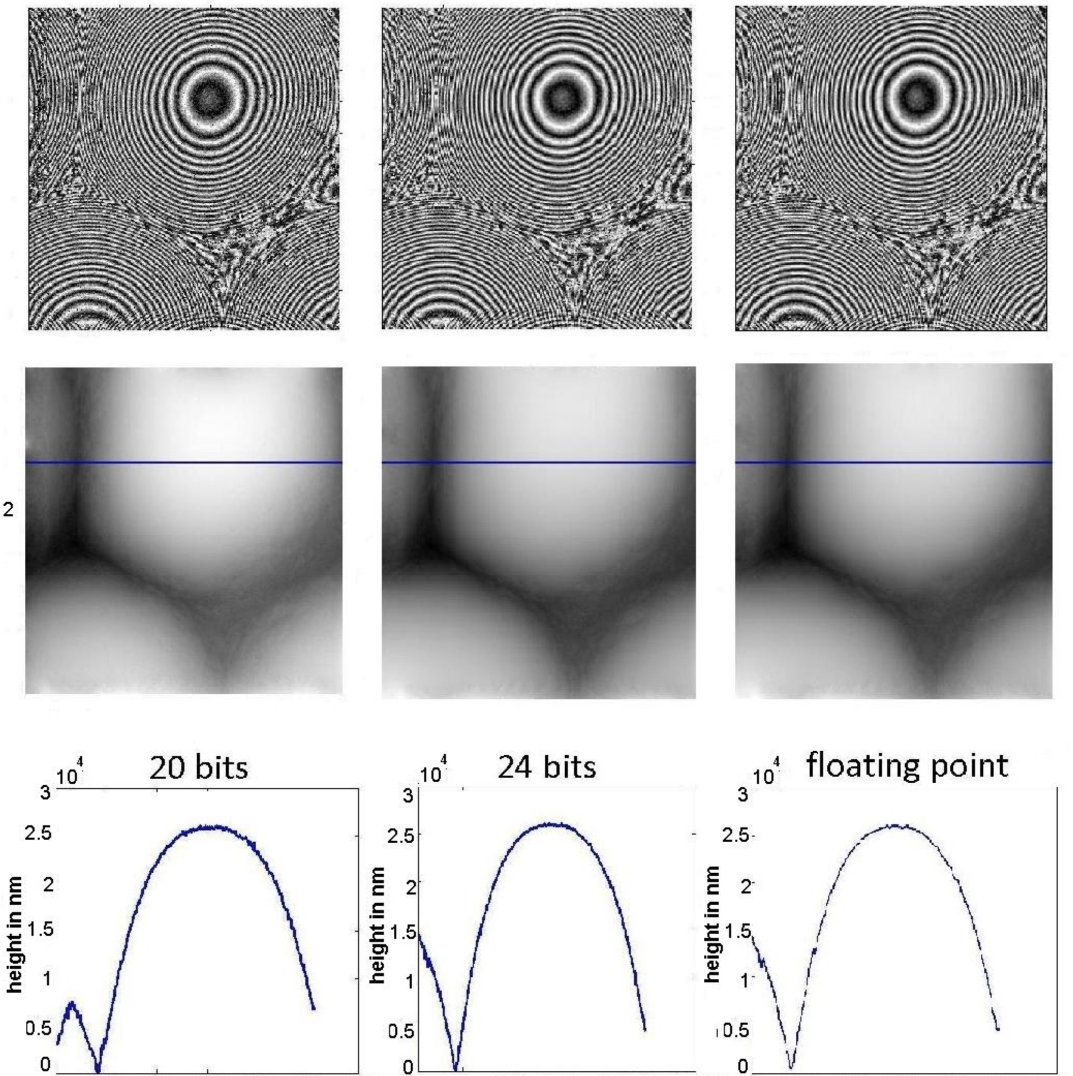

(a) (b) (c)

Figure 4.2: **Fixed point reconstructions Reconstructions for (a)20 bits fixed point (b) 24 bits fixed point and (c)64 bit(double precision) floating point. The surface profiles(third row) are shown for the horizontal black line in the second row.**

the number of computations in the reconstruction algorithm as the variable bit length. The ‘x’ line shows the corresponding decrease in the RMSE error of the unwrapped phase. It is seen that as the bit size increases, the number of computations grows almost linearly ($N\log N$ complexity) but the error in the reconstructed phase decreases exponentially ($\frac{1}{2^N}$). At 24 bits the total number of operations is approximately 45% less than those at 32 bits.

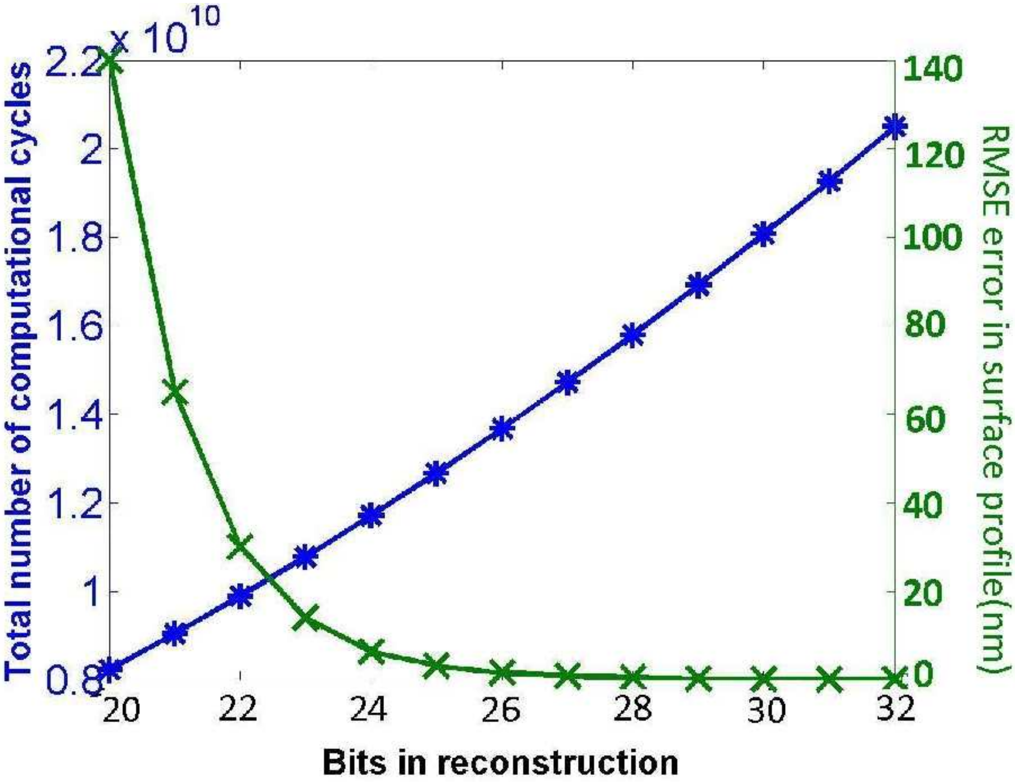

Figure 4.3: Number of computations required in reconstruction and the RMS error in the surface profile. Experimental results show that each additional bit reduces the error by half.

We have reconstructed phase contrast digital holograms using fixed point arithmetic for the entire reconstruction process. We have shown that it is possible to reconstruct quantitative phase data with good fidelity using fixed point arithmetic with 20 bits or more for reconstructing using the convolutional method. The number of computations decreases with the number of bits but the error in the signal increases. The number of bits can be chosen to suit the accuracy required by the application. We believe that this work will facilitate the use of low power fixed point processors for a fully portable record display digital holographic microscope. Such a device would have widespread application in on site industrial inspection and bedside cellular imaging.

4.3 Precomputation and compression of chirp

In the previous section, we aimed to reduce the number of operations required to multiply and add the variables by representing them in a fixed point format. In this section, it is aimed to (i) reduce the numerical complexity of the reconstruction of the digital hologram on general computer architecture by precomputation and quantization of the quadratic phase factor also termed as a 'chirp' used in the Fresnel transform. (ii) to study the impact of quantization in the numerical computation/reconstruction of digital holograms and how the memory usage in the reconstruction of a DH can be minimized. It is shown that precomputations of the chirp can speed up the computation on CPUs and GPUs. The chirp matrix is subjected to quantization to compress it and reduce the memory size. The effect this has on the reconstructed image quality is studied and finally these precomputed and compressed matrices are shown to be effective in a variance based focus search algorithm in which many reconstructions are required at various distances.

The idea behind pre-computation can be seen in the the practical implementation of the direct Fresnel transform which is as follows. Since we are interested in the intensity of the reconstructed image, we ignore the constant phase factor in the reconstructions.

- Calculate the grid of the X-Y plane where each element represents the x, y coordinates of the pixel. $(m, n) = (m\Delta x, n\Delta y)$ for $m = -M/2 : M/2 - 1$ and $n = -N/2 : N/2 - 1$
- Calculate the chirp $C = \exp -i\frac{\pi}{\lambda d}(m^2 + n^2)$ at all the points on the grid.
- Perform element to element multiplication of C and O to give $P = C.O$
- Perform a 2D DFT on P. $F = 2DFFT(P)$.
- The reconstructed image intensity is given by $|F|^2$.

We focus our attention to the intensity of the reconstructed image and thus the second phase factor is not calculated. The camera pixel pitch is Δx and Δy in x and y directions. O is quantized according to the quantization level of the camera and C is calculated in the computer with user defined precision. In order to speed up the Fresnel reconstruction, we note that the input chirp is independent of the input hologram field. The second chirp and the constant factors are also independent of the input. These matrices are composed of the exponential phase factors which are time-consuming to compute. If we precalculate a range of these matrices for different distances and load the corresponding data from memory during reconstruction, we can save 2 $N \times M$ computations of sines and cosines and thus reduce the time for reconstruction. This is advantageous for real time high resolution digital holographic systems running on nominal hardware. The computation reduces to 2 vector multiplications and the FFT algorithm. Table 4.1 shows the speedup on different hologram sizes achieved by precomputation.

Hologram size	No loading(seconds)	With loading (seconds)	Speedup
100x100	0.0613	0.04731	1.3
200x200	0.1027	0.07023	1.46
500x500	0.439	0.26449	1.66
1000x1000	1.736	0.99297	1.74
2000x2000	7.1904	4.22684	1.7

Table 4.1: Speedup on CPU

We perform the reconstructions using preloading on a NVIDIA Geforce graphics card (with 768 Mb of onboard memory) on a AMD Athlon 64 X2, 2.31Ghz, 2 GB RAM . We use the Jacket engine from Accelereyes for Matlab to run our code on the GPU. The results are shown in Table 4.2. A large number of these chirp matrices which cover a large distance can be stored permanently in memory and can be accessed by the program whenever the reconstruction is demanded for a particular distance.

To speed up the computation further, we quantize the chirp phase factor and study the effect on the reconstruction. We do so by restricting the total number of angles used to calculate the sines and cosines in the chirp. Thus the chirp matrix can be represented using fewer bits. This reduces the total filesize of the data file and thus

Hologram size	No loading(seconds)	With loading (seconds)	Speedup
100x100	0.0629	0.0555	1.13
200x200	0.0646	0.0522	1.23
500x500	0.0854	0.0672	1.27
1000x1000	0.1819	0.0775	2.34
2000x2000	0.5336	0.2514	2.12

Table 4.2: Speedup on GPU

allows the possibility to load up a large number of matrices in the program memory space. The quantized chirp can further be subjected to a lossless or lossy compression to reduce the file size further of the precomputed matrices. The compressed files will then have to decompressed during execution of the Fresnel integral. Consider the algorithm described in section 1 to compute the chirp phase factor for a hologram of an object placed at a distance of 285mm of size 1024 × 1024, with a wavelength of 785nm and with a pixel pitch of $6.45\mu m$ in both directions. Using the direct reconstruction, the computed chirp matrix has a total of 104265 unique angles at which the sines and cosines have to be calculated. If we bin the angles into a smaller number of levels, we will not only reduce the number of computations required to generate the full chirp matrix but also reduce the total number of bits per pixel required to 'represent' this matrix. (For example using 512 angles we can represent using 9 bits per pixel). A digital hologram of the object (a stormtrooper figurine), placed at a distance of 28cm is recorded with our setup and the numerical reconstruction is performed using different chirp matrices. Fig. 4.4 shows the quantized values of the angles and the resulting phase distribution and the reconstructed image.

Fig. 4.4 (a), (d), (g), (j), (m), (p) and (s) show the angles representing the chirp which are the unquantized, 512, 256, 64, 16, 8 and 4 angles respectively. Fig. 4.4 (b), (e), (h), (k), (n), (q) and (t) show the image of the real part of the chirp matrix showing the subsequent quantization and Fig. 4.4 (c), (f), (i), (l), (o), (r) and (u) show the intensity of the reconstructed image. As it can be seen limiting the number of angles to just 4 gives perceptually satisfactory images. To quantify the difference, we calculate the NRMS error between the reconstructed intensities and the original intensity by using the following equation where I_{fc} is the reconstructed intensity when

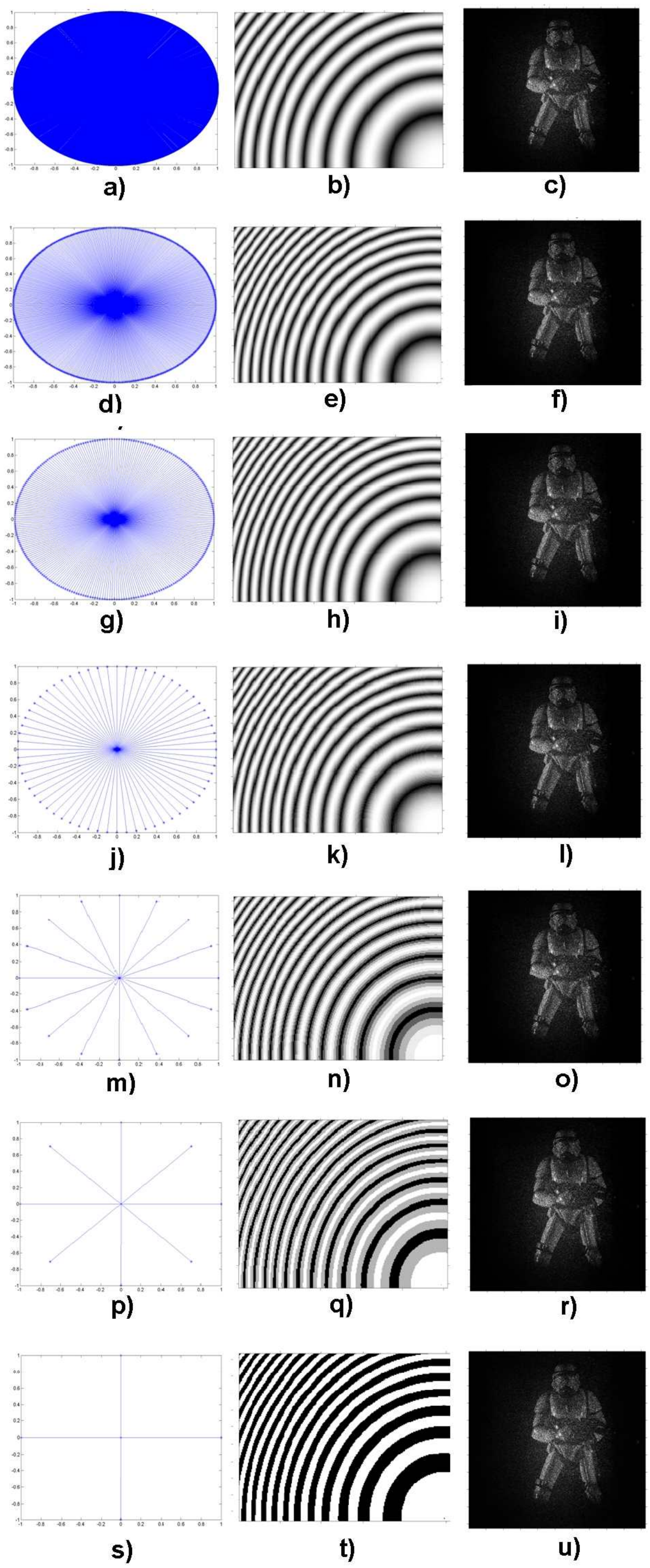

Figure 4.4: Reconstructions using quantized chirps.

we use a complete chirp calculated at all the required angles and I_{qc} is the reconstructed intensity resulting from the use of the quantized chirp in the reconstruction algorithm.

$$NRMSE = \frac{\sqrt{\sum\sum |I_{qc} - I_{fc}|^2}}{\sqrt{\sum\sum |I_{fc}|^2}} \tag{4.1}$$

Fig. 4.5 shows the NRMS error obtained from the reconstructions. The error is highest for 4 angles in the chirp (0.241) and decreases with increasing the number of angles. It can be debated whether the NRMS error metric is a reliable metric when comparing images from a visual perceptive point of view.

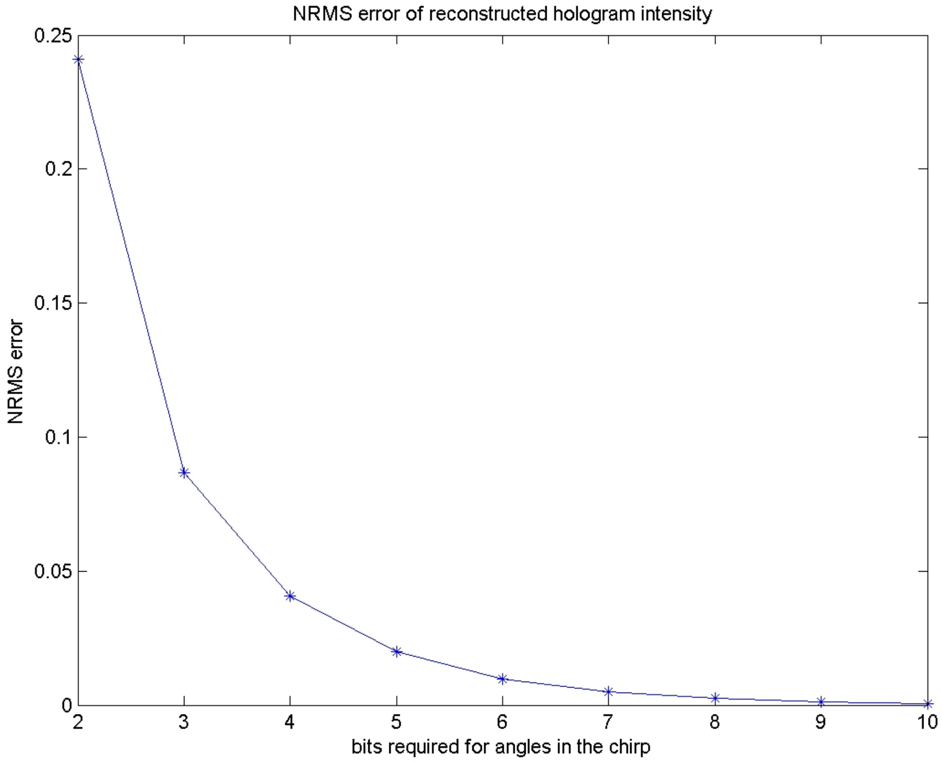

Figure 4.5: NRMS error for the reconstructed images.

It has been shown that the MSE is not a good metric for such studies and variance of the image is a better metric [96]. In Fig. 4.6 we show the percentage variance of the reconstructed image versus the number of bits required for the angle in the chirp. The variance changes to less than 30% for the 4 level representation.

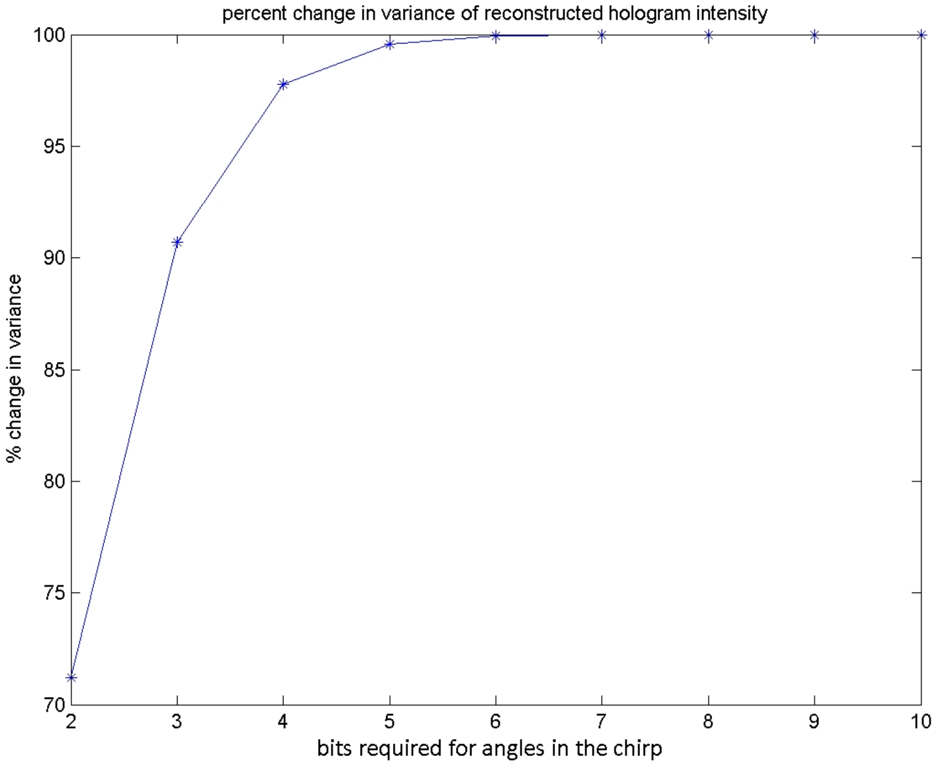

Figure 4.6: Change in variance with respect to the original.

Because of the decreased variance of the data, the quantized chirp matrices can be compressed effectively using lossless compression techniques. We use Matlab's built-in compression scheme used in saving MAT format files to compress and store the chirp matrices. Matlab's compression scheme is based on gzip and uses the DEFLATE algorithm [97]. Fig. 4.7 and Fig. 4.8 show the reduction in filesize of the compressed files. The compressed file size of the un-quantized chirp matrix is 10MB. The file size of the quantized chirp and the average time taken to load and decompress the file decreases along with the quantization level.

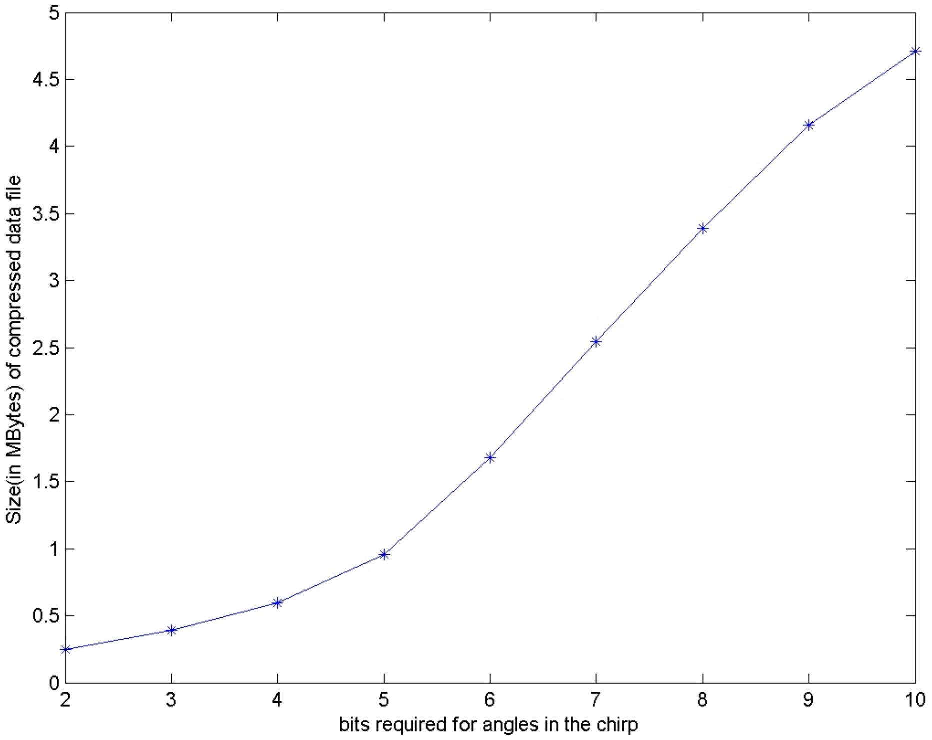

Figure 4.7: Size of compressed chirp.

We have shown that even with 4 level representation (2 bit) of the matrix, the reconstructed object can be perceptible. We now investigate the application to a variance based focus search algorithm to identify the correct focusing distance. The focusing distance can be found by using variance as a measure of the sharpness of the image. A section of the reconstruction plane was taken and the variance of that section measured

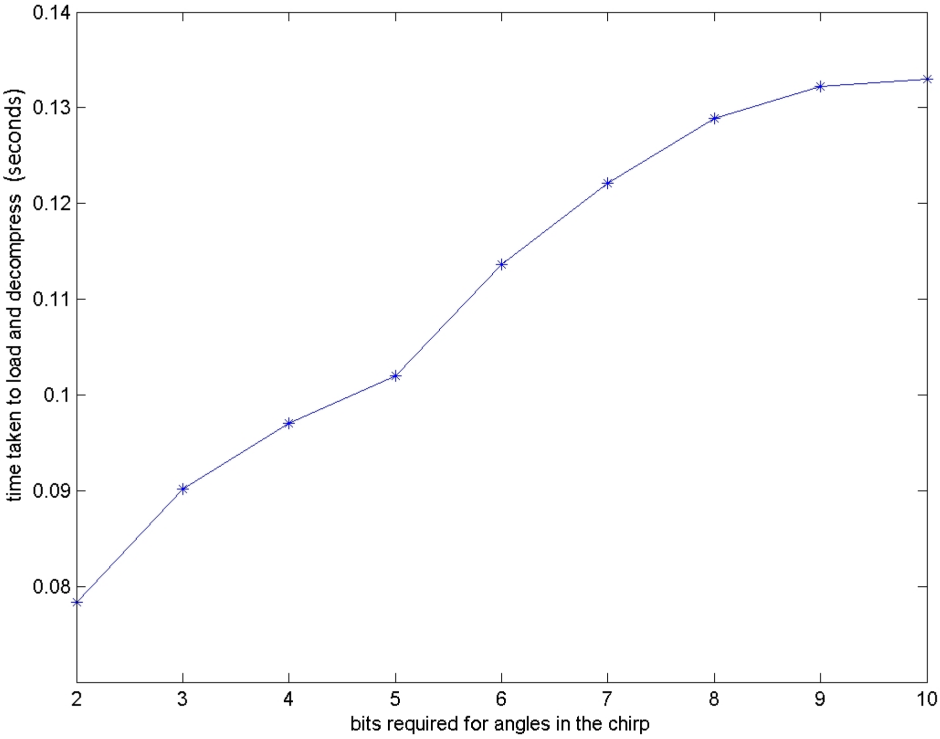

Figure 4.8: Time taken to load and decompress the pre-computed chirp matrix.

at different reconstruction distances. The variance was calculated for the chosen section of the reconstruction plane. The focusing distance is 285mm as checked manually. The variance of a reconstructed object in general varies smoothly as a function of reconstruction distance. The jitter introduced due to the quantized chirp can be removed by a moving average filter. Fig. 4.9 shows the variance vs. distance plot at different levels of quantization. The correct distance has been unambiguously recovered even when using a 2 bit representation of the chirp.

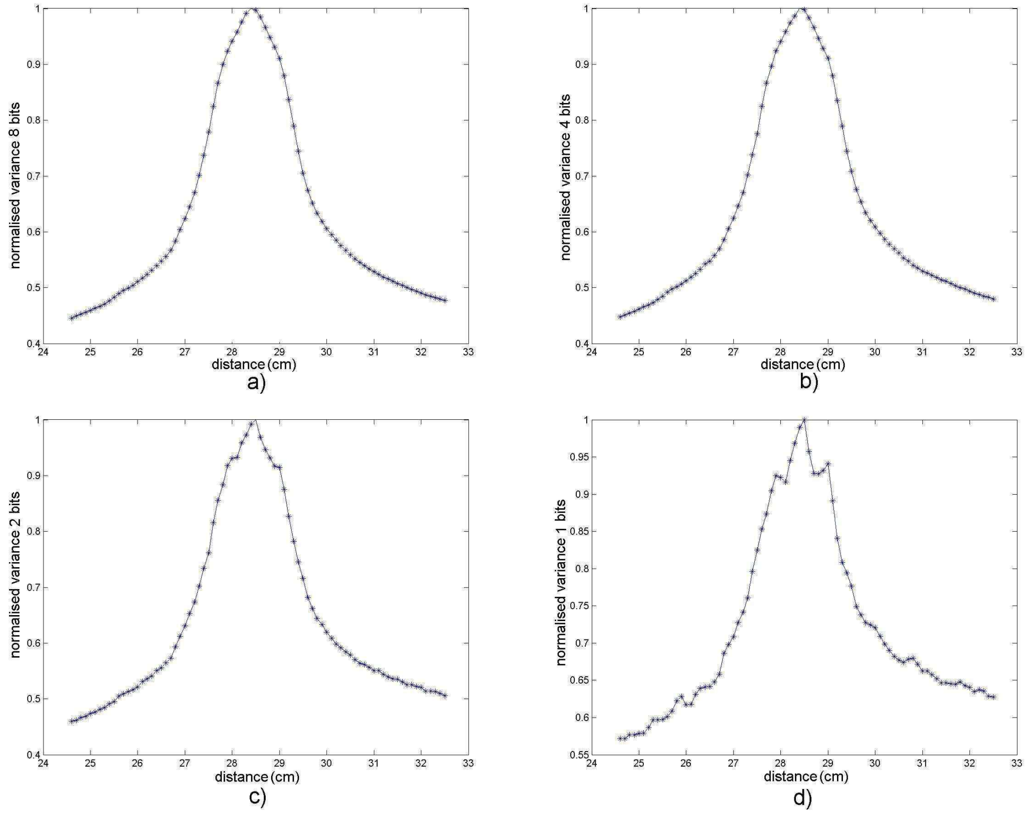

Figure 4.9: Variance of a section of the hologram as a function of distance of reconstruction. The variance is highest when the object is in focus.

We have shown the benefits of using a table of precomputed chirp phase factor matrix on the speed of digital hologram reconstruction on normal CPUs and GPUs. The speedup improves with larger matrices and occurs due to the fact that loading large data from memory takes very little time compared to calculation 'on the fly'. We have reduced the quantization of the precomputed phase factors in order for it to be compressed effectively and have shown the NRMS error and variance of the reconstructed image intensity. Additionally we have also shown how this highly quantized chirp can be used in focus search algorithm where a large number of reconstructions at different distances over the search range are required. We have limited our investigation to the direct method of computing the Fresnel transforms which is made up of two chirp multiplications and a FFT algorithm [8]. Other methods of reconstruction also require calculation of chirp data which is independent of the input hologram. The convolution method discussed in the previous section and introduced in Chapter 3 requires an FFT algorithm followed by multiplication by a chirp followed by a second FFT. Since this chirp is independent of the input hologram field, its precalculation will also result in considerable time savings. We can expect the same performance as for the direct method for NRMS error and variance as well as speed up and memory storage. These reduced complexity matrices can give perceptually satisfactory reconstruction of 3D objects embedded in holograms and autofocus algorithm based on variance gives the correct focusing distance.

4.4 Conclusion

In this chapter, we outlined our first investigations into quantization in the reconstruction algorithms. In section 4.1, we looked at using fixed point arithmetic for the entire reconstruction process and this included the use of fixed point FFTs. We focused our study on the convolution method of reconstruction with the application in mind of using portable low power electronic devices for reconstruction of digital holograms of microscopic specimen. This study was published in the journal paper [1]. In Section 4.2, we looked at quantizing the angles used in the chirp for the direct method of reconstruction. We showed that the reconstructed intensity was clearly distinguishable even with low quantization and we showed that precomputaion of these chirps allowed for speed up of the reconstruction process with only a small overhead in terms of memory storage. The investigation outlined in Section 4.2 was published in [2].

These two studies formed the basis of future research into understanding the effect of quantization of the camera pixels on the final reconstruction in terms of both the phase and the amplitude. This study is outlined below in Chapter 5. where we study the influence of quantization of the hologram on the reconstructed image and phase quality. We also study the influence of shot noise.

5

Additive noise in digital holography: Statistical analysis

5.1 Introduction

In the previous chapter, we showed that reconstruction algorithms can be speeded up by pre-computation and quantization of the variables involved in the computation. We also implemented the reconstruction algorithm using fixed point arithmetic. These studies motivated us to look deeper into the issue of quantization and its impact on the reconstructed intensity. In this chapter, we do the following.

- In Section 5.2, we review the work done in quantization in digital holography and the results and observations presented on this topic in the literature.
- In section 5.3, we analyze quantization noise in lensless Fourier digital holographic imaging. In this architecture, the reconstruction is obtained by a single discrete Fourier transform(DFT) of the recorded hologram. We believe the results can be extended to the Fresnel case. To the best of our knowledge, this is the first time that quantization has been studied for the lensless digital holography architecture.
- We study the influence of quantization noise in the hologram plane and the reconstruction plane in Section 5.3.1 and Section 5.3.2.
- We derive a simple theoretical model that predicts the effect of quantizing the digital hologram on both the phase (Section 5.3.3) and intensity values (Section 5.3.4) of the reconstructed image.

- We extend the results obtained to shot noise in Fresnel digital holographic microscopy in Section 5.4. We again develop a model for predicting the influence in the reconstructed phase due to shot noise in the recording plane.

5.2 Quantization noise

In digital holography, an interference pattern is recorded on a digital camera. Therefore quantization of the recorded hologram is an integral part of the imaging process. Recently the resolution of CCD/CMOS sensors has increased significantly and with it, so too has the computational requirement of a digital holographic imaging system. The bandwidth needed for transmission of holograms from one point to another has also increased and hence compression of digital holograms has been an active area of research [9-18]. In this context, the quantization of the hologram and the result on the reconstructed images has been studied before.

Reducing the number of quantization levels to represent the hologram has various advantages. It directly reduces the memory requirement of the hologram and combined with suitable processing and hardware can decrease the computational requirement of the digital imaging system [1]. A quantized hologram can also be compressed effectively. However, as a side effect, the quantization introduces a quantization noise in the hologram and the reconstructed image. This can have an adverse effect on the quality of the reconstructed intensity for 3D display applications and on the fidelity of the phase information in the case of digital holographic microscopy. The advantages and disadvantages of quantization in digitally recorded holograms in various recording architectures have been discussed by a number of authors. Naughton et. al. [92] have demonstrated the effectiveness of quantization in combination with lossy and lossless compression techniques for transmission and storage of digital holograms. A networked 'real time Fresnel field transmission system' was developed by the authors in [98] to test different compression algorithms. They obtained the complex wavefield by phase shifting and then quantized and compressed the real and imaginary parts separately. In [99], quantization of the real and imaginary parts of the complex hologram values (obtained from phase shifting) was studied in combination with lossless and lossy compression techniques. In [100], reconstruction from pure phase objects was studied and perceptible reconstructions were achieved by using a 1 bit (binary) representation level. Various other quantization schemes were developed and studied by Shortt et. al. [101, 102, 103]. An in-depth simulation and experimental study on the effect of quantization in phase shifting digital holography was performed by Mills and Yamaguchi [93] in which the individual phase shifted interferograms were quantized before calculating the complex wavefield. They found that the use of 4 bits for hologram quantization is adequate for 'visual recognition' of the reconstructed images. They also mention that using 2 bits per pixel (4 levels) gives noisy reconstructions. In phase shifting digital holography, Darakis et. al. studied the effect of compression in the individual interferograms, the complex hologram and in the reconstruction [104, 105]. Also see [106] for a survey on quantization in holography.

The lowest quantization one can achieve directly is 1 bit per pixel, the binary hologram. This introduces appreciable noise in the reconstructed image. If the noise in the reconstructed image can be reduced, there are several advantages of using binary holograms for display and projection applications. Ferroelectric binary SLMs have very fast switching rate (upto 10000 fps) and can display holograms at a fast frame rate. Binary holograms occupy considerably less memory (90% less than a 8 or 12 bit per pixel hologram). Also, in principle it is faster to acquire binary holograms. Such advantages of optical setups employing binary SLMs have been shown in [107] and [108]. Another imaging strategy employing binary sensors and compressive sensing was recently shown in [109].

In the 1960-70s, various authors studied the influence of quantization arising from the finite printer resolution in computer generated holograms and their efficiency [110, 111, 112]. In [113], Powers and Goodman derive the probability of error in holographic memory employing computer generated holograms when there is a quantization error in the hologram plane. Binary holograms were especially studied [114] because of the ease of printing and new methods were also developed for synthesis of binary CGHs [115].

Using this experimental setup, we record a lensless Fourier hologram of a 2D object, a USAF resolution chart. Since we are studying quantization, we intentionally use the full dynamic range offered by the camera by adjusting the power in the beams. This results in some saturated pixels. The percentage of saturated pixels is 0.5% and thus has little effect on the reconstructed image. This hologram is quantized at 12 bit

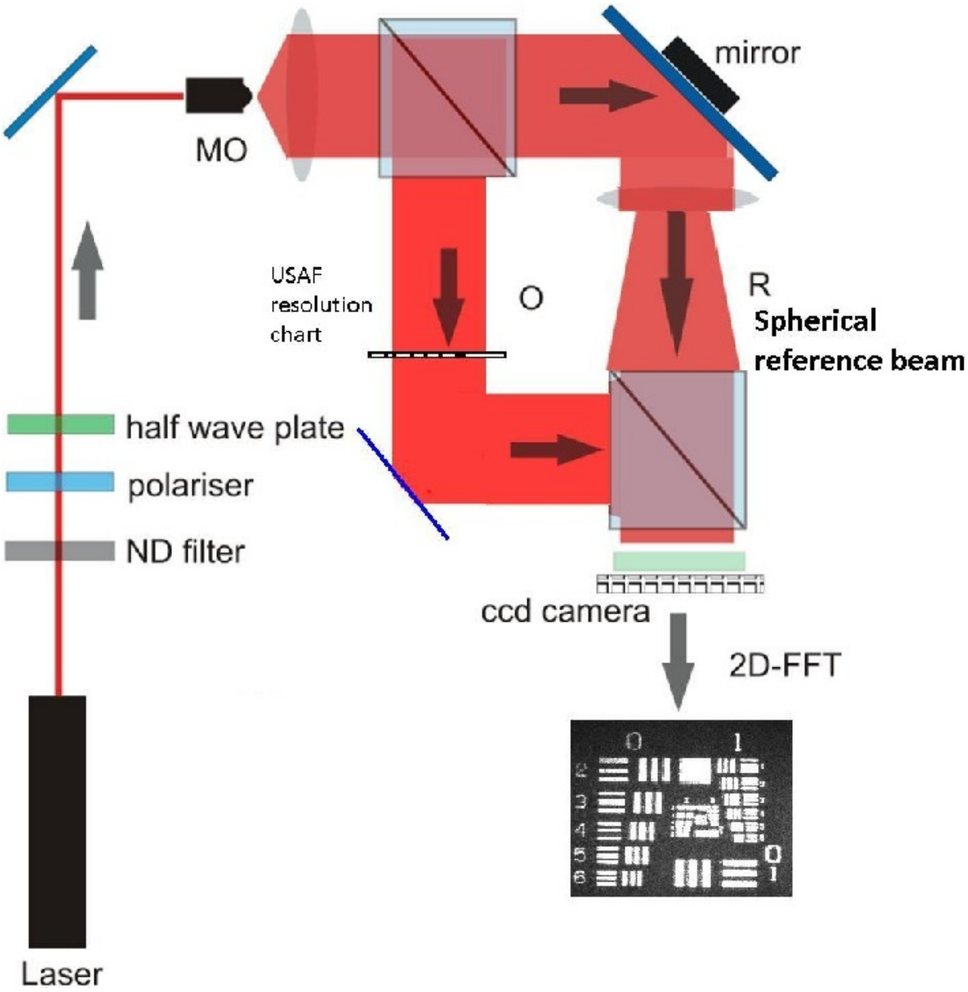

Figure 5.1: Setup for Fourier Digital holography.

precision by the camera and is our benchmark hologram for comparing the effect of further quantization.

5.3 A model for quantization noise in Fourier digital holography

5.3.1 Noise due to quantization in the hologram plane

The image acquired by any digital image sensor is in a quantized format. This can be further quantized computationally to suit the needs of the application, e.g compression. We base our experimental results on digital holograms that are obtained by digitally re-quantizing our benchmark 12 bit hologram to a reduced number of quantization levels. We use the following notation throughout this chapter which is illustrated in Fig. 5.3.

- H represents the ideal 2D hologram and h represents its ideal reconstruction. H_l represents the re-quantized 2D hologram. h_l represents its reconstruction. l denotes the number of bits used to quantize the hologram.
- Q_l represents the noise in the hologram plane due to quantization with l bits. It is a 2D matrix representing the quantization error per pixel. q_l represents the resulting quantization noise in the reconstruction plane. q_l is the DFT of Q_l.

When an optical wavefield with a particular variation in irradiance (of dark to bright) is incident onto the image sensor, the image sensor captures this variation in accordance with the quantization rate. During the digital capture process the camera pixels convert the charge acquired into a voltage and this voltage is digitized and quantized into a pixel value which is directly indicative of the intensity of light incident on that pixel. The interval between M_x and M_n is uniformly divided into 2^l levels and all the pixels are 'binned' into their closest level. The quantizing interval thus is

$$\Delta_l = \frac{M_x - M_n}{2^l} \tag{5.1}$$

and the quantized hologram thus has 2^l levels. Quantization results in some loss of information and causes noise in the reconstructed image in both the phase and amplitude. This is depicted in Fig.5.4 which shows the degrading effect of uniform quantization

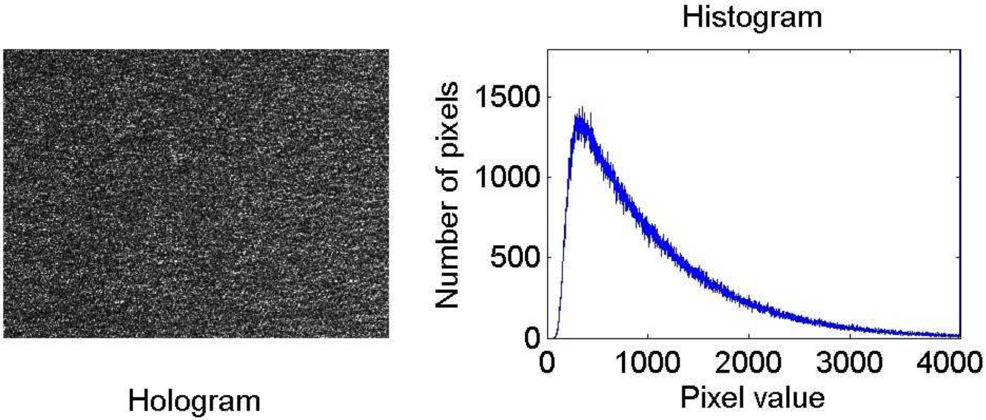

Hologram
(a)

(b)

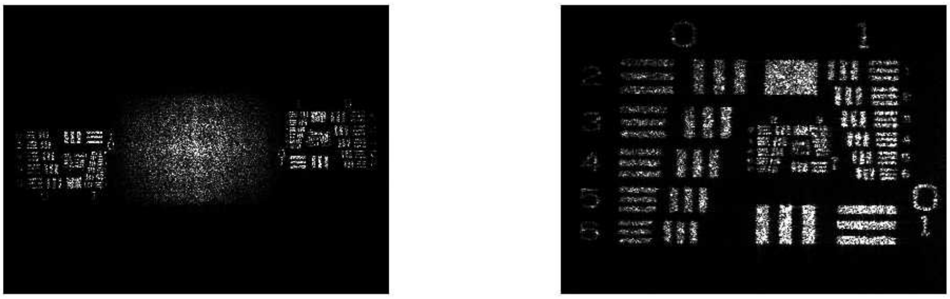

Reconstruction
(c)

Object area
(d)

Figure 5.2: Captured test hologram and reconstruction. (a) The original hologram. (b) The histogram showing the grayscale value and the corresponding number of pixels. (c) and (d) the reconstructed image.

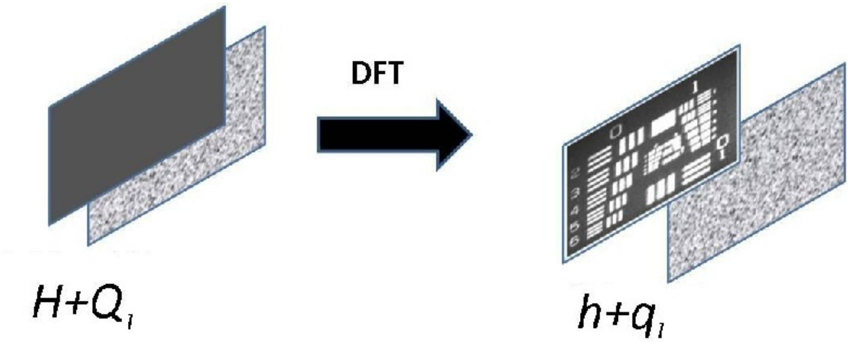

Figure 5.3: Illustration of the notation used between the hologram plane and the reconstruction(Fourier) plane. Q_l stands for the quantization noise in the hologram plane and q_l stands for the quantization noise in the Fourier domain. q_l is complex and the reconstruction is the complex sum of the ideal reconstruction h and the noise q_l

on the reconstructed image quality. In Fig.5.4(a), we show the histogram of H_{12}, the hologram recorded using the full 12 bit range of the camera. In Fig.5.4(b) we show the intensity of the resulting numerical reconstruction. In Fig.5.4(c), we show the histogram of H_8, the case where the 12 bit hologram is re-quantized to 8 bits. In this case there are 16 times fewer levels than the 12 bit case. Thus we see that the number of pixels in each bin increases. In Fig.5.4(d), the intensity of the resulting numerical reconstruction is shown. There is no apparent reduction in quality compared with the 12 bit case. In Fig.5.4(e) and Fig.5.4(f), the holograms and the reconstructed image is shown for the 2 bit case where there are just 4 levels. Even though the visual quality has decreased the object is still perceptible. Finally Fig.5.4(g) and Fig.5.4(h) show the limiting case for quantization, the binary case where the object is immersed in a high amount of quantization noise.

Quantizing in the way described above means that the value of the quantized pixel will deviate from its correct value by $\pm\Delta_l/2$. Thus we can model the quantization noise, Q_l, by assuming that it is an additive white noise sequence with values uniformly distributed between $-\Delta_l/2$ and $+\Delta_l/2$ where Δ_l is the quantization interval[116]. In the hologram plane, the quantized hologram can be written as

$$H_l = H + Q_l \tag{5.2}$$

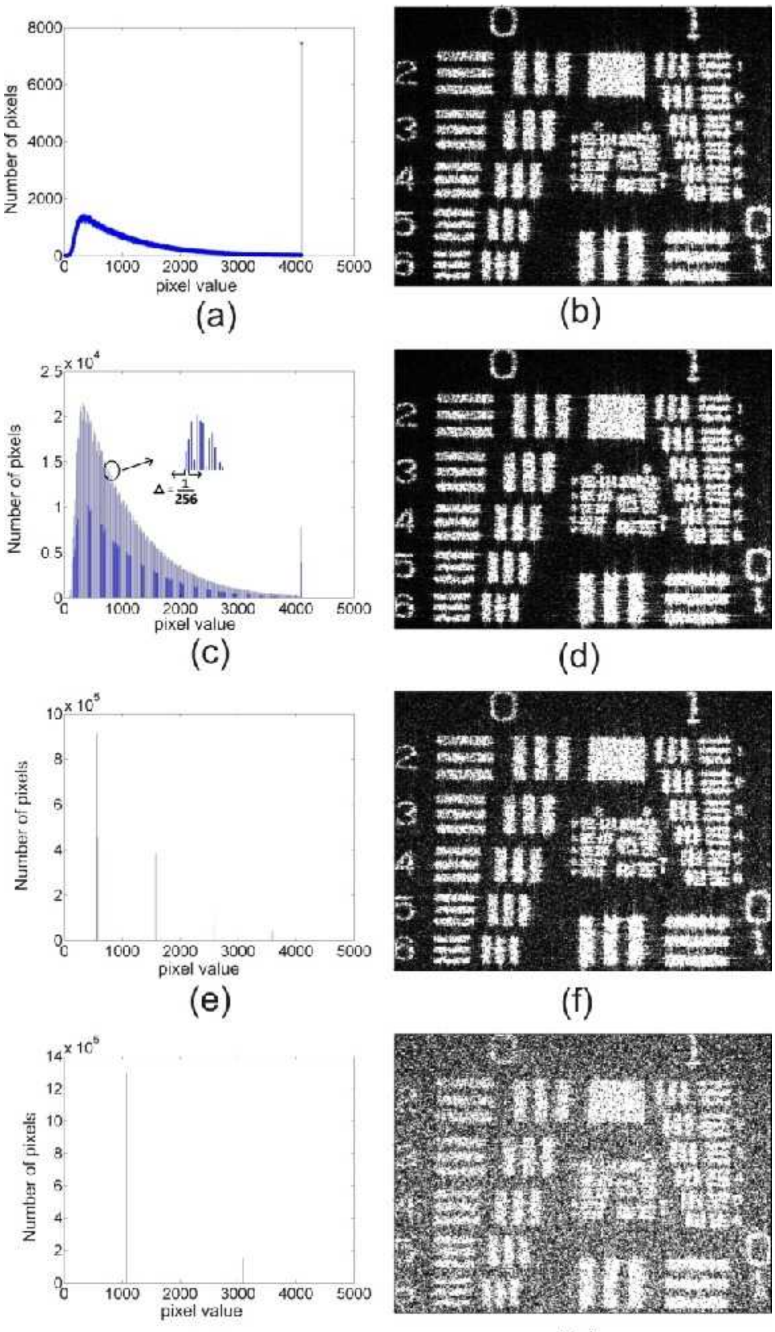

Figure 5.4: Histograms for various quantization levels and the corresponding reconstructed images. (a) and (b) 12 bits, (c) and (d) 8 bits, (e) and (f) 4 bits and (g) and (h) 1 bit(binary) cases.

For such a uniform white noise sequence, the mean value is 0 as the noise is fluctuating randomly between $-\Delta/2$ and $+\Delta/2$ and the variance can be derived as

$$\sigma_{Q_l}^2 = \int_{-\Delta_l/2}^{\Delta_l/2} x^2 \left(\frac{1}{\Delta_l}\right) dx = \frac{\Delta_l^2}{12} \tag{5.3}$$

Thus for a quantizer with interval Δ, the standard deviation in the error is

$$\sigma_{Q_l} = \frac{\Delta_l}{\sqrt{12}} = \frac{M_x - M_n}{2^l\sqrt{12}} \tag{5.4}$$

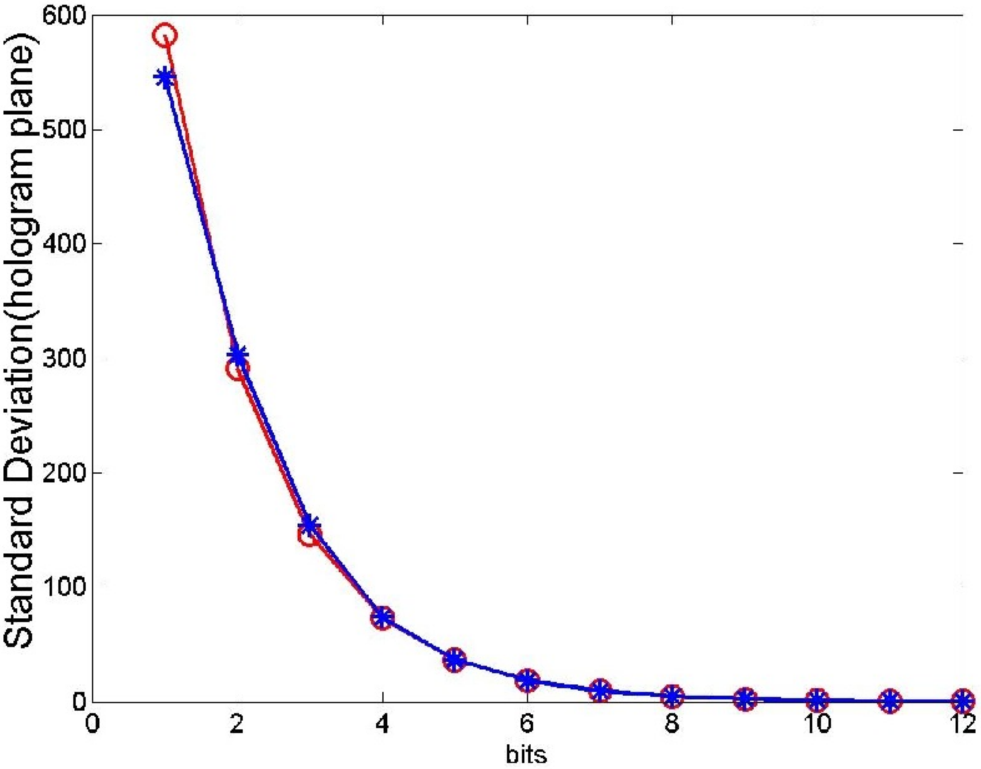

Figure 5.5: Standard deviation of the quantization noise in the hologram plane vs the theoretical prediction.

We calculate the quantization error, Q_l for different values of l in the following way. The acquired 12 bit hologram, H_{12}, is re-quantized (as described in section 5.3.1) down to l bits to generate the lower quantized hologram, H_l. Q_l is signal independent (for low quantization levels) and additive and H_l can be written as $H_l = H + Q_l$. Since $H_{12} \approx H$, this gives $Q_l = H_l - H_{12}$. We can thus calculate the quantization noise for various values of l by computing H_l and subtracting it from H_{12}. In Fig. 5.5, the

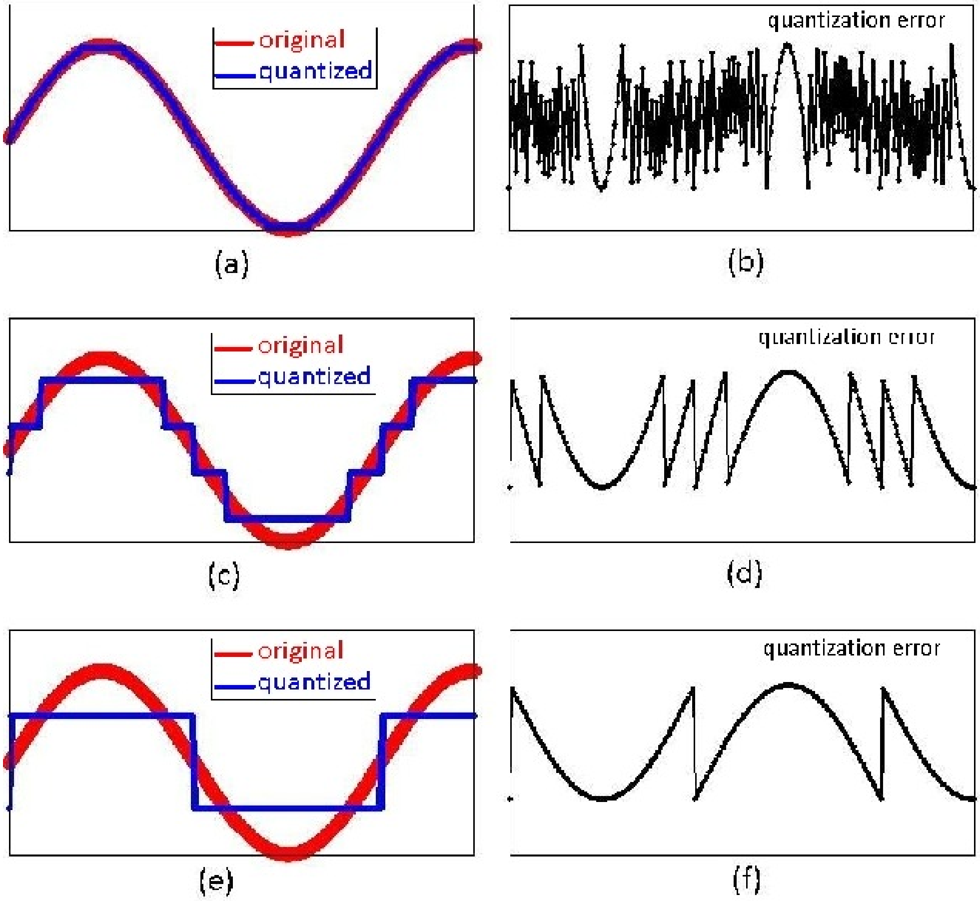

Figure 5.6: Quantization of a sinusoidal signal and the corresponding quantization noise for 3 different cases. (a) and (b) 5 bits (b) and (c)2 bits and (d)and (e)1 bit. It can be seen that for 5 bits the quantization noise has a higher variance (b) and for the 1 bit case(e) it has the particular characteristic frequency of the original signal.

theoretical and actual standard deviation in the quantization noise, Q_l for different values of l (from 12 bits to 1 bit) is shown. The standard deviation closely follows Equation 5.4. The curves closely match except for the 1 bit case where there is a small deviation from the predicted value. This led us to discover that at very low bit levels, the quantization noise carries with it the same structure as that of the hologram, H. This concept is illustrated in Fig. 5.6, where a simple sinusoidal signal is quantized to 32 levels (5 bits), 4 levels (2 bits) and 2 levels (1 bit). The quantized signal and the quantization noise are shown for the 3 cases and it can be seen that when the signal is quantized to the binary case, the quantization noise carries the same characteristic frequency and the shape as that of the signal. Thus the noise is no longer a random white noise but has the characteristic frequency of the signal. This is analogous to the phenomenon of color banding in computer graphics which occurs when there are very few bits per pixel available for representing color. The concept of dithering in signal processing is related to reducing such effects in highly quantized signals [117]. In Fig.5.7, we plot the histograms of the quantization noise, Q_l for l= (a) 8 bits, (b) 6 bits (c) 4 bits and (d) 1 bit. The histogram for the 1 bit case is not uniformly distributed and thus Q_l will contain many of the same frequency components of H for low values of l. This is again clearly demonstrated when we calculate the DFT of Q_l for l=8,6,4 and 1 bits. As we have discussed above, the result of quantizing H at a very low quantizing rate results in an error signal, Q_l, that inherits frequencies of H. The DFT of H is the reconstructed image and therefore we can expect the DFT of Q_l, which we denote as q_l to have resemble the reconstructed image. In Fig.5.8 it can be seen that for the low value of $l = 1$ bit, the object can be seen in the reconstruction of the noise. The 'non-white noise' occurs only at low quantization rates (i.e. 2 bits and less). For other cases, the assumption that the quantization noise in the hologram plane is a white noise sequence holds strongly and we proceed with this assumption for the rest of our analysis. We refer the reader to [118] for a discussion on the conditions for quantization noise to be uniform and white.

5.3.2 Noise due to quantization in the reconstruction plane

In the previous subsection it was shown that the noise in the hologram plane can be described as a uniformly distributed white noise with a standard deviation of $\Delta_l/\sqrt{12}$.

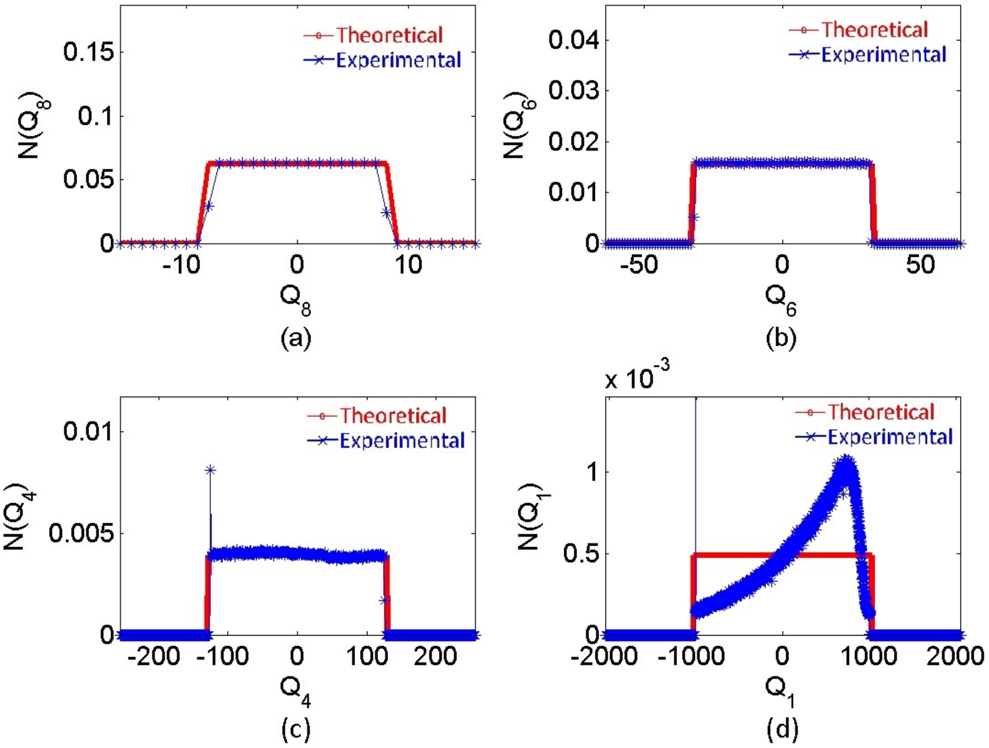

Figure 5.7: Normalized histograms of the quantization noise in the hologram plane. (a) 8 bits. (b) 6 bits. (c)4 bits. (d) 1 bit.

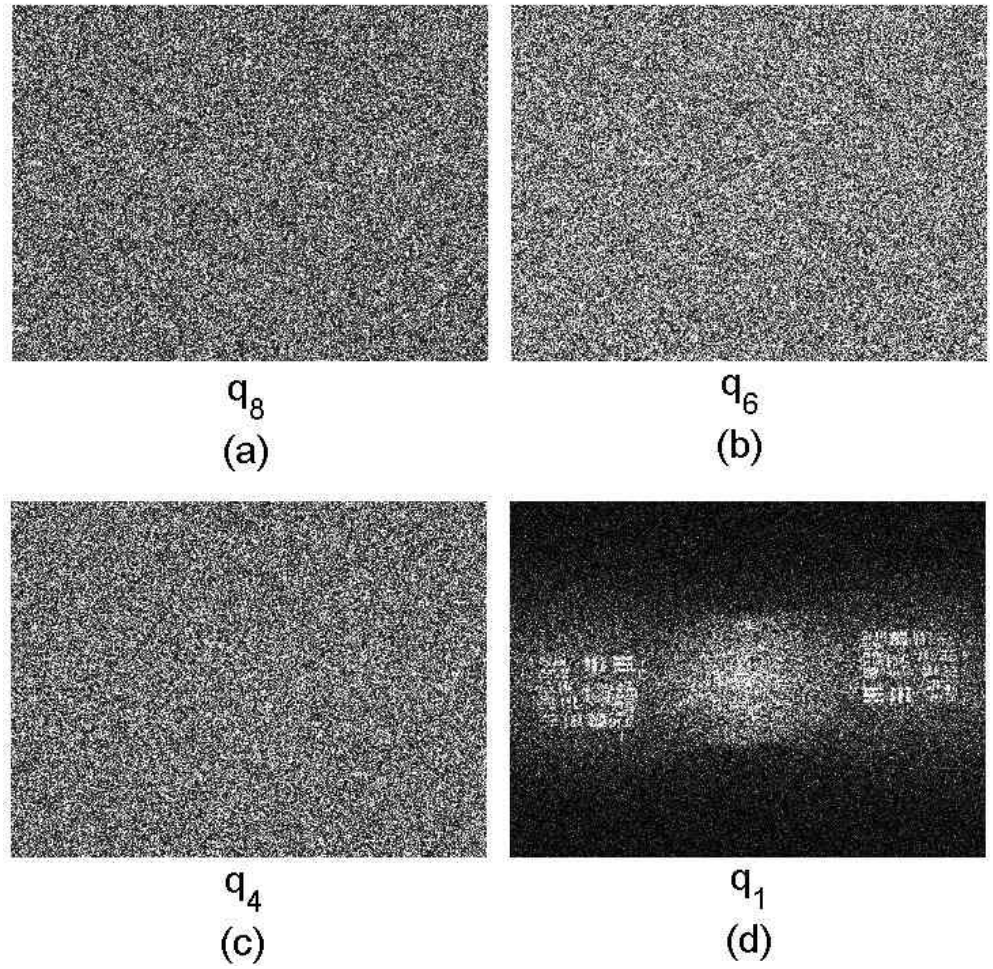

Figure 5.8: Reconstruction at low quantization levels For low bit quantization like 1 bit, the quantization noise in the hologram plane is not uniform and white. This can be seen in the reconstruction from the quantization noise for 4 different cases. (a) 8 bits (b) 6 bits and (c) 4 bits and (d) 1 bit. The reconstruction of the noise for 1 bit is not random and the object can be seen in it.

We are interested in studying the properties of q_l, the resulting noise in the reconstructed image. In lensless Fourier digital holography, the reconstruction is obtained by applying a DFT to the acquired digital hologram. The discrete Fourier transform is a linear operation, therefore the noise in the reconstruction plane is the Fourier transform of the noise in the hologram plane. We now proceed to show that the noise in the reconstruction plane shares the same first order statistical properties as that of speckle. In the case coherent light incident on a rough surface, the resulting speckle pattern can be treated as a random walk and the first order statistical properties can be derived under the assumptions that the amplitudes and phases of the random walk components at each point are statistically independent from phasors at other points and also that the amplitudes and phases are independent of each other. A further assumption is that the phases are uniformly distributed between $-\pi$ and π. In the case of lensless Fourier digital holography, quantization noise in the Fourier plane is the DFT of the noise in the hologram plane. A DFT of white noise can also be considered as a random walk arising from the phases at which the DFT is calculated which are uniformly distributed between $-\pi$ and π. Thus in the Fourier holographic system, the noise in the reconstruction plane has the same first order statistical properties as that of speckle. We proceed to explicitly derive the statistically properties of this noise.

$$h_l = DFT(H_l) = DFT(H + Q_l) = h + q_l \tag{5.5}$$

The statistical properties of the DFT of a discrete random signal can be calculated. We derive here the mean and variance of q_l which is a sequence of complex numbers with the real and imaginary parts given by

$$q_l(k) = R_l(k) + iI_l(k) \tag{5.6}$$

$$R_l(k) = \frac{1}{\sqrt{N}} \sum_{n=0}^{N-1} Q_l(n) \cos\left(\frac{2\pi kn}{N}\right) \tag{5.7}$$

$$I_l(k) = \frac{1}{\sqrt{N}} \sum_{n=0}^{N-1} Q_l(n) \sin\left(\frac{2\pi kn}{N}\right) \tag{5.8}$$

The mean of the real and imaginary parts of the noise, $E[R_l]$ and $E[I_l]$ can be found to be

$$E[R_l] = \frac{1}{\sqrt{N}} \sum_{n=0}^{N-1} E\left[Q_l(n)\cos\left(\frac{2\pi kn}{N}\right)\right] = \frac{1}{\sqrt{N}} \sum_{n=0}^{N-1} E[Q_l(n)]E\left[\cos\left(\frac{2\pi kn}{N}\right)\right] = 0 \tag{5.9}$$

$$E[I_l] = \frac{1}{\sqrt{N}} \sum_{n=0}^{N-1} E\left[Q_l(n)\sin\left(\frac{2\pi kn}{N}\right)\right] = \frac{1}{\sqrt{N}} \sum_{n=0}^{N-1} E[Q_l(n)]E\left[\sin\left(\frac{2\pi kn}{N}\right)\right] = 0 \tag{5.10}$$

where E represents the expectation or the mean value. The real and imaginary parts of the complex quantization noise in the reconstruction plane thus have zero mean.

The variance of R_l can be derived to be

$$\sigma_{R_l}^2 = E[R_l^2] = \frac{1}{N} \sum_{n=0}^{N-1} \sum_{m=0}^{N-1} E[Q_l(n)Q_l(m)]E\left[\cos\left(\frac{2\pi kn}{N}\right)\cos\left(\frac{2\pi km}{N}\right)\right] \tag{5.11}$$

For $n \neq m$, $E[\cos(\frac{2\pi kn}{N})\cos(\frac{2\pi km}{N})] = E[\cos(\frac{2\pi kn}{N})]E[\cos(\frac{2\pi km}{N})] = 0$ and only the $n = m$ terms contribute to the sum. Therefore,

$$\sigma_{R_l}^2 = \sum_{n=0}^{N-1} \frac{1}{N} E[Q_l(n)^2]E[\cos^2 \phi_n] =$$
$$\frac{1}{N} \sum_{n=0}^{N-1} E[Q_l(n)^2]E\left[\frac{1}{2} + \frac{1}{2}\cos 2\phi_n\right] = \frac{1}{N} \sum_{n=0}^{N-1} \frac{E[Q_l(n)^2]}{2} = \frac{\sigma_{Q_l}^2}{2} \tag{5.12}$$

Similarly $\sigma_{I_l}^2 = \frac{\sigma_{Q_l}^2}{2}$ where $\sigma_{Q_l}^2$ is the variance of Q_l. The statistical distributions of the amplitude and the intensity of the complex noise can also be derived. A complete derivation of these statistical distributions with the necessary assumptions and conditions can be found in [119], [120] and [70]. These distributions are summarized in the table below for the case of a hologram having a quantization interval of Δ_l defined in Equation 5.4. The amplitude of q_l which is denoted by A_l is Rayleigh distributed and the intensity, Int_l is exponentially distributed. We validate this theoretical model by calculating a re-quantized digital holograms with 4 bits, H_4 from H_{12} by uniformly quantizing. We can reconstruct these two digital holograms, H_4 and H_{12} using a FFT to obtain the complex reconstructions h_{12} and h_4. In Equation 5.5, we showed that h_l= h + q_l where h was an ideally reconstructed digital hologram. We can write q_l as

Real Part (R_l)	$p(R_l) = \frac{12}{\pi\Delta_l^2}\exp\left(\frac{-12Re_l^2}{\Delta_l^2}\right)$
Imaginary Part (I_l)	$p(I_l) = \frac{12}{\pi\Delta_l^2}\exp\left(\frac{-12Im_l^2}{\Delta_l^2}\right)$
Amplitude (A_l)	$p(A_l) = \frac{24A_l}{\Delta_l^2}\exp\left(\frac{-12A_l^2}{\Delta_l^2}\right)$
Phase (θ_l)	$p(\theta_l) = \frac{1}{2\pi}$
Intensity (Int_l)	$p(Int_l) = \frac{12}{\Delta_l^2}\exp\left(\frac{-Int_l}{\Delta^2}\right)$

Table 5.1: Probability densities of different parts of quantization noise in the Fourier domain.

the difference between the reconstruction of the quantized hologram, h_l and the noise free reconstruction, h. If we assume that for the 12 bit case, $Q_{12} \approx 0$ and $H_{12} \approx H$, we can further assume that $h_{12} \approx h$ and $q_{12} \approx 0$. Therefore we can calculate q_l using the following equation

$$q_l = h_{12} - h_l \tag{5.13}$$

We can thus find out the error in the reconstruction for any quantization rate. In Fig. 5.9, we show the theoretical and experimental histograms of the various parts of the complex noise for the quantization rate of 4 bits. As it can be seen in Fig. 5.9 the statistics of quantization noise matches the theoretically predicted values. We have found similar agreement between theoretical model and the experimental results for quantization at other rates(l=4 bits to 11 bits).

In the previous sections, we examined the characteristics of quantization noise in both the hologram plane and the resulting noise in the reconstruction plane. The reconstruction however is the complex sum of both the complex reconstruction and the complex quantization noise. In the sections that follow, we look at the properties of this complex sum.

5.3.3 Effect of quantization noise on reconstructed phase for phase objects

The phase of the reconstructed image is important in digital holographic microscopy. For quantitative phase contrast microscopy of transparent samples, information about the three dimensional structure is encoded in the phase variations of the reconstructed image. Skydan et al. [121] have studied the influence of quantization on the phase

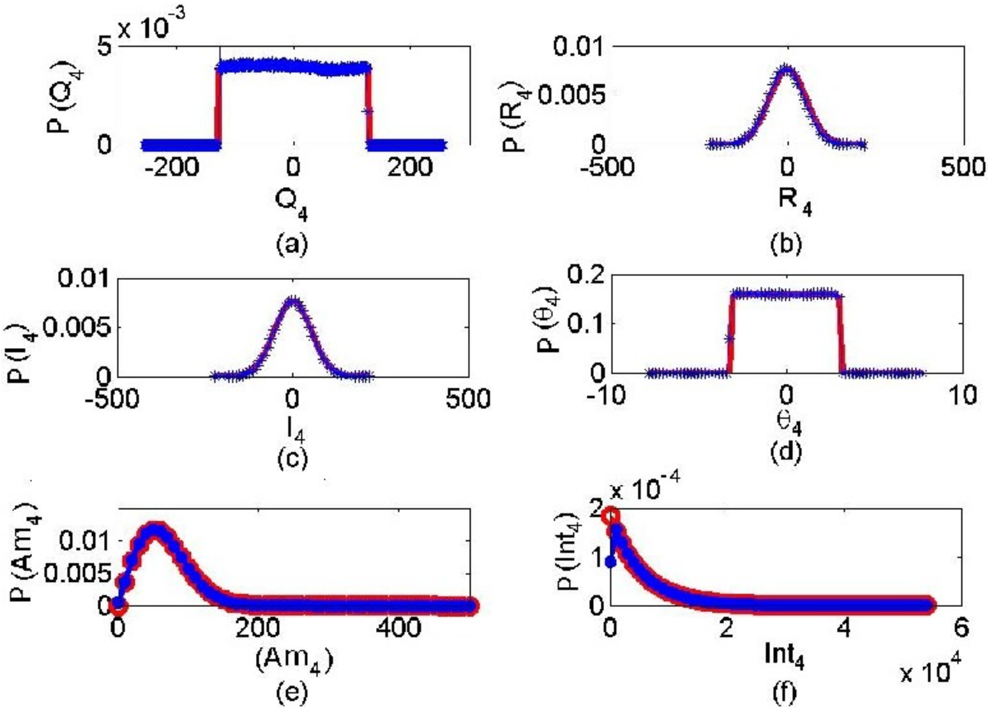

Figure 5.9: Theoretical and experimental probability distributions for various parts of the complex quantization noise in the Fourier plane For the 4 bit quantization case, Red- theoretical. blue-experimental. (a) histogram of quantization noise in hologram plane. (b) distribution of real part of complex noise. (c) distribution of imaginary part of complex noise. (d) distribution of phase (e) distribution of amplitude. (f) distribution of intensity.

error in fringe pattern analysis. In fringe pattern analysis, the phase measurement is performed on the recording plane whereas in digital holography, the phase measurement is performed on a Fourier or Fresnel transform plane. Digital holographic methods have been shown to give sub-wavelength axial resolution of a samples thickness and this is dependent on the accuracy of the phase measurement [54].

The value at every point in our reconstructed image is the complex sum of the ideal reconstruction, h and the complex quantization noise, q_l. The addition of these two vectors is illustrated in Fig. 5.10. The resulting phase of the two vectors is different from the original phase. As seen in the Table 5.1, the phase of the noise in the Fourier domain, θ_l is uniformly distributed between $-\pi$ and π and the amplitude of the noise,Am_l is Rayleigh distributed. As seen in Fig. 5.10, the maximum error in the phase occurs when the noise vector is perpendicular to the signal vector and is minimum when the noise vector is parallel to the signal vector. It is of considerable interest to evaluate the influence of quantization error in phase angle measurement in a statistical manner. We assume that the amplitude of the transmission function of the object under investigation is uniform. For pure phase objects, this is a reasonably good assumption. We denote this amplitude as A. Since we measure the error in phase by subtracting the original phase distribution from the erroneous one this problem is completely analogous to the phase distribution in the resulting sum of a speckle pattern and a coherent background [70] and in the case of coherent noise in MRI data [122]. In the case of the speckle on a coherent background, the background is coherent and uniform and the speckle adds to this coherent background and the resulting phase is given by the distribution above.

The phase error can be defined as the difference between the phase of the original signal(S_o) and the new noisy signal(S_n). The phase error can then be described as

$$\theta_{err} = \angle S_n - \angle S_o \tag{5.14}$$

if $S_o = A\exp(i\angle S_o)$ then $S_n = S_o + N$ and θ_{err} can be written as

$$\theta_{err} = \angle S_n - \angle S_o = \angle[S_n \exp(-i\angle S_o)] = \angle[A + N\exp(-i\angle S_o)] \tag{5.15}$$

In our case, the background is the noise free reconstruction of the phase and is not uniform. But since we calculate the phase error by subtracting the noise free phase reconstruction from the noisy one, our situation is similar to the one of the speckle against a coherent background.

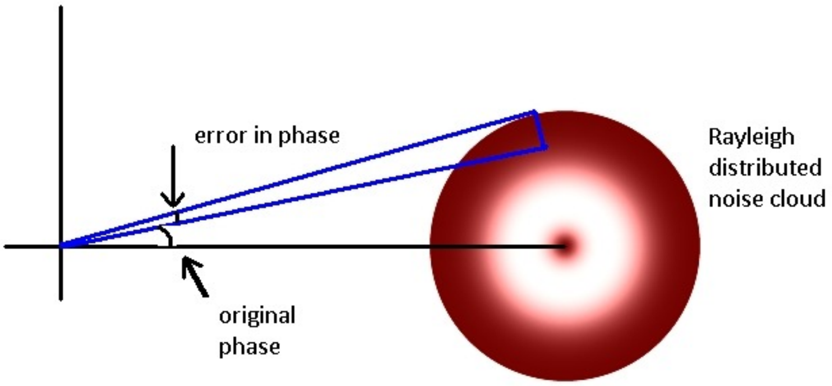

Figure 5.10: Illustration of the result on the phase of the reconstruction q_l is distributed with a Rayleigh distribution and adds on to the original amplitude vector. The net phase detected is the angle subtended by the complex vector sum of the original signal and the complex noise vector.

The probability density for such a phase distribution can be derived to be [123]

$$p(\theta) = \frac{1}{2\pi} \exp\left(\frac{-A^2}{2\sigma_R^2}\right) \left\{1 + \frac{A}{\sigma_R}\sqrt{2\pi} \cos\theta \exp\left(\frac{A^2\cos^2\theta}{2\sigma_R^2}\right) \left[1 - \Phi\left(\frac{A\cos\theta}{\sigma_R}\right)\right]\right\} \tag{5.16}$$

where

$$\Phi(x) = \frac{1}{2\pi} \int_x^\infty \exp(-x^2/2)dx \tag{5.17}$$

and σ_R is the standard deviation in the real part, R. The probability density function is symmetric around the origin as the error can fluctuate in both the directions. For A=0, the phase is distributed uniformly between $-\pi$ to π. For high values of A, the error becomes gaussian and centered around 0 with standard deviation of σ_R/A and Equation 5.17 density can be approximated as

$$p(\theta_{err}) = \frac{A}{\sqrt{2\pi}\sigma_R} \exp(\frac{-\theta_{err}^2 A^2}{2\sigma_R^2}) \tag{5.18}$$

This can be expected as the magnitude of the corrupting phasors becomes small relative to the original signal magnitude. For a high number of bits per pixel representation, the error will be small. From Equation 5.4, the standard deviation in the error in terms of the quantization interval can be written as

$$\sigma_{\theta_{err}} = \frac{M_x - M_n}{2^l\sqrt{24}A} = \frac{\sigma_{Q_l}}{\sqrt{2}A} \tag{5.19}$$

where M_x and M_n as defined previously are the maximum and minimum values in the recorded digital hologram and A is the average amplitude value in the reconstructed object area. A is directly proportional to the product of object and reference powers $(O.R)$ in the hologram plane.

We experimentally verify Equation 5.22 by recording a hologram of a lens using the same experimental setup. This time the illumination is without a diffuser. The object beam passes through a aperture of a small lens. The recorded off-axis hologram and the reconstructed phase are shown in Fig. 5.11. Fig. 5.11 (a) shows the recorded phase hologram. Fig. 5.11(b) shows the reconstructed image. The spatially separated areas carrying the object and the twin image can be clearly seen. Fig. 5.11 (c) shows the amplitude in a section of that area and Fig. 5.11 (d) shows the phase value in that section. We are interested in the error which occurs in this phase section when the hologram is quantized to lower number of levels. We re-quantize the recorded hologram and the phase of the new noisy reconstruction is calculated and subtracted from the original phase of h_{12} to give the phase error. The phase error varies between $(-\pi$ to $+\pi)$. The distribution of the phase error for 4 different cases (a) 8 bits, (b) 6 bits, (c) 4 bits and (d) 1 bit is shown in Fig. 5.12. As it can be seen the phase error can be modeled as a gaussian for all these cases.

In our case the mean amplitude value in the object area in the reconstruction, A is 953 and the fluctuation is less than 20% around this value due to the various experimental issues like spurious reflections etc. This value is directly proportional to the mean amplitude in the reconstructed object area. In order to compare the theoretical probability $p(\theta_{err})$ in Equation 5.19 with the histogram obtained from the experimental data, the theoretical value of standard deviation in the phase error is plotted with the experimentally obtained value for different levels of quantization in Fig. 5.13. The curves show a close agreement. The standard deviation in the phase error decreases by a factor of 2 for every bit added. For 8 bits of quantization, the standard deviation in the error is $\sigma_{\theta_{err}}$=0.00247 radians. This corresponds to approximately 0.0004λ error in surface height measurement in air for a reflection geometry. For the 1 bit case, the $\sigma_{\theta_{err}}$=0.3165 radians and this corresponds to approximately 0.05λ error in surface height measurement in air.

As seen in Equation 5.19, the error in the phase resulting from quantization can be reduced by having a large mean amplitude in the reconstruction relative to the

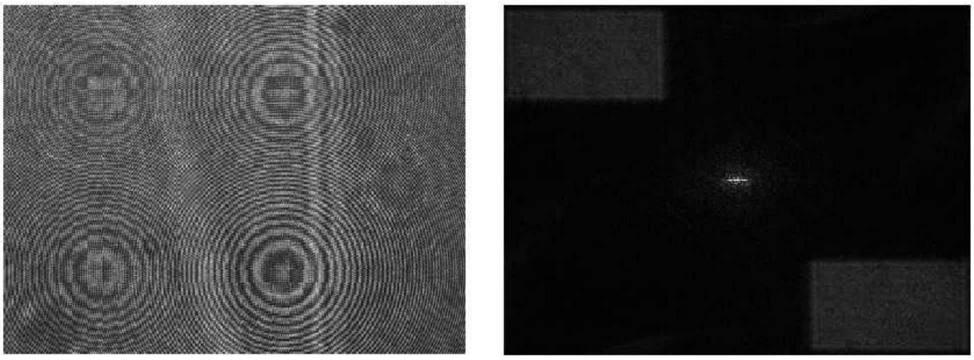

(a) Hologram (b) Reconstruction

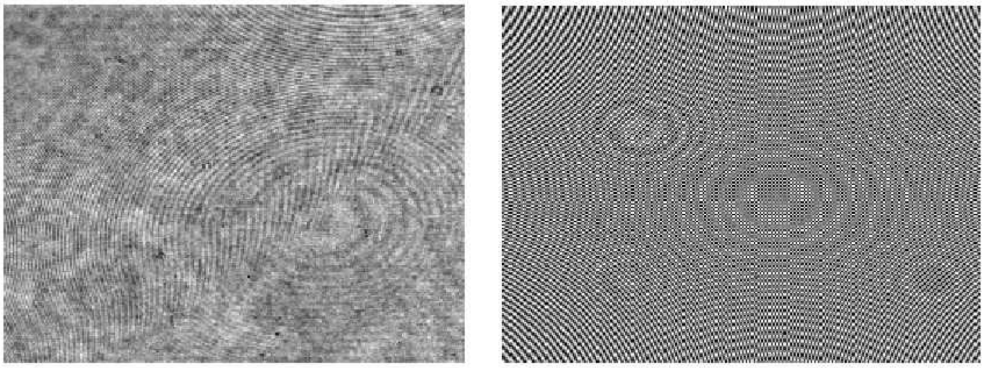

(c) Amplitude(reconstruction) (d) Phase(reconstruction)

Figure 5.11: Hologram of Phase object (a) recorded phase hologram of the a lens, (b) Fourier reconstruction, (c) Amplitude in a 200×250 section of the reconstructed object and (d) the phase distribution in the same area.

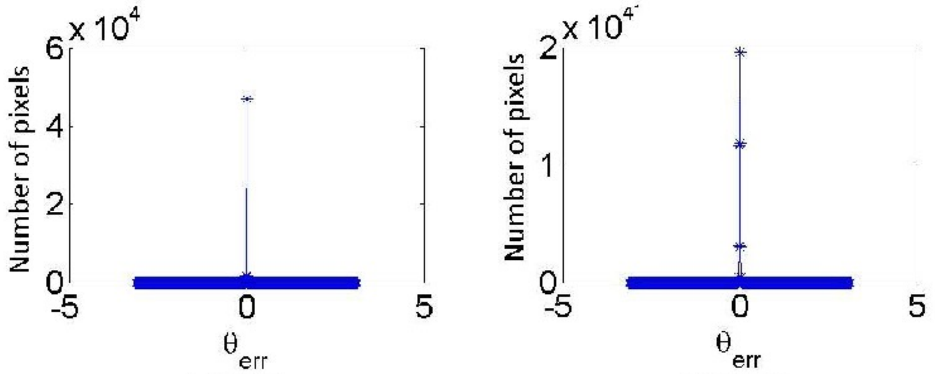

(a) 8 bits (b) 6 bits

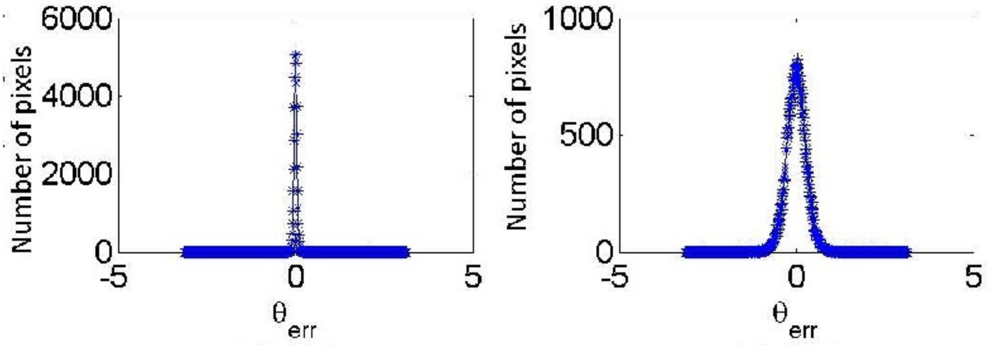

(c) 4 bits (d) 1 bits

Figure 5.12: Error distribution in phase $-\pi$ to $+\pi$ for (a) 8 bits (b) 6 bits (c) 4 bits and (d) 1 bit

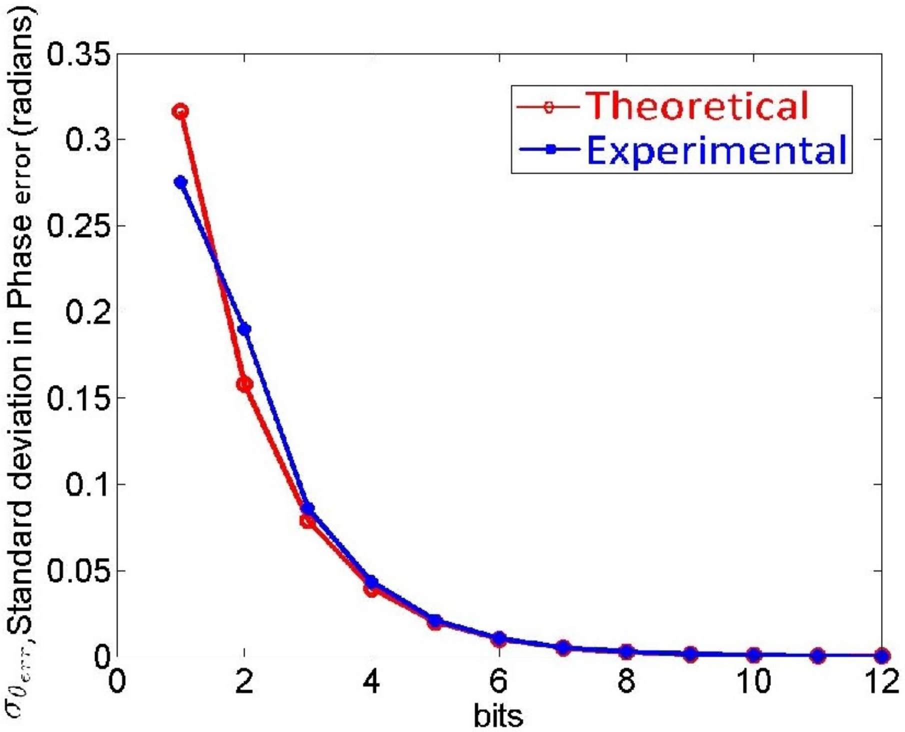

Figure 5.13: Standard deviation of the error in reconstructed phase θ_{err} for different levels of quantization of the recorded phase hologram.

standard deviation in the error introduced due to the quantizer. The mean amplitude can be easily shifted by increasing the exposure. Thus it is advantageous to have a high mean intensity in the reconstruction to reduce the influence of quantization error on the phase measurement.

5.3.4 Effect of quantization noise on reconstructed intensity for 3D objects

Many applications of digital holography such as 3D display, pattern recognition, imaging through occlusions [124] and projection on 2D surfaces [125] rely on the intensity pattern in the reconstruction plane. In this subsection, we analyze the statistics in the reconstructed intensity when quantization noise q_l is present. The intensity of the hologram is

$$|h_l|^2 = |h + q_l|^2 = |h|^2 + |q_l|^2 + hq_l^* + h^* q_l \tag{5.20}$$

which can be written as

$$|h_l|^2 = |h|^2 + |q_l|^2 + 2(Real[h]Real[q_l] - Imag[h]Imag[q_l]) \tag{5.21}$$

This is the sum of 4 terms all of which are independent of each other. Since h and q_l are independent and the real part and imaginary parts are uncorrelated with each other [70], the variance in the sum is equal to the sum of the variances. The total variance in the complex intensity in the Fourier plane can be approximately written as

$$\sigma^2_{|h_l|^2} = \sigma^2_{|h|^2} + \sigma^2_{|q_l|^2} + 4\sigma^2_{Real(|h|)}\sigma^2_{Imag(|q_l|)} + 4\sigma^2_{Imag(|h|)}\sigma^2_{Real(|q_l|)} \tag{5.22}$$

Since $\sigma^2_{Real(|h|)}$ and $\sigma^2_{Imag(|h|)}$ are known apriori, we can use this simple model to calculate the standard deviation in the image for any lower number of quantization levels. $\sigma^2_{Real(|h|)}$ and $\sigma^2_{Imag(|h|)}$ are assumed in our case to be equal to $\sigma^2_{Real(|h_{12}|)}$ and $\sigma^2_{Imag(|h_{12}|)}$ respectively. In Fig. 5.14, we plot the standard deviation in a uniform region in the reconstructed image along with the value calculated using Equation 5.23. The observed value matches the predicted value with high accuracy down to 2 bits. For 1 bit quantization, the predicted value deviates from the observed value. At 1 bit the deviation is 26%. We believe that is due to the onset of 'banding' as explained previously in Fig. 5.6.

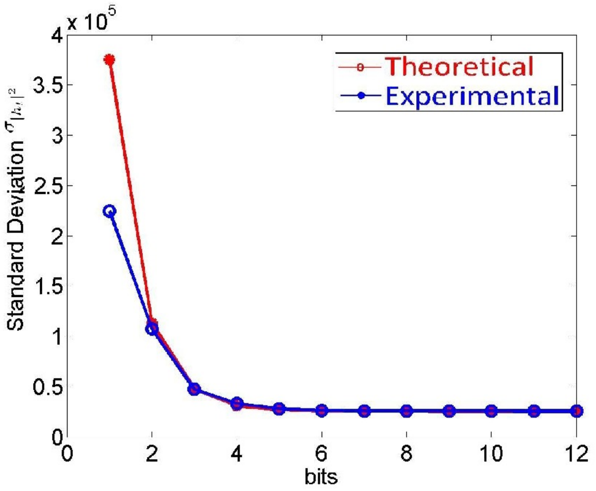

Figure 5.14: Standard deviation in the intensity of the reconstruction plane. Red-theoretical, blue-experimental. We can see that the simple model above can be used to predict accurately the quantization error upto 2 bits (4 levels) of quantization. The deviation at 1 bit comes due to the non-white nature of quantization noise in the hologram plane at binary quantization. In this case, the noise term has a pattern and structure similar to the original signal.

5.4 Shot noise

We have derived a model for the influence of additive noise in the recording plane on the phase value of the reconstructed image. The reconstructed phase is particularly important in digital holographic microscopy. It is also known that at low exposures, the prevalent and the limiting noise is shot noise [126]. For many applications, it is of interest to perform digital holography at low exposures. In biology, for the visualization of fast surface changes of cells and in metrology for vibration measurement, a fast frame rate is needed. In the following sections, we analyze the influence of additive noise in the hologram plane on the accuracy of phase measurement. We analyze Gaussian distributed and Poisson distributed shot noise in the camera plane and we develop a model for quantifying the error in the reconstructed phase.

The influence of shot noise in DHM was first studied by Charrière et al [127] [128]. They have experimentally investigated the influence of the parameters like the gain of the CCD, power in the recording beams and the beam ratio on the standard deviation in the phase error. They also showed methods of reducing shot noise by combining multiple exposures. In [128], the authors used a Signal to Noise ratio (SNR) metric based on statistical decision theory, which is suitable for biological microscopy specimens, to study the influence of recording parameters on the reconstructed holograms in presence of shot noise. In [129], the authors presented a method based on heterodyne holography where they have demonstrated recording and reconstructing images at extremely low signal levels. Yamamoto et. al. have recently demonstrated the possibility of object reconstruction under very weak illumination (43 photons per second) [130]. In such cases, the issue of shot noise is particularly important.

5.4.1 Effect on phase measurement precision

In digital holographic microscopy(DHM), noise occurs in the capture plane at the image sensor. This is always real in nature since it occurs due to the square law detection. The hologram is then reconstructed to extract the phase information of the object. The reconstruction in DHM is generally obtained by firstly filtering the hologram in the Fourier domain to remove the twin image and zero order terms and secondly by computing the Fresnel transform. This gives rise to a second type of noise in the reconstruction plane. Here we show that both the filtering process and the propagation process tend to make the real noise in the hologram plane as a complex Gaussian distributed noise in the reconstruction plane. For our study we use a hologram acquired from a commercial digital holographic microscope (Lyncee-Tec DHM-T1000). This has a transmission off-axis Fresnel architecture. The object we used is a micro-lens array. The hologram is captured under good recording conditions with an exposure time of 314μs. The wavelength used in this system is λ=682nm and the pixel pitch is 6.45μm. The hologram has a size of 1392x1040 pixels and the size of the mask is 450x450 pixels in the Fourier domain. Fig. 5.15(a) shows the hologram.

Fig. 5.15(b) shows the DFT before application of the filtering mask. Fig. 5.15(c) shows the amplitude in the reconstruction and Fig. 5.15(d) shows the phase of the microlenses structure. Any abberations resulting from the setup are removed by capturing the interference patterns when there is no object and reconstructing it. The phase of this reconstruction is then subtracted from the reconstruction of the object. Our acquired holograms has some noise like microscopic dust particles, spurious reflections and other noise sources like readout noise, quantization noise etc but since we are measuring the error in phase upon introducing computer generated noise, the hologram

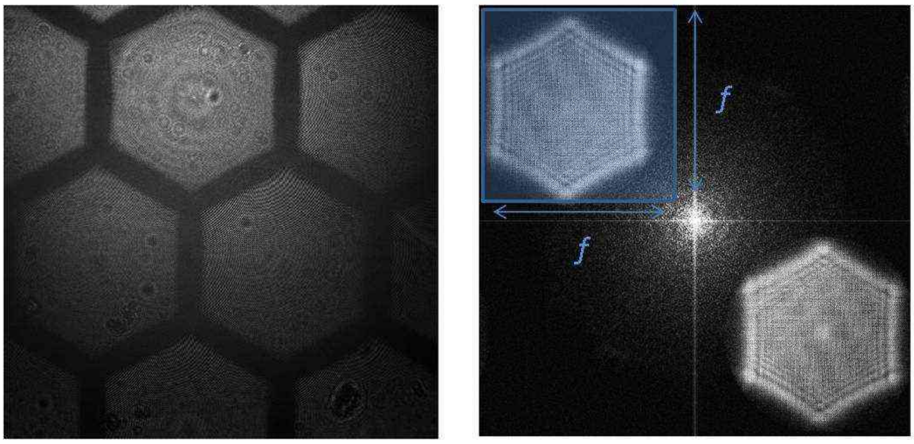

(a) Hologram

(b) Fourier plane

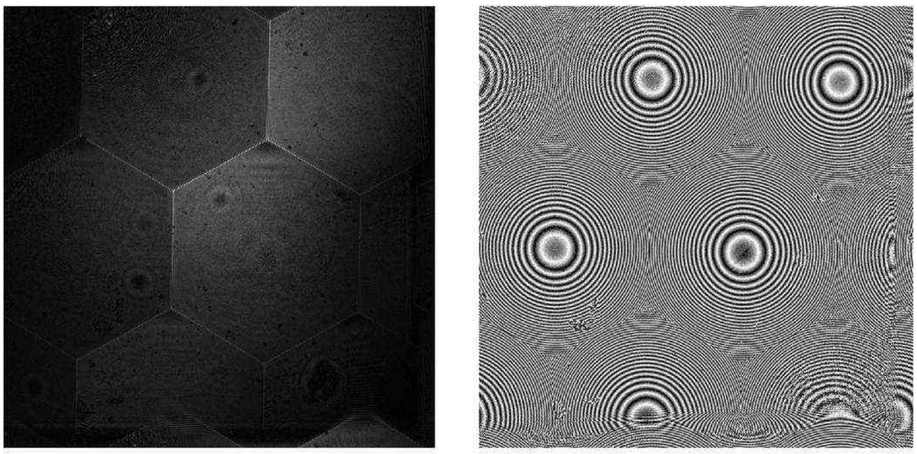

(c) Amplitude
of reconstruction

(d) Phase
of reconstruction

Figure 5.15: Holograms and reconstructions of microlenses (a) Hologram of phase object, (b) Fourier transform showing the filtered area. (c) Amplitude of the reconstruction and (d) Phase of the reconstruction.

we acquire is treated as a benchmark noise free hologram and we compare the noisy reconstructions against this hologram.

5.4.2 Fourier filtering

Fourier filtering is used to remove the zero-order term and the twin image in the hologram. This is accomplished by multiplying with a binary mask in the Fourier plane which has a passband over the object region. The filtering process in the Fourier plane can be viewed as a convolution with a complex sinc(x) function or a Bessel function depending on the shape of the filtering mask. As we filter the hologram, the nature of the noise transforms from uniform real to complex Gaussian. To examine this transformation, we consider real uniformly distributed zero mean random white noise in the hologram plane and study the characteristics of the resulting complex filtered noise. Quantization noise is an example of such a uniformly distributed zero-mean white noise. We use kurtosis as a measure of the peakedness of the distribution of the real and imaginary parts. The kurtosis of a variable x with mean μ and standard deviation σ is defined by

$$K = \frac{< [(x-\mu)^4] >}{\sigma^4} - 3 \tag{5.23}$$

Uniformly distributed variables have a kurtosis of -6/5 while perfectly Gaussian variables have a kurtosis of 0. We perform Fourier filtering on this noise for different filter sizes and calculate the kurtosis of the real and imaginary parts of the resulting complex noise as a function of the filter size.

In Fig. 5.16, it can be seen that the kurtosis of the real part of the noise decreases from 0 to -1.2 as the filter size increases. While the kurtosis of the imaginary part stays almost constant. This is expected as the noise in the hologram plane is real and transitions to being complex when sufficient frequencies are removed. In the case of Fresnel off-axis or Fresnel infocus digital holography, the filter size in the Fourier plane in number of pixels is atleast 1/2 of the number of pixels in the hologram. For this filter size, the noise is complex Gaussian with both real and imaginary points having the same variance.

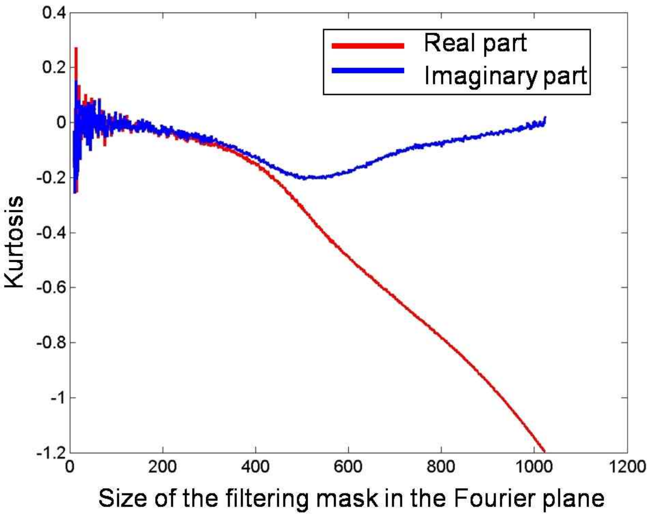

Figure 5.16: Kurtosis of the real and imaginary part of the complex noise resulting from Fourier filtering.

5.4.3 Numerical Propagation

The next step in the reconstruction algorithm is numerical propagation of the retrieved complex waveforms by simulating the Fresnel transform. In DHM, the Fresnel transform is routinely simulated using the convolution approach in which the discrete Fourier transform (DFT) of the filtered hologram is multiplied by a discrete quadratic phase function and then an inverse DFT is performed [131] [132]. This further contributes to the final distribution of the Gaussian noise in the reconstruction plane. This is demonstrated using the equations below for a simple 1D case. Let $H(n)$ be the filtered hologram and D represent its DFT.

$$D(k) = \frac{1}{\sqrt{N}} \sum_{n=0}^{N-1} H(n) \exp\left(-i\frac{2\pi kn}{N}\right) \tag{5.24}$$

$$= \frac{1}{\sqrt{N}} \sum_{n=0}^{N-1} H(n) \cos\left(\frac{2\pi kn}{N}\right) - \frac{1}{\sqrt{N}} \sum_{n=0}^{N-1} H(n) \sin\left(\frac{2\pi kn}{N}\right)$$

Let C represent the discrete quadratic phase factor for a wavelength λ and distance z;

$$C(n) = \exp(i\pi z n^2) = \cos(\pi\lambda z n^2) + i\sin(\pi\lambda z n^2) \tag{5.25}$$

where $n = (n\Delta x)$ for $n = N/2$ to $n = N/2 - 1$ where Δx is the pixel pitch of the camera. The final reconstruction of this is given by

$$O(k) = IDFT[(D(n)C(n))] \tag{5.26}$$

thus giving

$$O(k) = \frac{1}{\sqrt{N}} \sum_{n=1}^{N} D(n)C(n) \exp\left(\frac{2i\pi kn}{N}\right) \tag{5.27}$$

where IDFT is the inverse DFT. For ease of notation, we have ignored some constant phase factors. It can be seen that each value in the final reconstruction O is the result of a weighted sum of the values of the previous DFT. Since the filtering process and the numerical Fresnel transform are both linear and since we assume the noise to be additive, we can say that noise is also 'propagated' using the same algorithm and each value of the noise in the output plane results from the sum of a large number of random values taken from the input plane. The noise term at each point in the reconstruction plane is therefore given by a large sum of randomly weighted phasors, the angles of which are uniformly distributed between $-\pi$ and π. We can use the central limit theorem to conclude that the noise in the reconstruction plane after Fourier filtering and fresnel propagation has Gaussian statistics. The statistical properties of the complex noise are similar to that of speckle. The real and imaginary parts are Gaussian distributed while the amplitude is Rayleigh distributed and the phase of the noise is uniformly distributed in the range $[-\pi, \pi]$.

Let σ_I^2 represents the variances of the real additive noise in the input plane and $\sigma^2_{O_{Re}}$, $\sigma^2_{O_{Im}}$ represent the variances of the real and imaginary parts of the resulting noise at the output plane respectively. By using Parseval's theorem, we can say

$$\sigma^2_{O_{Re}} + \sigma^2_{O_{Im}} = \sigma_I^2 \tag{5.28}$$

Assuming the energy to be evenly distributed between the real and imaginary parts we can assume

$$\sigma^2_{O_{Re}} = \sigma^2_{O_{Im}} = \frac{1}{2}\sigma_I^2 \tag{5.29}$$

We can further say that the variance of the real and imaginary parts of the complex noise, N, are equal to $\sigma^2_{O_{Re}} = \sigma^2_{O_{Im}} = \sigma_I^2/2$. We assume that the noise energy is evenly distributed throughout the frequency domain. If there is a bandpass filter in the frequency domain with a passband of f^2. i.e. the spatial frequency bandwidth of the transmitting mask in the DFT plane is f times the bandwidth of the hologram in both dimensions, then by once again using Parseval's theorem, we can conclude that the final variance becomes $f^2\sigma_I^2$. Thus the real and imaginary parts of the noise in the reconstruction plane have Gaussian distributions both with a variance given by $f^2\sigma_I^2/2$.

5.4.4 Statistics of the error in phase

If we consider the reconstructed signal, S_e to be given by the sum of the noise free signal, S_o and the error inducing noise term. i.e $S_e = S_o + E$. Therefore the phase error can be defined as the difference between the phase of the original noise free signal ($\angle S_o$) and the phase of the noisy signal ($\angle S_e$);

$$\theta_{err} = \angle S_e - \angle S_o \tag{5.30}$$

Letting the reconstruction $S_o = A\exp(i\angle S_o)$, where A is the uniform amplitude in the reconstruction. θ_{err} can be written as

$$\theta_{err} = \angle S_e - \angle S_o = \angle[S_e \exp(-i\angle S_o)] \tag{5.31}$$

since $S_e = S_o + E$, we can write this as

$$\theta_{err} = \angle[(S_o + E)\exp(-i\angle S_o)] = \angle[(S_o + E)\exp(-i\angle S_o)] = \angle[A + E\exp(-i\angle S_o)] \tag{5.32}$$

This shows that the phase error in the reconstruction plane has the same form as that of the phase distribution in the sum of a uniform background of amplitude, A and a speckle pattern. We restate here that our assumption that the object has uniform amplitude in the reconstruction, i.e. A is constant. Such an assumption is valid for phase only objects. In this case the probability distribution of the phase error, $p(\theta_{err})$, can be interpreted as the distribution of phase in the sum of a constant phasor and a random speckle like noise. This is similar to the phase distribution in the coherent sum of a uniform background with the speckle field emitting from a rough surface. The probability distribution of the phase in such a sum has be shown [123] [78] to be

$$p(\theta_{err}) = \frac{1}{2\pi}\exp\left(\frac{-A^2}{2\sigma_R^2}\right)$$
$$\left\{1 + \frac{A}{\sigma_R}\sqrt{2\pi}\cos(\theta_{err})\exp\left(\frac{A^2\sin^2\theta_{err}}{2\sigma_R^2}\right)\left[1 - Q\left(\frac{A\cos\theta_{err}}{\sigma_R}\right)\right]\right\} \tag{5.33}$$

where σ_R is the standard deviation of the real part(or imaginary part) of the complex noise in the reconstruction plane. From our previous analysis this is equal to $\sigma_R = f\sigma_I/\sqrt{2}$ where σ_I is equal to the standard deviation of the noise in the input(camera) plane and

$$Q(x) = \frac{1}{2\pi}\int_x^\infty \exp(-x^2/2)dx \tag{5.34}$$

Equation 5.33 is also used to model the noise in MRI data [122] and in the general case of the phase error when Gaussian noise is added to a complex sinusoidal signal [133]. When $A >> \sigma_R$, Equation 5.33 can be approximated as a Gaussian of the form

$$p(\theta_{err}) = \frac{A}{\sqrt{2\pi}\sigma_R}\exp\left(\frac{-\theta_{err}^2 A^2}{2\sigma_R^2}\right) \tag{5.35}$$

with a standard deviation of

$$\sigma_{\theta_{err}} = \frac{\sigma_R}{A} \tag{5.36}$$

5.4.5 Application to additive white Gaussian noise

Gaussian noise is a general model that is often used in digital signal processing to describe the noise from various sources. The combined effect of all the noises due to quantization, thermal noise, shot noise, readout noise can be described as a zero mean additive white Gaussian noise (AWGN). We numerically generate AWGN with different standard deviations and add them to our sample hologram. The noisy holograms are reconstructed using the convolution method for simulating the Fresnel transform. The phase of the reconstruction is calculated and the standard deviation in the phase error is calculated by least squares fitting the observed distribution to a non-normalized Gaussian. This value is compared with the predicted value given by Equation 5.36. Fig. 5.17 shows the standard deviation in the phase error vs. the standard deviation of the noise in the input plane for both small errors. We see an approximately linear relationship. The phase error starts deviating when the noise standard deviation is increases and this is because of the deviation from the assumption that $A >> \sigma_R$. In this case of high noise, the noise in the capture plane dominates the phase signal. The phase of the reconstructed signal is immersed in noise and the values tend to become uniformly distributed in $[-\pi, \pi]$ and thus with a variance of $\frac{\pi^2}{3}$. Thus the standard deviation in the measured error becomes $\frac{\pi}{\sqrt{3}}$.

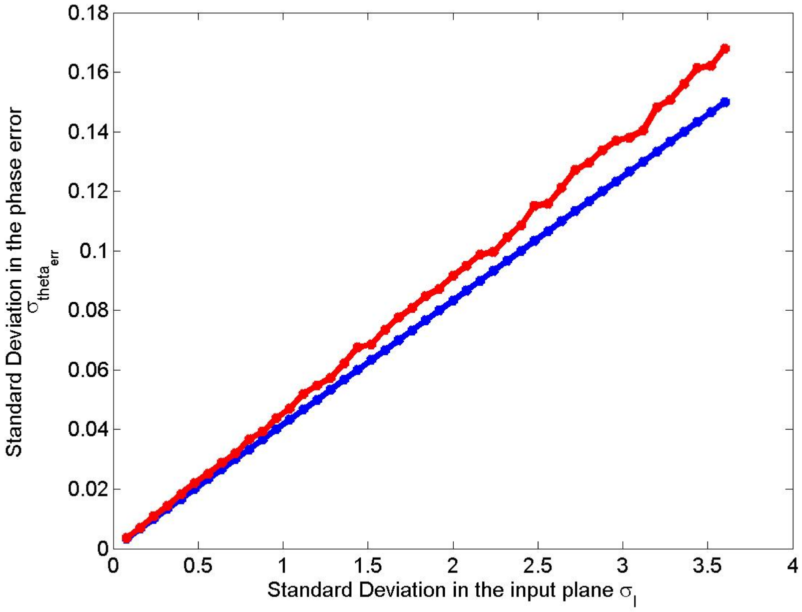

Figure 5.17: Standard deviation of the phase error vs the standard deviation in the camera plane of the hologram for gaussian noise.

At low exposures, the influence of noises like thermal noise and quantization noise can be reduced by cooling the CCD chip and by using a higher bit rate camera respectively. The ultimate noise limitation is due to the fundamental shot noise at low light imaging.

5.4.6 Application to Shot noise

In this subsection, we build on the results of previous subsections to investigate the phase error in DHM when the noise in the hologram plane is generated from a Poisson distribution. Our theoretical model complements the experimental investigations done in [127] [128]. Poisson noise is a data dependent noise which occurs due to the random and discrete nature of the photons and photoelectrons involved in the digital image formation process. It can be treated as additive in nature. This noise is a fundamental limitation to imaging [126] and is particularly influential at low lighting conditions.

Since the amount of shot noise depends only on the signal and not on any other external factors, we can provide an estimate for the phase error based on the power of the signal itself. We can estimate the standard deviation of the shot noise in the following way. An important characteristic of a Poisson distributed variable is that the variance is equal to the mean. The variance of Poisson noise is equal to the mean of the signal μ. Thus the standard deviation is given by $\sqrt{\mu}$. When this hologram is amplified by a factor α, the amplitude in the reconstruction becomes αA and the mean becomes $\alpha\mu$. Once again A represents the amplitude in the reconstructed phase area of the ideal noise free hologram. Substituting these values in Equation 5.36 gives the standard deviation in phase error to be

$$\sigma_{\theta_{err}} = \frac{\sigma_n f}{\sqrt{2}A} = \frac{\sqrt{\alpha\mu}f}{\sqrt{2}\alpha A} = \frac{\sqrt{\mu}f}{\sqrt{2\alpha}A} \tag{5.37}$$

This shows that as the hologram is amplified by increasing α, the standard deviation in the phase error decreases by a factor $\sqrt{\alpha}$. The filter factor f is a constant for the system as discussed in section 5.4.3. It should be noted here that the amplification factor is that of the holographic signal before the recording is made. This can be increased by increasing the power of the illuminating beams or by increasing the exposure time of the camera. It should also be noted that amplification by increasing the gain of the CCD only increases the sensitivity of the photo-detectors but does not decrease the photon shot noise.

In order to verify the theoretical model, we numerically introduce Poisson distributed noise into the hologram in order to simulate the presence of shot noise in our capture and then reconstruct using the convolutional approach. The phase is assumed to be noise-free and it is used as a benchmark to measure the error resulting from the noisy holograms. Poisson noise is signal dependent and to generate different noises, the mean value of the signal is varied by multiplying with a factor α. Each pixel of the scaled hologram is treated as the mean of a Poisson distributed random variable and is replaced by a integer randomly selected from a generated distribution. There are various algorithms for generating Poisson distributed variables [134]. We use the **imnoise** function in Matlab to generate poisson noises for all the holograms with different mean values. These holograms are reconstructed and the noisy phase values are calculated.

A histogram of the phase error is calculated and the standard deviation is calculated by least squares fitting a non-normalized Gaussian to the histogram of the phase error. This value is plotted against the value given by Equation 5.36. Fig. 5.18(a) shows the standard deviation in the phase error for amplification factor(α) from 1 to 125 along with the predicted value from Equation 5.36. Fig. 5.18(b) shows the shot noise in the hologram. Fig. 5.18(c) the phase reconstruction and Fig. 5.18(d) the histogram of the phase error with least squared fit of a Gaussian curve.

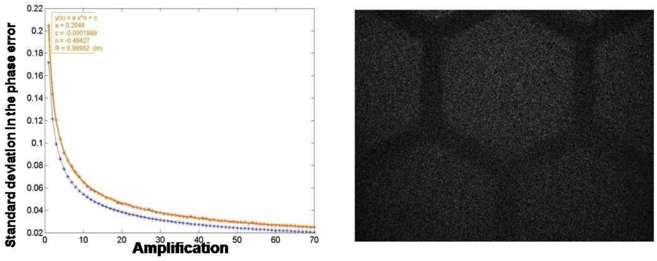

(a) Phase error vs Amplification

(b) Shot noise

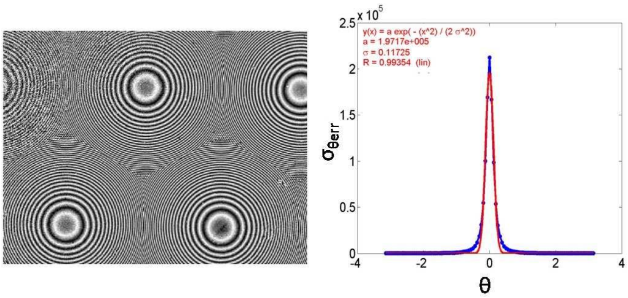

(c) Phase of reconstruction

(d) Histogram of error in phase

Figure 5.18: Standard deviation of the phase error vs the amplification (α) of the hologram. 'blue' curve is calculated using Equation 5.36 and the red curve is calculated by using computer generated Poisson noises for each value of the amplification factor α).

As seen in Fig. 5.18(a), the standard deviation in the phase error follows a $\sqrt{\alpha}$ curve closely. Fig. 5.18 also shows the least squares fit to a function of the form $y = a.x^n + c$ and gives the value of $n = 0.49$ and fit parameter $R = 0.99$, confirming the square root dependence. The same dependence was observed in experimental studies by the authors in [127]. Even though the simulation results and the predicted values follow the same $\sqrt{N}$ dependence, there is a bias in between the curves. There are two important factors for this. In the case of an appreciable modulation of the amplitude, uniform noise in the hologram plane also becomes complex and Gaussian in the reconstruction plane. However the phase error cannot be described by the equations here. The model used here relies on noise being added to a fixed amplitude phasor which is not the case when there is modulation in the amplitude of the signal. Another assumption is one with the nature of the noise due to the Poisson process. It is signal dependent. Thus the assumption that the noise is completely random is not strictly true and thirdly our curve fitting is based on an approximation of Equation 5.33 under the assumption that $A >> \sigma_R$. For low image signal intensities, this assumption is not a strong one as the standard deviation of the Poisson noise is comparable to the signal.

5.5 Conclusion

Quantization error is fundamental to any digital sensor. We have shown that in digital holography, quantization error is introduced as uniformly distributed additive noise in the recording plane (camera plane) and this manifests itself as a complex noise in the reconstruction plane with gaussian distributed real and imaginary parts, rayleigh distributed amplitude and uniformly distributed phase. We have shown and characterized the various statistical properties of this noise both theoretically and experimentally in the case of lensless off-axis Fourier digital holography. We have also discussed the non-white nature of quantization noise at low bit rate (of binary quantization) in digital holography for the first time. We have studied the influence on the phase measurement accuracy and the reconstructed intensity quantitatively. The standard deviation in the phase measurement error increases by a factor of 2 for every bit removed in the quantization process. The effect of quantization noise on the phase can be suppressed (linearly) by increasing the mean intensity of the phase hologram during recording. We have also characterized the noise in the intensity of the reconstructed images. This complex noise can be treated as the result of a random walk in the complex plane and shares the same statistical properties as that of speckle.

We have quantified the influence of the additive noise on the phase measurement error in the hologram plane in digital holographic microscopy under the assumption that the object is highly transmissive in nature. We have shown that in general, the noise in the output plane of a digital holographic system has Gaussian characteristics. This happens due to both the Fourier filtering as well as the numerical propagation of the complex wavefield. We have described the relationship between standard deviation in the error in the camera plane to the standard deviation in the error in the reconstructed phase in the case of Fresnel off-axis geometry. Shot noise which has Poisson statistics is a fundamental noise source for holographic imaging. According to our simple model, the phase error can be decreased linearly by amplifying the image by either increasing the exposure time or by adding multiple exposures as shown in the experiments by the authors in [127]. The reduction in error happens because the amplitude of the reconstructed image increases relative to the perturbation by the noise phasors in a $\sqrt{\alpha}$ fashion where α is the amplification of the holographic signal. Though we have studied the noise due to quantization and shot noise, we believe that the same method can be applied to other kinds of additive noise in the hologram plane for other architectures in digital holography.

6

Noise in digital holography: improvement of image quality

6.1 Introduction

In this chapter, we continue our discussion on noise in digital holography. Here we deal with some techniques to remove the noise or to reduce the influence on the reconstructed image quality. There can be many sources of noise in a practical digital holographic imaging setup, the most important being speckle, twin image, object DC etc. The image quality is also susceptible to vibrations during the recording process, abberations, dust on the optics and spurious reflections. Other important sources include

- Thermal noise in the camera photo-detectors. This occurs because of random thermal fluctuations in the photodetectors.

- Pixel non uniformity noise (PRNU) because of each pixel having a slightly different response [135] and pixel crosstalk between neighboring pixels.

- Computational noise due to the hardware implementation and finite bit representation of the numerical algorithms. This noise is extremely low for modern 64 bit precision computers but is still a noise source and can depend on the algorithm used for reconstructing the image.

- Noise due to vibrations, dust particles, coherent reflections etc.

- Additionally transmission of digital holograms on a channel without error correction can lead to ‘channel noise’ where the bits can be lost or assigned a different value.

Many of these noise sources can be modeled as additive noise source (in the same manner as quantization noise and shot noise) in the sensor plane with their own statistical distributions and the statistics in the reconstructed image that were derived in Chapter 5. The first is a method to remove quantization noise and at the same time improve memory efficiency of the imaging system. This is discussed in Section 6.2. This work was published in parts in [3] and [61]. The second method is a novel method to remove twin image noise in reconstructions of 3D objects. This method has the potential for complete removal of the twin image while preserving the full bandwidth of the camera and without the need for expensive phase shifting devices.

6.2 Quantization noise reduction using speckle reduction techniques

Following from our theoretical model described in Chapter 5, we propose and experimentally validate a method to reduce the noise in the reconstructed intensity resulting from quantization using a speckle reduction technique. This is achieved by moving a diffuser to generate statistically independent speckle patterns. Since the speckle pattern is generated by a moving diffuser with approximately uniform transmittance and the quantization rate is constant for all the different captures, the mean value of these intensity patterns is approximately constant. When N statistically independent intensities are added together, the variance of the sum increases N times and the standard deviation increases $\sqrt{N}$ times but the mean value of the sum increases N times. Thus the coefficient of variation also called the speckle index [79, 80, 81] which is the ratio of the standard deviation to the mean in this case decreases as $1/\sqrt{N}$.

We experimentally prove this by capturing a number of different statistically independent speckle patterns of the object. This is achieved by moving a diffuser on a translational stage with steps of 1mm. The resulting holograms are quantized to the binary level (1 bit per pixel) and reconstructed. The reconstructed intensities for all the different reconstructions are added together. Speckle reduction dramatically increases the quality of reconstruction. In Fig. 6.1, the speckle index is plotted with respect to the number of diffusers added. The results show a well matched $1/\sqrt{N}$ dependence. The results are shown for the extreme 1 bit case where the quantization noise is at a maximum. We mention that in the case of Fresnel geometry, where the twin image occurs as an out of focus noise, speckle reduction can be used to suppress the twin image [59]. A single hologram acquired by a typical camera requires 12 bits per pixel which uses the same memory as that of twelve 1 bit holograms. To give another comparison with respect to memory usage we show in Fig. 6.2 two reconstructions. One from an individual 12 bit hologram and the other the intensity summed from twelve 1 bit holograms. The summation from twelve 1 bit holograms gives a better reconstruction than the case from one 12 bit hologram even though both of them utilize the same memory. For comparison with a 1 bit hologram, the reader can refer to Fig 5.4(h). Of course, it can be argued that this method of capturing requires more time and requires moving diffusers but there are significant advantages like better contrast and improved detail in the reconstruction for the same memory of storage of holograms. Since a binary capture sequence is inherently fast on hardware, the capture time can be reduced to be the same as that of a single 12 bit or 8 bit image capture. Another advantage is that binary ferroelectric SLMs have much faster switching rates (in kHz) than multi-phase LCOS SLMs which are around 80-90 frames per second. Thus multiple binary holograms could be captured, transmitted over network/hardware bus with minimal latency and displayed in a fast amplitude or phase SLM for 3D display and projection applications. When a captured hologram is displayed on a SLM, this can be used to generate improved reconstructions. The different speckled holograms are displayed at a fast frame rate, such that many holograms are averaged over the integration time of the eye and a speckle and quantization noise reduced image is perceived. This technique has been demonstrated in the area of computer generated holographic projection where the different holograms are computed and given a random phase pattern [125]. We have obtained the same results for reflective objects as well.

6.3 Twin image reduction with a scanning aperture

The twin-image noise occurs as an out-of-focus speckle pattern overlapped on the objects image. In this section, we describe a novel method to completely remove the twin image noise in digital holography while using the full bandwidth of the CCD. Unlike

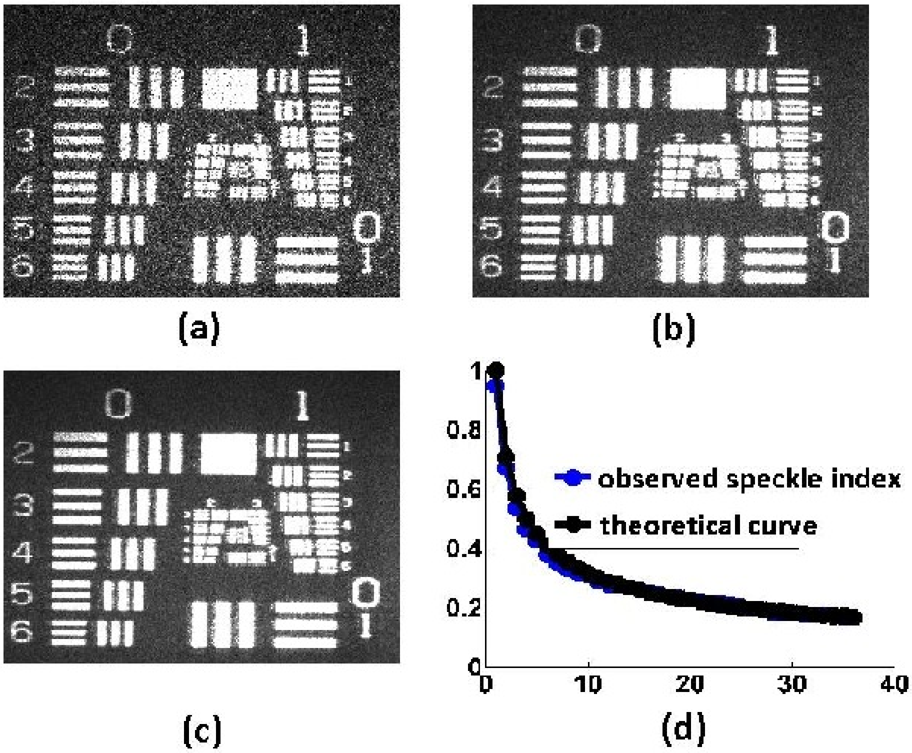

Figure 6.1: Results for speckle reduction on binary holograms (a) 4 diffuse holograms added together, (b)16 patterns (c)36 patterns (d) Speckle index in the image. (black-theoretical,blue-observed.

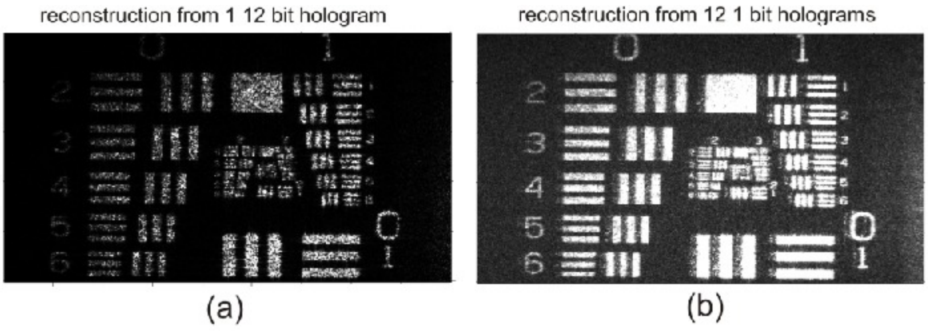
reconstruction from 1 12 bit hologram

reconstruction from 12 1 bit holograms

Figure 6.2: Comparison of reconstructions utilizing the same memory. (a) a single 12 bit hologram, and (b) reconstructions obtained from 12 1 bit holograms. Both the reconstructions involve the same amount of memory usage(in bits)

the traditional off-axis method, the full bandwidth of the CCD is utilized and unlike the previously discussed method of statistical averaging, this method returns the full complex wavefield. The performance is comparable to phase shifting techniques even though expensive and high precision piezoelectric devices are not required. The method exploits the fact that the twin (or virtual) image is the conjugate of the real image. It is most suitable for recording digital holograms of macroscopic 3D objects but can also be applied to DHM. Consider the in-line hologram of the stormtrooper object. The twin images's conjugate property means that the noise resulting from the top of the object will appear at the bottom of the reconstructed image. In other words, if the object taken as a whole is in-line with the reference wave, parts of the object are still off-axis to the reference wave. If these parts are illuminated separately, the twin image noise resulting from them can be isolated and removed from the reconstructions. The concept is illustrated in Figs. 6.3 and 6.4.

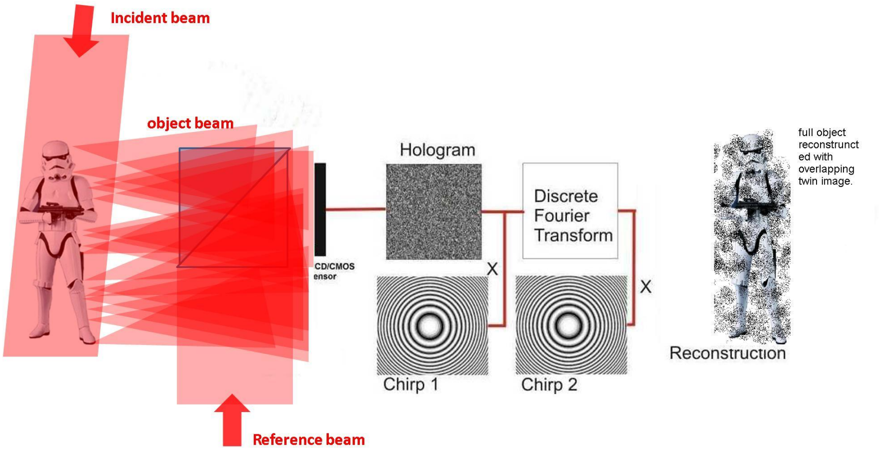

Figure 6.3: Reconstruction of an inline hologram showing overlapping twin image noise

The methodology followed is as follows

1. The object is placed in-line with the camera st the closest distance possible so that the full bandwidth of the camera can be used.

2. A slit like aperture (typically of 0.2 - 0.25 of the object's size) is placed in between the object-camera path.

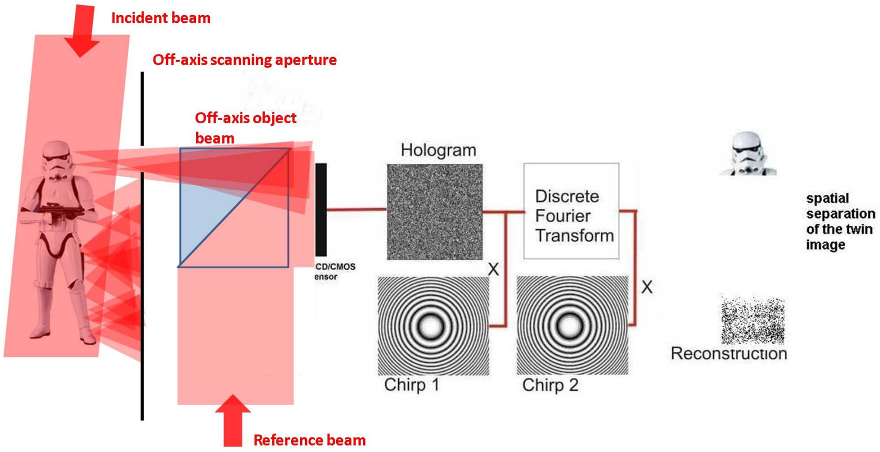

Figure 6.4: Reconstruction of an inline hologram with an off-axis aperture

3. Holograms are captured as the aperture is scanned across the object. It is preferable to scan across the longer dimension.
4. These holograms are effectively off-axis holograms(except for the case where the aperture is in-line with the optical axis and the reference beam).
5. The twin image is filtered from each hologram and the complex reconstructions are added together to yield the twin-free complex reconstructions.

Fig. 6.5 (a) shows the hologram obtained without any aperture. It is a in-line Fresnel hologram. Fig. 6.5 (b) shows the Fourier plane of the hologram where it can be seen that the twin image is overlapping on the object. Fig. 6.5 (c) shows the setup used in this experiment. The object is the stormtrooper figurine shown in Fig. 6.5 and is placed 190mm away from camera (cam3 in Table A.1).

Fig. 6.7 shows the reconstruction of the inline hologram of the object. The zero-order has been filtered. The twin image noise can clearly be seen degrading the object's image.

Fig. 6.8 shows the same reconstruction using Phase shifting. The twin image has been completely removed.

Fig. 6.9 shows the reconstruction obtained from this technique. Comparing it with Fig. 6.8 and Fig. 6.7, we can see that the twin has been significantly reduced.

The aperture is placed on a translational stage. The aperture is scanned from the top to the bottom in steps of 3mm and the holograms are acquired. Fig. 6.6 shows

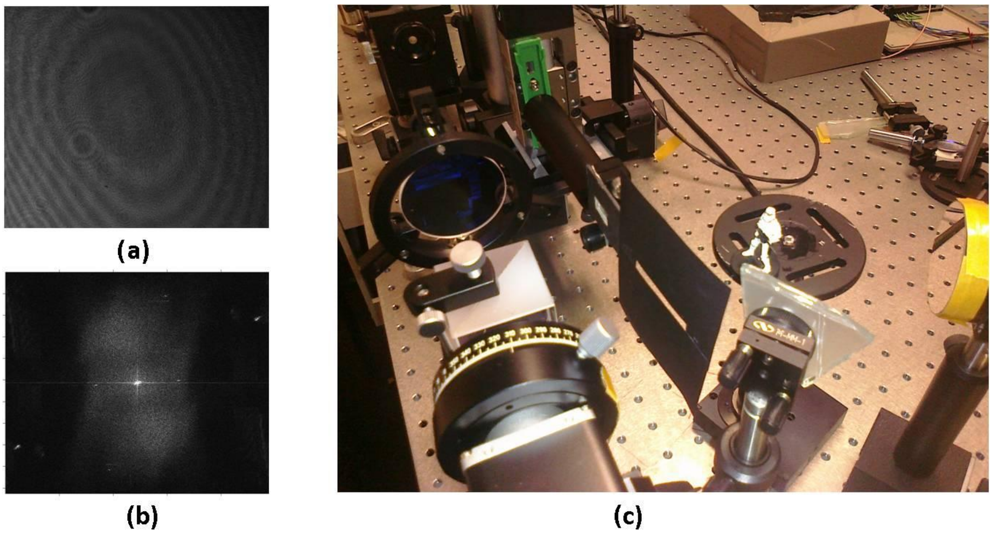

Figure 6.5: Setup used for aperture scanning. (a) The original in-line Fresnel hologram without the aperture. (b) The Fourier transform of the hologram showing the overlapping orders. (c) The setup used for aperture scanning. The aperture is attached to a translational stage

the Fourier transform of the hologram obtained at different positions of the aperture. The zero-order term is high pass filtered. As it can be seen in Figs. 6.6 (a)-(c) and (e)-(f), the twin image can be separated but in Fig. 6.6 (d), the two images overlap because the aperture is now in line with the optical axis. For this particular aperture position, the twin image can not be removed but it can be completely removed for the cases (a)-(c) and (e)-(f). The twin image is filtered and the object is reconstructed and all the complex reconstructions from different aperture positions are added together to yield the twin-free reconstruction.

6.4 Conclusion

We have suppressed this noise by using a speckle reduction technique and have shown good quality reconstructions with binary holograms when speckle reconstruction is performed. We have shown improved reconstructions while using the same amount of memory in storing the holograms. Though we have studied the noise due to quantization, we believe that the same method can be applied to other kinds of additive noise in the hologram plane. We also proposed a novel method for reduction of the twin image

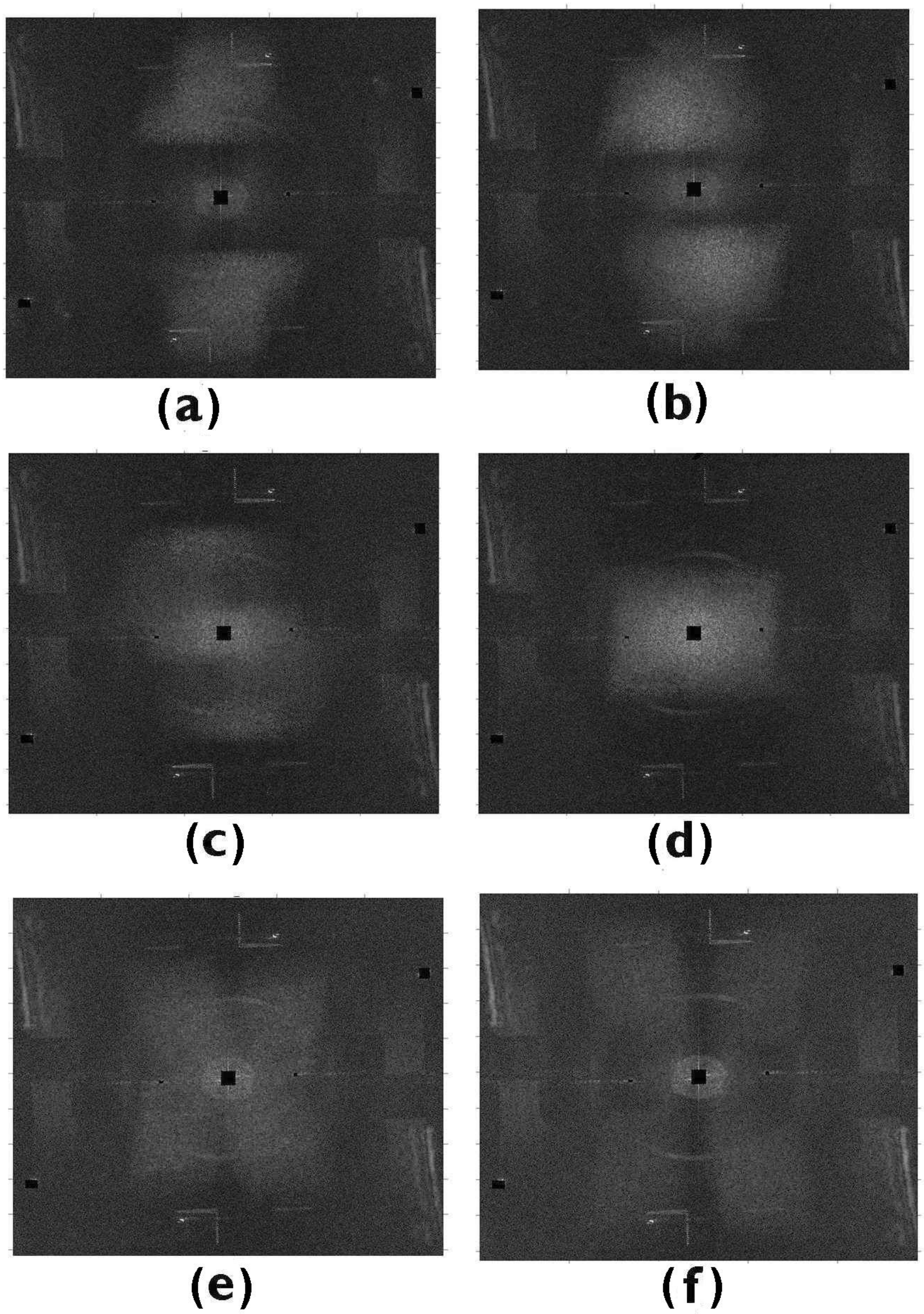

Figure 6.6: Fourier transforms of the holograms for different aperture positions The spatial orders separate when the aperture is off-axis.

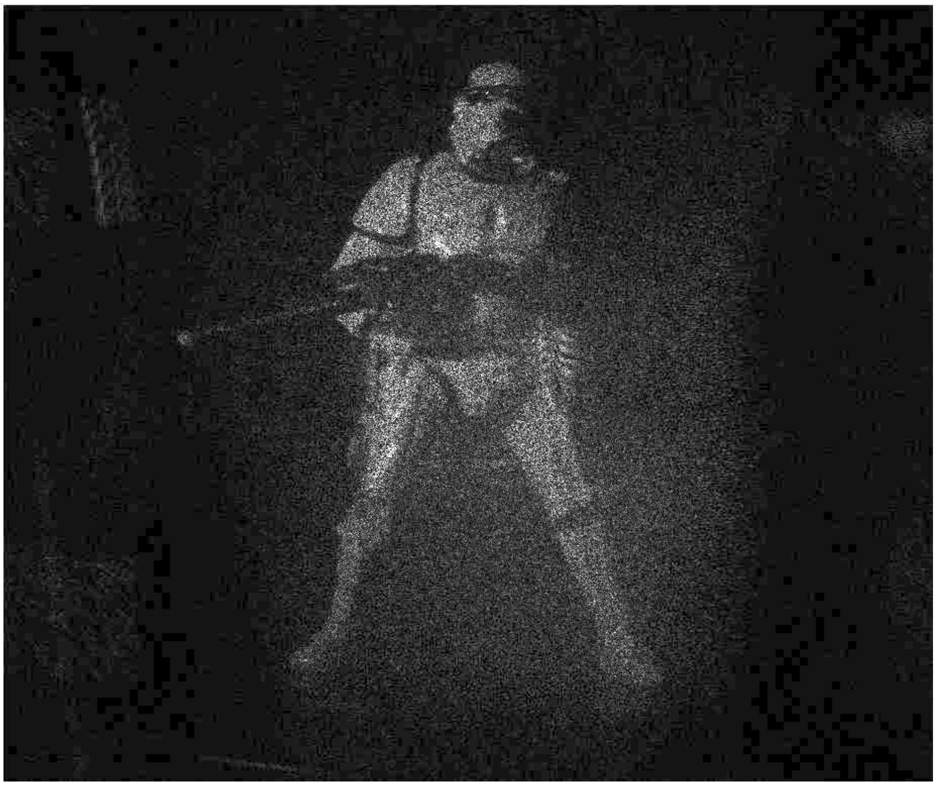

Figure 6.7: Reconstruction of the inline hologram The object and the twin image noise can be clearly seen. The zero order term has been removed by high pass filtering.

Figure 6.8: Reconstruction using phase shifting The twin image noise has been completely removed.

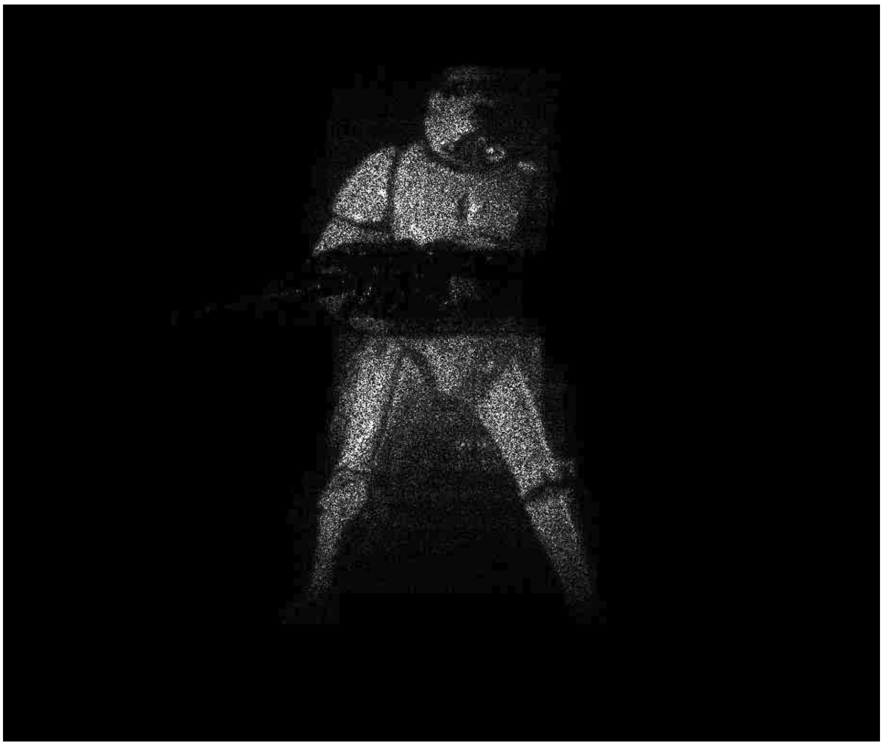

Figure 6.9: Combined reconstruction with all the different aperture positions The twin image noise has been significantly separated.

based on a scanning aperture. This method does not require expensive phase shifting devices and it preserves the camera bandwidth. It does require a translation stage and subsequent image processing to filter the twin image.

7

Perspective enhancement and bandwidth improvement by synthetic aperture

7.1 Introduction

In Chapter 4, we discussed the speed up of reconstruction algorithms in digital holography and in Chapters 5 and 6, we focused on understanding the influence of noise and improving the quality of reconstructions by reducing noise. These efforts were aimed towards improving practical implementations of digital holographic imaging systems. Another important issue with the use of digital holograms for 3D display is the issue of low range of angular perspectives in the reconstructed image. As discussed in chapter 3, digital holograms can be replayed on a spatial light modulator. The total angular perspective of the 3D object which is replayed depends on the aperture of the hologram (i.e. the total dimension of the digital hologram). In many instances, it is desirable to increase the aperture of the camera so that a wider field of view can be captured. For example, in digital holography using an infra-red light source, the thermal cameras are typically in the order of 640x480 pixels in size and get quite expensive as the size increases.

One of the techniques which can be used to improve the image resolution and the angular perspective in such cases is to perform aperture synthesis. In this chapter, we look at another form of improvement in digital holographic imaging by synthetically increasing the aperture of the camera. This technique is called 'synthetic aperture'. Aperture synthesis or 'synthetic aperture' refers to the techniques in which several individual coherent signals are appropriately combined to yield a high resolution signal. We begin this chapter with a review of the literature in synthetic aperture digital holography in Section 7.1. In Sections 7.2, we discuss the increase in resolution and angular perspective of the reconstruction due to synthetic aperture. In sections 7.3 and 7.4, we introduce two methods for synthetic aperture. The first method is implemented by rotating a beamsplitter in the path of the object beam and the second one is implemented by translating a camera and capturing phase shifted holograms at each camera position. We discuss the algorithms to join these holograms in both cases.

7.2 Review of synthetic aperture in digital holography

Synthetic aperture imaging was first developed in the 1960s at radio wavelengths by Martin Ryle [136] and coworkers from the Radio astronomy group at Cambridge. Since then, this concept has led to the rise of fields such as synthetic aperture radar (SAR) [137], synthetic aperture sonar [138] and synthetic aperture magnetometry [139]. These techniques have also been adapted to optical microscopy [140]and digital holography in various forms and recording geometries. In [141], the author has implemented a method in which a camera is translated across a plane and multiple captures are taken and combined. A larger camera will capture a larger solid angle of the object beam and thus will lead to an increased perspective. The author translated a camera manually on a translational stage in both x-y directions and obtained a strongly improved resolution and reduced speckle size in the reconstruction. The setup is for off-axis lensless fourier digital holography using a spherical reference beam which is generated by using a concave mirror. Another effective way of achieving synthetic aperture increase was presented by Binet et.al [142]. This method uses a static camera placed in the far field of the object wavefield. The object is rotated by very small angles (0.130° +/- 0.005°) so that the speckle does not decorrelate in between subsequent captures. Another method was proposed by Hennelly et.al [143]. It involves the rotation of a mirror in the path of the object beam to direct different parts of the beam to the camera and then joining the holograms together by determining the shift after correlating.

In another method, authors Di. et. al.[144] used a linear CCD and scanned it on a precision translational stage to build a 2D hologram. Since they did not use a 2D array, no correlation was performed to obtain to register the hologram. In their experiment, the precision translation stage was automatically controlled by computer to move in the y direction with a constant velocity of 6.863×10^{-4}m/s, and the linear CCD is triggered to frame a picture every 0.0102s. In 51s, they recorded 5000 pictures and then orderly patched them to form a 5000 × 5000 pixel digital hologram with a large area of 3.5cm × 3.5cm. They demonstrated the numerical reconstruction result of a 4mm object at a recording distance of 14cm with a theoretically minimum resolvable distance of $2.57\mu m$. Another method to perform synthetic aperture without any scanning type of motion was proposed by Kreis and Schluter [145]. Here they show a increase in effective NA in holographic microscopy which is also briefly discussed in Section 7.2 of this thesis. They theoretically found the point spread function (PSF) of a double camera non-overlapping Fourier holography system and showed that it is the point spread function of a single aperture multiplied by a cosine whose spatial frequency depends on the separation of the two apertures. It is narrower than the single aperture PSF and thus leads to an improved resolution. They propose two methods to generate synthetic aperture. The first method is the individual reconstruction of both complex fields and their sub-sequent superposition and the other method is the embedding of the two holograms into one large matrix of zeroes and the reconstruction of the effective wave field from this large synthetic hologram. In both cases it is crucial to know the exact mutual positioning of the CCDs for determining the shift of the second reconstructed field relative to the first one when superposing or for fixing the positions of the digital holograms in the large synthetic hologram. This exact position is found out by recording circular fringes on the camera-gap-camera system and doing a least squares fit on the fringes to find the distance between the centres of the two circles.

In the area of digital holographic microscopy, Alexandrov et. al. [146] proposed a method in which amplitude and phase images are synthesized from a set of digital holograms of different regions of the two-dimensional complex spatial Fourier spectrum of a wave after interaction with a sample. Selection of an area of the Fourier spectrum is performed via control of the angular and/or spectral properties of the illumination and collection light fields. They show high-synthetic-NA (numerical aperture) images containing spatial frequencies that are outside the modulation transfer function of the objective. Zhang et.al. [147] have kept the camera stationary but moved a planar object laterally across the optical axis. The object region is illuminated with a broad beam so that the object lies within it wherever it is moved. They used an intensity correlation from each sub-hologram to find the relative shift and stitched 4 sub-holograms together. Exact improvement was not quantified but visual improvement in the scene was observed.

Here we implement two novel methods of synthetic aperture in digital holography. The first method is a modification of the method proposed by Hennelly et.al [143]. The novelty here is that the correlations are performed on complex wavefields obtained after phase shifting digital holography. This ensures that the full bandwidth of the camera is used up and that the reconstructions are free from the twin image.

7.3 Impact of synthetic aperture on perspective and resolution

As discussed in Chapter 3 the resolution of the reconstructed image is determined by the source wavelength, λ, the recording distance, z, and the camera aperture size D_x and D_y. It is approximately given by $D_x\lambda z$ and $D_y\lambda z$ in the two dimensions and the resolution of the image is given by the inverse, i.e. $R_x = \lambda z/D_x$ and $R_y = \lambda z/D_y$. Reducing z or λ, will improve the resolution. However, as we discussed in Chapter 3, the minimum value of z must be chosen meet a constraint that is determined by the sampling rate of the camera where there are different constraints for in-line and off axis recording architectures. In general we will not be able to control λ in our setup, and since z will be limited to some minimum value, the only means available to us to increase the resolution in the reconstructed image is to increase the camera aperture size, D_x and D_y. This can be achieved by making multiple captures and stitching these captures together to create a synthetic aperture that is much larger than a single camera aperture. For synthetic Aperture in the macroscopic case we are simply increasing the effective aperture of the system by stitching together multiple captures. In each capture we take a different window in the hologram plane and thus we increase the effective aperture of the system and reduce the resolution. The resolution in x and y is inversely proportional to D_x and D_y respectively. For synthetic aperture in the microscopic case, we can again increase the effective aperture of the system by stitching together multiple captures. This time in each capture we take a different window in the plane of the microscopic objective which should be roughly matched to the camera aperture. In this way we can increase the effective aperture of the microscopic objective. Again the resolution is proportional to the aperture and the distance the object is placed from it, but this time the relationship is not linear, see Equation (55) Section 8.6 in [70] where the resolution of a coherent microscope is defined as $0.82\lambda/\mathrm{NA}$, where NA is the numerical aperture of the system, see section 4.8.2 in [70].

In the figures below we plot the improvement in resolution against the number of contiguous captures that are stitched together using SADH. In Fig. 7.1 (a) we show the improvement in resolution for the 1D macroscopic case when the camera aperture, D_x = 1cm, the distance from camera to object is z = 20cm and the source wavelength λ = 500nm. The figure shows the improvement in resolution through 10 contiguous captures. We note that after 10 captures the synthetic aperture has a size 10cm. In Fig. 7.1 (b) we show the theoretical improvement in resolution for 10 contiguous captures in the microscopic case when the distance the object is placed from the MO is given by z =5mm, the MO aperture has a diameter A = 5mm and again λ = 500nm. Here we define resolution to be equal to $0.5\lambda/NA$. In both the macroscopic and microscopic cases we can see a considerable improvement in resolution after 10 captures. We note however to achieve the same improvement in resolution in both the x and y dimensions would require 10^2 captures. We also note that in the case of DHM, synthetic aperture has the end result of providing an increased field of view. What we mean by this is that is possible to achieve a resolution that is close to the diffraction limit using an appropriate MO. In this case there will be little improvement in resolution using synthetic aperture digital holography (SADH) techniques. In this case we also note that we will have the smallest possible range of the object under investigation. With smaller magnification we will a larger span of the object but the resolution will be increased. Using SADH, the resolution of this image may be improved.

At this point we must mention the relationship between camera aperture and perspective in in the case of macroscopic DH. Resolution is not an issue this case in the same way as it is in the microscopic scenes in DHM. When a DH is displayed on an SLM, the human eye will often be the limiting aperture in the system and it will therefore define the resolution of the image viewed by the observer as well as the speckle size. The position of the eye, relative to the SLM will determine the perspective. So long

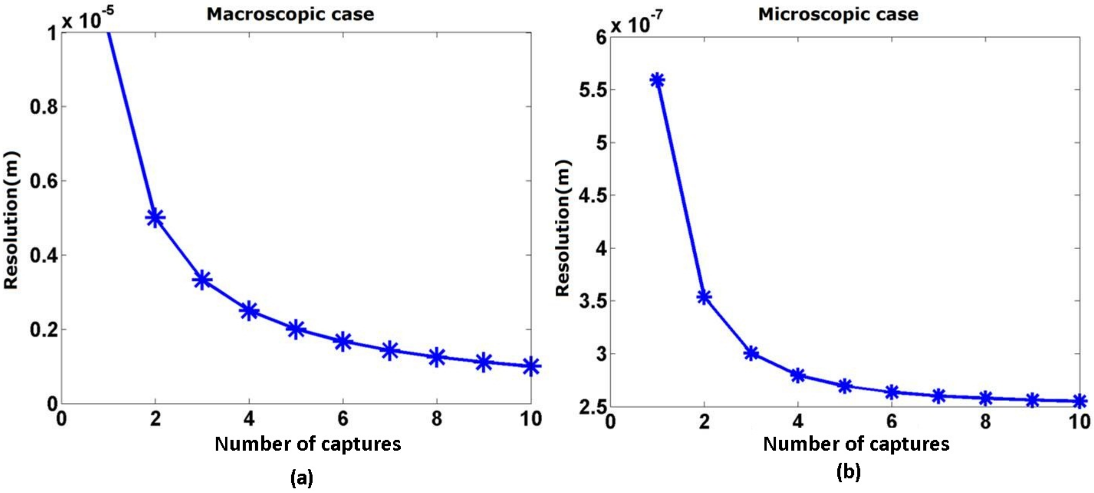

Figure 7.1: Improvement in resolution over 10 contiguous captures (in one dimension) for synthetic aperture digital holography. (a) the macroscopic case and (b) the microscopic case

as the human eye is positioned at a reasonable distance from the SLM, the aperture of the eye will itself be the limiting aperture in the system and it will limit the resolution. We now discuss the resolution and the size of the image on the retina of the observer at a particular distance. We also discuss the range of angular perspective available to the viewer. Really, it is the increased range of angular perspective from a synthetic aperture digital hologram that will benefit the viewer's experience in DH microscopy and not the reduced resolution. In Fig. 7.2 below we illustrate the improvement in range of perspective offered by a SADH. The most well-known property of holograms is that of 3D perspective. A 3D perspective of an object can be seen commonly in reflection holograms. A similar effect can also be seen in a digital hologram of a 3D object displayed on an SLM. Various regions in the hologram plane have recorded light coming from a different angle. So when a small aperture of the wave field propagating from the hologram is reconstructed, the object is seen from that position. This windowed part of the hologram may be reconstructed optically by the eye or numerically by selecting the segment and then carrying out a numerical reconstruction as discussed in Chapter 3. To simplify the following analysis we assume that the SLM that displays the hologram has similar properties to the CCD that recorded it, i.e. they have the same aperture D_x and D_y and the same pixel pitch. The effect of SLM/CCD mismatch

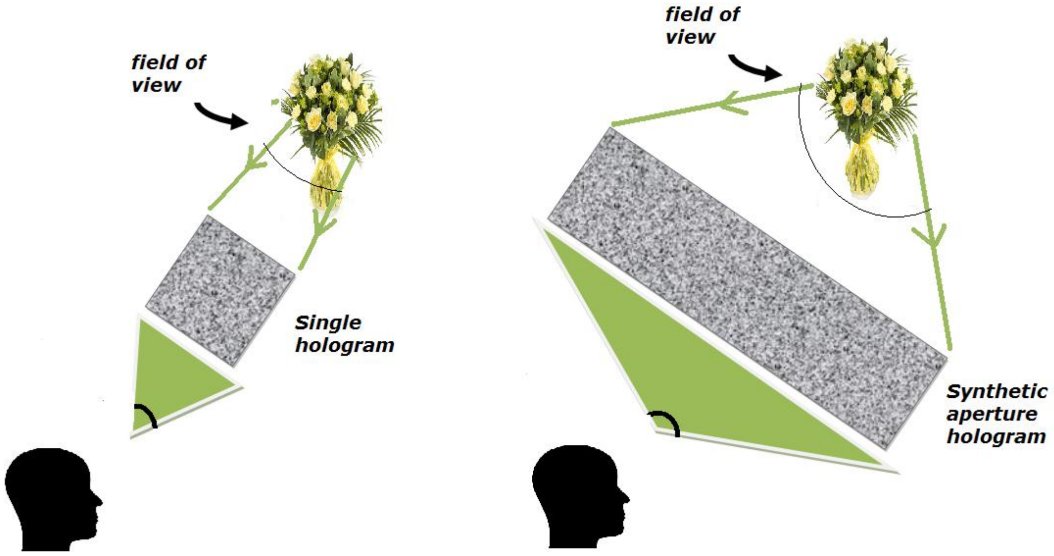

Figure 7.2: Perspectives and enhanced field of view from a synthetic aperture Hologram where the viewer sees the virtual image.

is not considered here. The range of angles that the viewer can perceive is related to θ_n which is the half-angle of the maximum cone of light that can enter the camera and exit the SLM from a point on the object centred on the optical axis (n can be x or y). See Fig. 7.3 (a) for an illustration of this concept. We determine that the maximum range of angles of a 3D point on the optical axis that an observer can see from an SLM is given by

$$2\theta_n = 2\tan^{-1}\left(\frac{D}{2z}\right) \tag{7.1}$$

where z is the distance of the observer from the SLM and D is the dimension of the SLM. We can have a different range of perspectives in the two dimensions if D_x and D_y are different. From this equation we can calculate the theoretical expansion in angular perspective from a synthetic aperture digital hologram. In Fig. 7.4 (b) we show the range of angles that are given from a synthetic aperture that is created from some number of contiguous captures. This plot corresponds to the case when the camera aperture, $D_x = 1$cm, the distance from camera to object is z $=$ 20cm and the source wavelength $\lambda = 500$nm. These values are similar to the values that we will have for the physical parameters in the 'Real3D' project. The figure shows an approximate linear improvement in angular perspective through 10 contiguous captures.

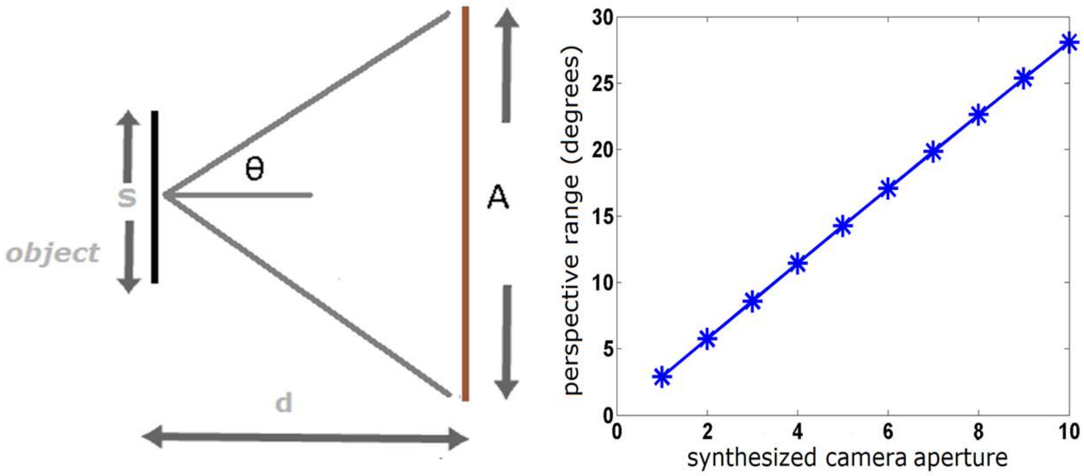

Figure 7.3: Increase in angular perspectives. (a) Illustration of the range of angles subtended from an object point on the optical axis to the camera aperture. (b) The expansion of angular perspective using synthetic aperture for a 1cm camera aperture where 10 contiguous camera apertures are recorded.

7.4 Synthetic aperture by rotating the object wavefield

In this technique, a mirror is used to direct the object wavefield to the camera. This mirror is then rotated so that different parts of the object wavefield are incident on the camera. The rotation of the mirror then introduces a translational and a linear phase shift in between the different captured parts. These different parts are then appropriately shifted in space and spatial frequency and joined together to generate a synthetic aperture image. Consider that the complex wavefield incident on the camera in the first instance is represented by

$$H_1 = O(x, y) \exp i\phi(x, y) \tag{7.2}$$

The wavefield incident after the rotation of the mirror can be represented by

$$H_2 = O(x - d, y) \exp[i(\phi(x - d, y) - \alpha x)] \tag{7.3}$$

The following steps are taken to join the two holograms together:

1. The quantity, d is the translational shift and the quantity α is the linear phase shift introduced by rotation of the mirror. By correlating $|H_1|$ and $|H_2|$, the translational shift, d is found out.

2. Next, the parts of the two holograms which have the same amplitude are extracted. These two parts have a linear phase shift $\exp(i\alpha x)$ between them.
3. A linear phase shift in the space domain corresponds to a translational shift in the spatial frequency domain. This linear phase shift can be easily be found by correlating the Fourier transform of the two common parts.
4. After the phase shift factor, α is determined, the hologram H_2 is multiplied by a phase factor $\exp i\alpha x$ to give $o(x-d,y)\exp[i(\phi(x-d,y))]$.
5. The two hologram matrices are then appended to each other in the x direction to yield the larger digital hologram.
6. The same process is repeated for subsequent angles of rotation and multiple holograms are stitched together.

This methodology used is further illustrated shown in Fig. 7.4. By using correlations, we can accurately determine these shifts and this accuracy can be further increased by sub-pixel correlation where the holograms are interpolated before correlation. We implement the above mentioned method in our experimental setup and use a beam splitter to rotate the object wavefield. We use cam0 in this study (see Table A.1). Fig. 7.5 shows the amplitude of the complex hologram captured from one position of the beam splitter using phase shifting. We rotate the beam splitter in steps of approximately 0.37 degrees and capture 6 complex holograms. These holograms are then stitched together to yield the wide aperture hologram shown in Fig. 7.6. Fig. 7.7 shows the reconstruction obtained from the original hologram and Fig. 7.8 shows the reconstruction obtained from the synthetic aperture digital hologram.

As it can be seen, the same object is now represented by a larger number of pixels. The increase in aperture can be quantified by measuring the depth of focus of the reconstruction of the hologram. When the aperture of an imaging system increases, the depth of focus decreases [70]. This can be analyzed by reconstructing the hologram and calculating a focus metric such as variance. A region in the object plane is selected and the variance of the pixel values in that region is plotted with distance from the camera. In Fig. 7.9, we see the depth of focus for the reconstruction of the two holograms. These curves shows how quickly the focus is falling off and the width of this variance curve is directly related to the depth of focus of the holographic imaging system. The

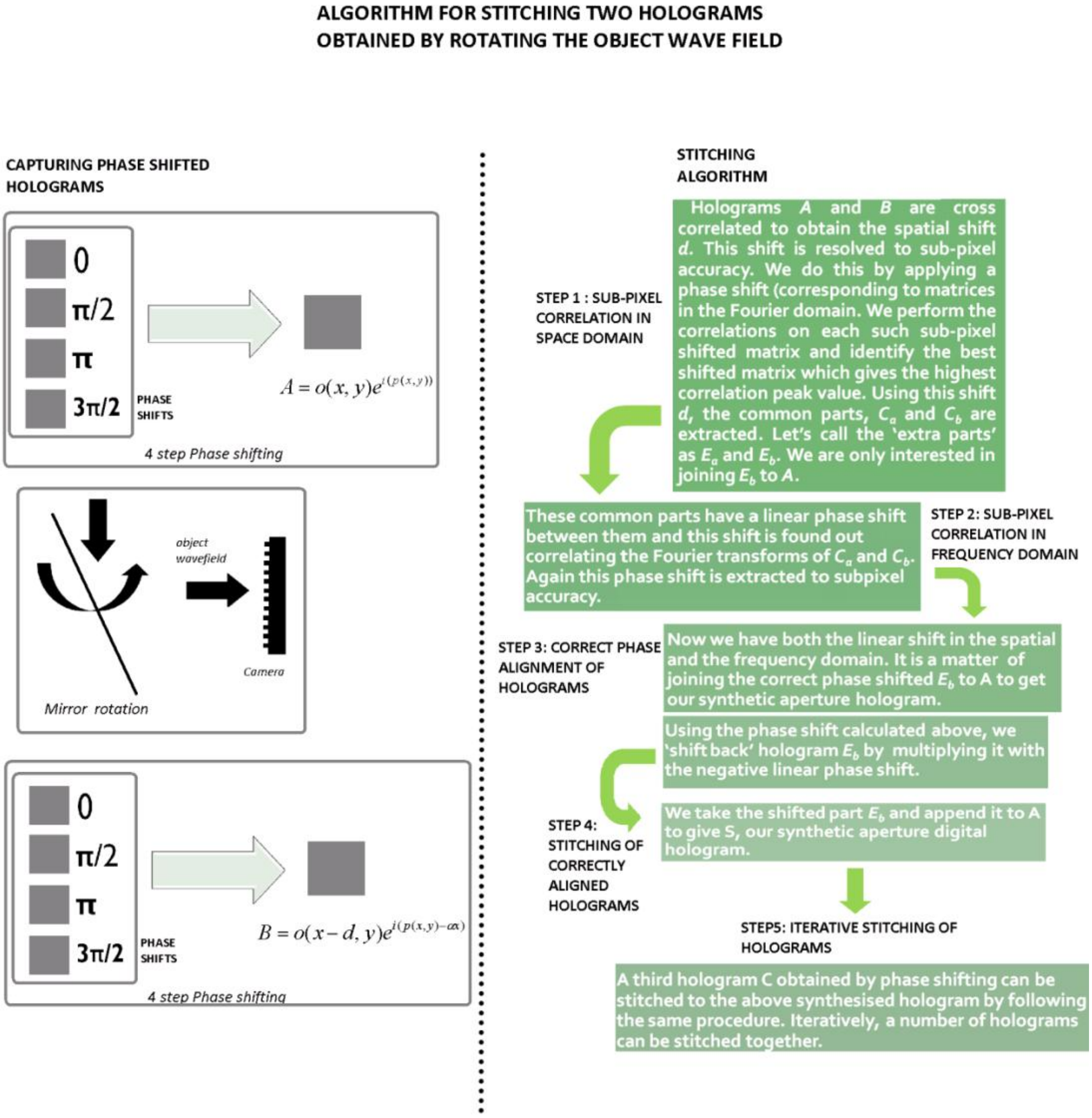

STEP 1 : SUB-PIXEL CORRELATION IN SPACE DOMAIN

Holograms A and B are cross correlated to obtain the spatial shift d. This shift is resolved to sub-pixel accuracy. We do this by applying a phase shift (corresponding to matrices in the Fourier domain. We perform the correlations on each such sub-pixel shifted matrix and identify the best shifted matrix which gives the highest correlation peak value. Using this shift d, the common parts, C_a and C_b are extracted. Let's call the 'extra parts' as E_a and E_b. We are only interested in joining E_b to A.

STEP 2: SUB-PIXEL CORRELATION IN FREQUENCY DOMAIN

These common parts have a linear phase shift between them and this shift is found out correlating the Fourier transforms of C_a and C_b. Again this phase shift is extracted to subpixel accuracy.

STEP 3: CORRECT PHASE ALIGNMENT OF HOLOGRAMS

Now we have both the linear shift in the spatial and the frequency domain. It is a matter of joining the correct phase shifted E_b to A to get our synthetic aperture hologram.

Using the phase shift calculated above, we 'shift back' hologram E_b by multiplying it with the negative linear phase shift.

STEP 4: STITCHING OF CORRECTLY ALIGNED HOLOGRAMS

We take the shifted part E_b and append it to A to give S, our synthetic aperture digital hologram.

STEP5: ITERATIVE STITCHING OF HOLOGRAMS

A third hologram C obtained by phase shifting can be stitched to the above synthesised hologram by following the same procedure. Iteratively, a number of holograms can be stitched together.

Figure 7.4: Methodology for synthetic aperture stitching in the wavefield rotation method

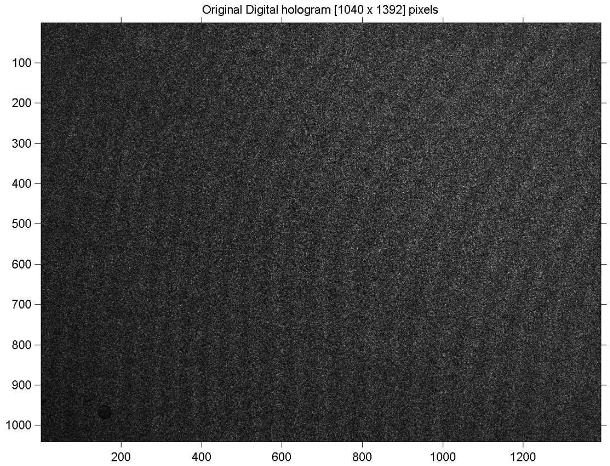

Figure 7.5: Hologram captured from one position of the beam splitter.

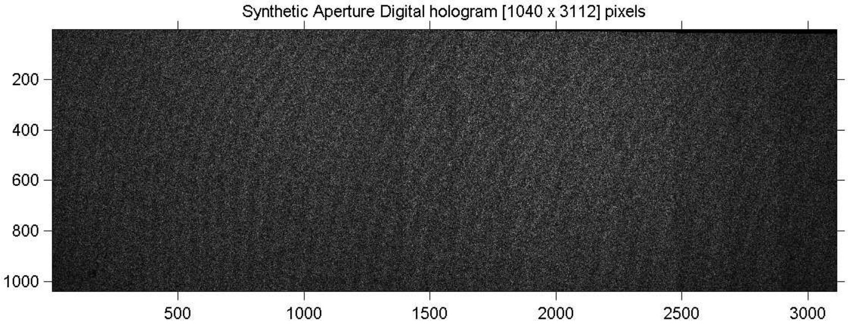

Figure 7.6: Hologram synthesized from five rotations of the beam splitter.

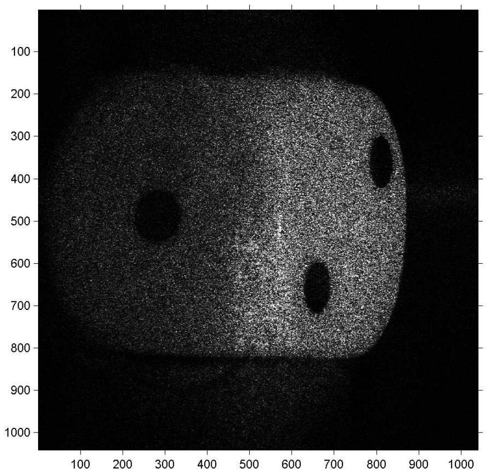

Figure 7.7: Reconstruction of original hologram.

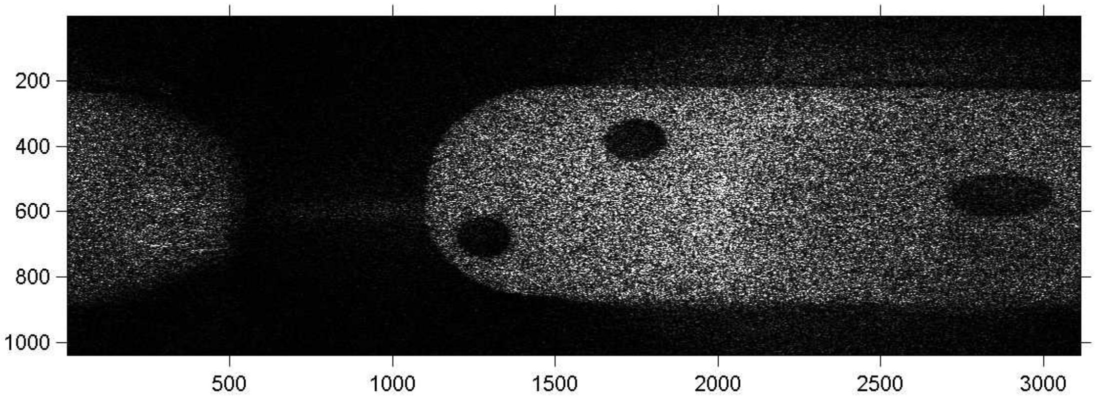

Figure 7.8: Reconstruction of Synthetic aperture hologram.

figure above shows the variance curve normalized to 1. The original hologram is padded with zeros to bring it to the same size as that of the synthetic aperture hologram. As it can be seen, the variance curve for the synthetic aperture hologram is more steep and slightly thinner than the original hologram.

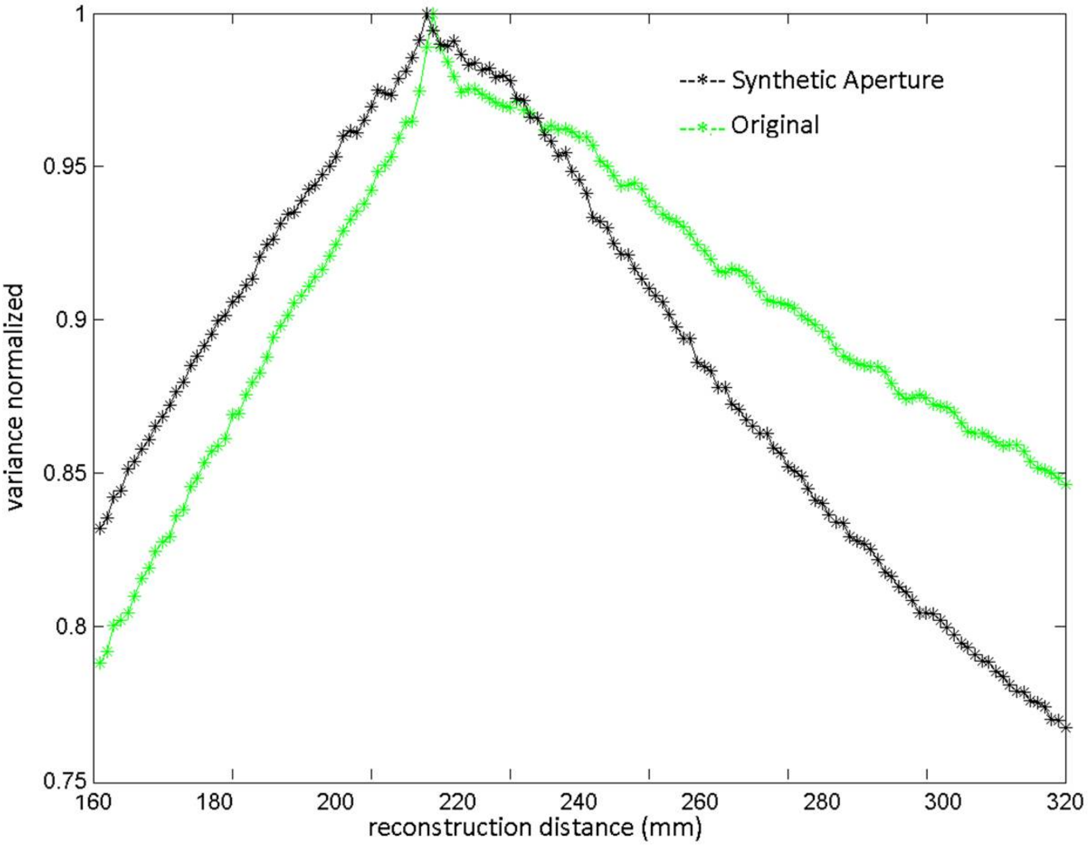

Figure 7.9: Reduction in depth of focus as the aperture is increased synthetically for method 1

7.5 Synthetic aperture by translating the camera

In this method, we modify and enhance the technique used by Massig [141], in which a camera is translated across a plane and multiple holograms are joined. In contrast to the original technique in which off-axis Fourier technique was used, we use inline-Fresnel architecture with a plane reference beam. We also use phase-shifting to retrieve complex wave fields and join them together. We again demonstrate an increase in aperture by plotting the decrease in the depth of focus. The methodology followed is shown below. Since we use a translation stage which moves accurately in one direction, we ignore any phase factors induced due to rotations.

Consider that the complex wavefield incident on the camera in the first instance is represented by

$$H_1 = o(x, y) \exp i\phi(x, y) \tag{7.4}$$

The wavefield incident after the translation of the camera can be represented by

$$H_2 = o(x - d, y) \exp i[\phi(x - d, y)] \tag{7.5}$$

The following steps are taken to join the two holograms together:

1. The quantity, d is the translational shift introduced by translation of the camera. By correlating $|H_1|$ and $|H_2|$, the translational shift, d is found out.

2. The two hologram matrices are then appended to each other in the x direction to yield the larger digital hologram.

3. The same process is repeated for subsequent holograms and they are stitched together.

The schematic for this setup is shown in Fig. 7.10. The object used in this case is a transmissive sample(USAF resolution chart) and is placed at a distance of approximately 102mm from the camera. The experimental setup used is shown in Fig. 7.11. Fig. 7.12 shows the hologram obtained from one position of the camera. The camera is translated by an amount less than the width of the sensor so that consecutive captures have an overlapping area in them. Fig. 7.13 shows the hologram stitched after five translations of the camera.

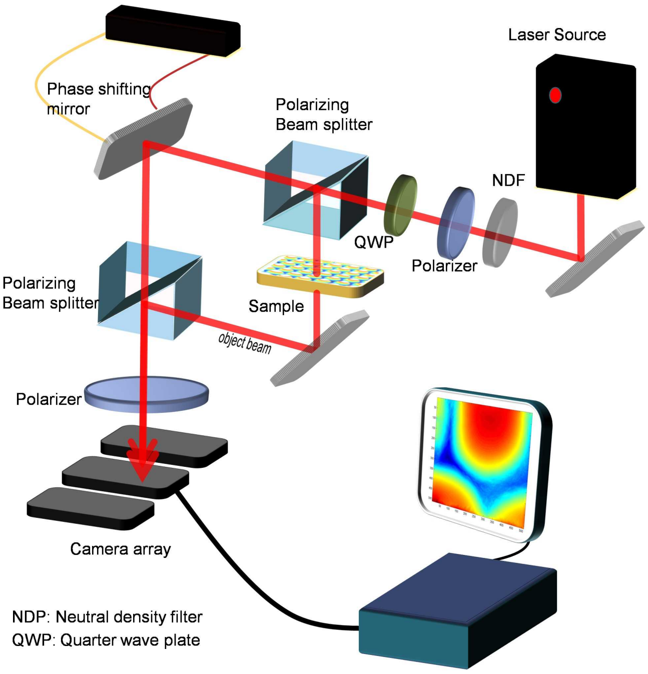

Figure 7.10: Schematic for synthetic aperture using phase shifting and camera translation.

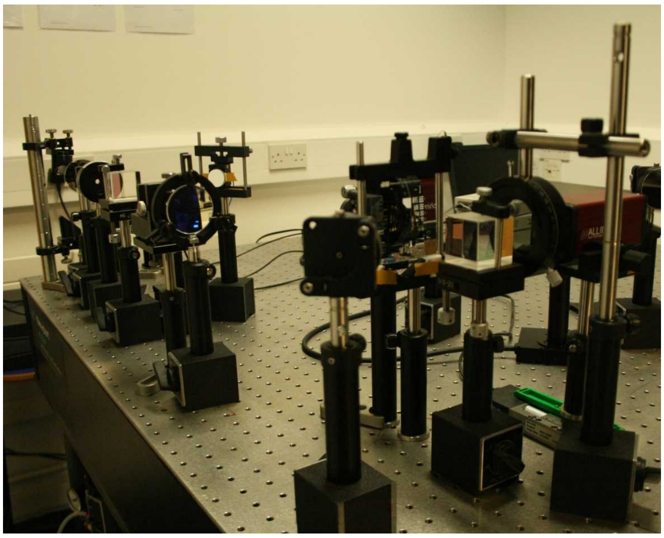

Figure 7.11: Experimental setup for synthetic aperture using phase shifting and camera translation.

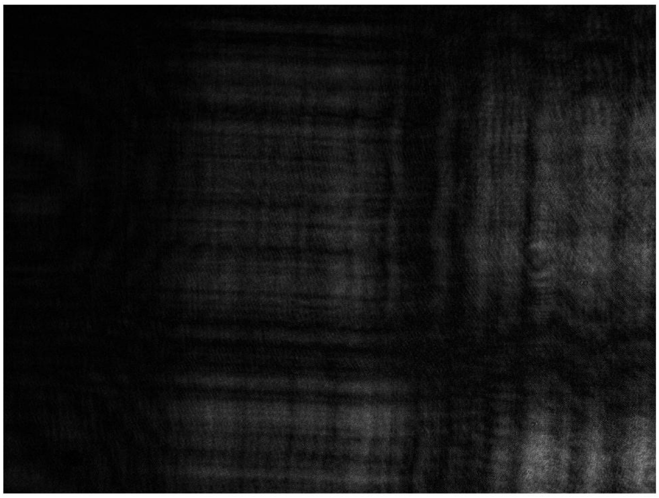

Figure 7.12: Hologram captured from one position of the camera.

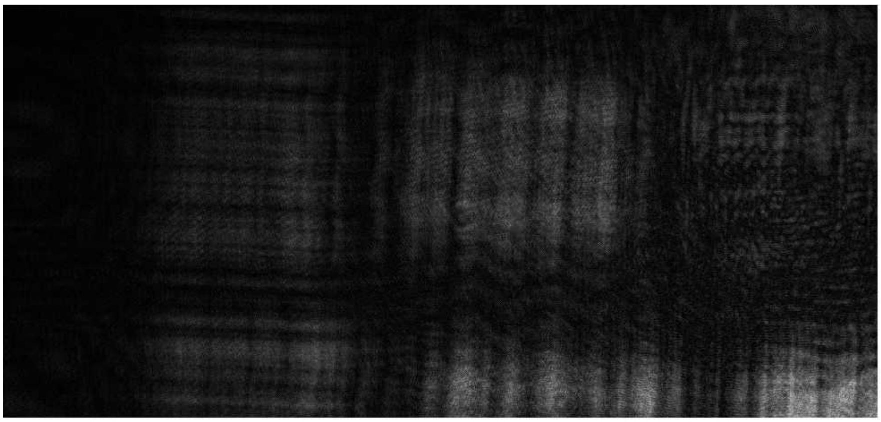

Figure 7.13: Hologram stitched together after camera translation.

Figure 7.14: Reconstruction from Hologram captured from one position of the camera.

Fig 7.14 shows the reconstructions from the hologram captured the original hologram and Fig 7.15 shows the reconstruction from the synthetic aperture hologram. We see more of the object in the reconstructions of the synthetic aperture.

Figure 7.15: Reconstruction from Synthetic aperture hologram.

We plot a focus metric, the variance of a section of the hologram for different reconstruction distances. Fig. 7.16 shows the variance curve normalized to 1. Again, the original hologram is padded with zeros to bring it to the same size as that of the synthetic aperture hologram. The depth of focus curve for the synthetic aperture hologram is steeper than the original hologram indicating the effectiveness of stitching.

7.6 Conclusion

In this chapter, we have discussed two methods to implement synthetic aperture digital holography. We have also shown the impact of synthetic aperture on the resolution and range of perspectives. The decrease in the depth of focus as a result of increase in the aperture was also shown. We believe that synthetic aperture techniques may be needed for the practical implementation of digital holography in a 3D display system.

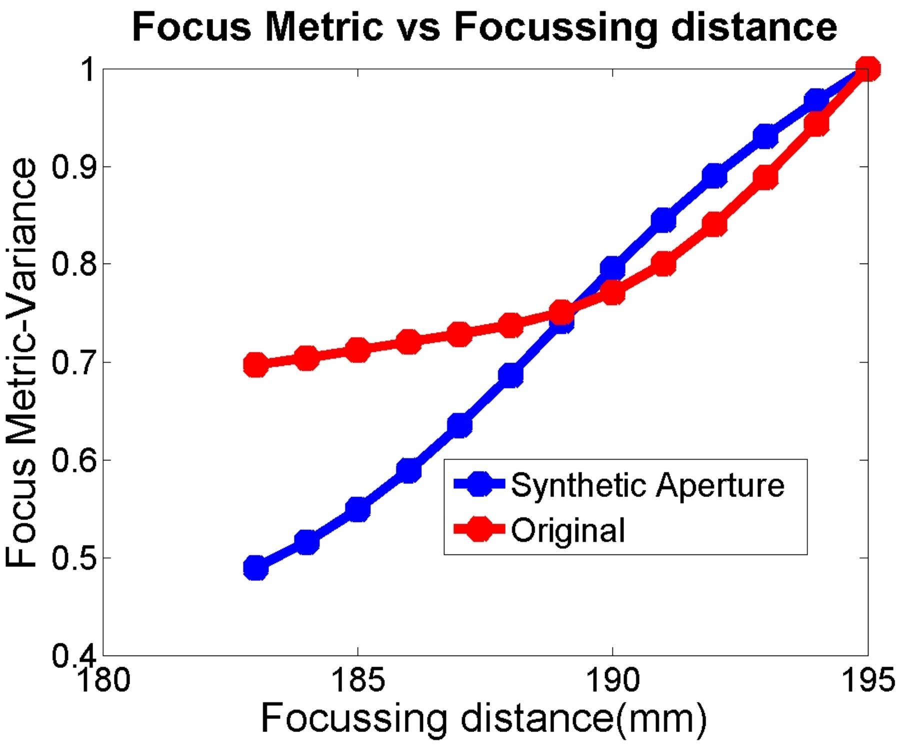

Figure 7.16: Reduction in depth of focus as the aperture is increased synthetically.

8

Conclusion

The aim of this chapter is to provide a conclusion to this thesis and summarize the main contributions of this work. In practice, the work done in this thesis contributes to the general area of digital holography especially in its application for 3D display.

The contributions of this thesis can be broadly divided into three areas.

- **Applications where a faster reconstruction of digital holograms is required :** In chapter 3, we introduced the basics of imaging objects using digital holography. We began by introducing the idea of recording and reconstructing holograms on a digital sensor. We discussed the algorithms for reconstruction of digital holograms. We also introduced the various features of digital holography like the twin image, ability to refocus the image to different depths, ability to reconstruct from partial holographic data and the issue of speckle noise. In Chapter 4 and 5, our focus was on techniques to improve some aspects of digital reconstruction algorithm in digital holography. We discussed methods to speed up the execution time and reduce the memory usage of the reconstruction algorithms used in digital holography. We showed that with the ideas of pre-computation and compression of the chirp matrices [2] and fixed point implementations [1], the reconstruction algorithm can be implemented computationally efficiently. We believe these results to be highly useful in applications requiring speed up of reconstruction of digital holograms.These can include implementations of digital holography on portable devices and microscope-on-a-chip applications. In such cases, it is necessary to reconstruct digital holograms but in a memory efficient and energy efficient manner. Another important application more relevant for the

Real3D project is in the processing of captured digital holograms prior to them being replayed on a display unit. For example, in-line digital holograms can be captured at a fast frame rate but they suffer from the overlapping twin image. The overlapping twin image can be removed by an image segmentation based approach and it requires a few reconstructions of the hologram. The speed-up technique showed here can be useful in such a case to fasten the intermediate processing. In a related work in Chapter 6, we have also shown how the image quality can be improved by speckle averaging but keeping the total number of bits transmitted the same. This method will be useful in an internet based digital holographic display system.

- **Modeling of noise in digital holographic imaging systems :** A major part of this thesis was the development of a noise model for additive noise in digital holography. The influence of quantization noise on the complex reconstructed image was theoretically and experimentally studied. The same study was extended to study the influence of shot noise [4]. We showed that in digital holography, quantization error is introduced as uniformly distributed additive noise in the recording plane (camera plane) and this manifests itself as a complex noise in the reconstruction plane with gaussian distributed real and imaginary parts, rayleigh distributed amplitude and uniformly distributed phase. We also characterized the various statistical properties of this noise both theoretically and experimentally in the case of lensless off-axis Fourier digital holography. We have studied the influence on the phase measurement accuracy and the reconstructed intensity quantitatively. The standard deviation in the phase measurement error increases by a factor of 2 for every bit removed in the quantization process. We also characterized the noise in the intensity of the reconstructed images. This complex noise can be treated as the result of a random walk in the complex plane and shares the same statistical properties as that of speckle. We quantified the influence of the additive noise on the phase measurement error in the hologram plane in digital holographic microscopy under the assumption that the object is highly transmissive in nature. We showed that in general, the noise in the output plane of a digital holographic system has Gaussian characteristics irrespective of the distribution in the capturing plane. This happens due to both the Fourier filtering as well as the numerical propagation of the complex wavefield. We described the relationship between standard deviation in the error in the camera plane to the standard deviation in the error in the reconstructed phase in the case of Fresnel off-axis geometry. Shot noise which has Poisson statistics is a fundamental noise source for holographic imaging. According to our simple model, the phase error can be decreased linearly by amplifying the image by either increasing the exposure time or by adding multiple exposures as shown in the experiments by the authors in [127]. The reduction in error happens because the amplitude of the reconstructed image increases relative to the perturbation by the noise phasors in a $\sqrt{\alpha}$ fashion where α is the amplification of the holographic signal. Though we have studied the noise due to quantization and shot noise, we believe that the same method can be applied to other kinds of additive noise in the hologram plane for other architectures in digital holography.

The quantization aspect of the digital sensor also plays a role in the quality of the reconstructed image. The work done on the effect of quantization noise on both the amplitude and phase of the reconstructed image can be useful in modeling of such imaging systems and in optimization of the capture rate and image quality.

- **Improvement in image quality via twin image reduction and synthetic aperture :** In chapter 6, we presented some methods to improve the reconstruction quality of digital holograms in presence of noise. We presented methods to improve the reconstruction quality. We showed that the noise due to quantization can be reduced using standard speckle reduction techniques in addition to lowering the memory usage. Such speckle reduction techniques can find use especially in the area of real time 3D display of digital holograms. We also proposed a novel method to remove the twin image from inline-Fresnel holograms. This method does not require expensive phase shifting devices and it preserves the camera bandwidth and is clearly useful for recording good quality holograms. For 3D digital holography based displays, it is important to capture a larger range of angular perspectives. We implemented a novel approach (in chapter 7) for synthetic aperture digital holography for this purpose. We combined phase shifting and spatial translation of the camera to stitch the complex phase fields. We believe this method to be especially useful for applications in 3D display where the range of perspectives in the reconstructed 3D image can be enhanced.

The work done in this thesis primarily contributed to work packages of Scenario 1 of the FP7 research project, REAL3D. Apart from these primary contributions, contributions were also made in the form of assisting in experiments, creating figures for various papers, writing computer programs and discussions during group meetings. In total, 6 peer-reviewed journal papers (3 being primary author)[1, 3, 4, 57, 58, 59] have been published and 6 conference proceedings (3 being primary author)[2, 60, 61] have been published. Additionally, 2 talks have been given at international conferences.

Appendix A

Experimental recording of digital holograms

During the course of this thesis numerous optical systems were constructed for the recording of digital holograms of static objects. In Fig. A.1 and Fig. A.2, we show two common set ups that we used. In Fig. A.1 the laser source outputs a beam directly to a periscope in order to change the height of the beam. It then passes through a neutral density filter which allows us to vary the input power to the system as required. A linear polarizer and a neutral density filter follow next. By varying these two elements we can control the relative power that is output from the two arms of the polarizing beam splitter which is the next element to be encountered. The horizontal arm of the beam splitter travels through a microscope objective that converges the light. The light passes through a pinhole with a 10μm diameter which spatially filters the light and it then passes through a lens which collimates the light and creates a plane wave reference beam which propagates directly toward the camera. The second arm of the beam splitter is reflected from a mirror attached to a piezoelectric motor which can be moved by fractions of a wavelength for phase shifting digital holography.

In Fig. A.2, we show a second set up that was used to record holograms. There are a number of key differences between this set up and the one just described. Firstly the camera position has been moved. To ensure that object and reference wavefields travel approximately equidistant paths, thereby maximizing the temporal coherence of the system. The reference wavefield reflects from a mirror towards the camera face. Secondly the object beam from the first beam splitter is passed through a quarter wave plate and then another polarizing beam splitter. The combination of these elements allows us to create two object beams so that we can illuminate the objects from two directions to ensure that we avoid shadows. Both beams are directed towards opposite sides of the object via a system of mirrors and they are both passed through diffusers which spread the light out to illuminate the entire object. The light is scattered directly towards the final beam splitter which reflects the light towards the camera. The use of multiple diffuser illumination system in the second system allows for more uniformly distributed illumination on the object with less self-occlusion. We note that the object was often positioned on a rotation stage and the diffusers in the set up were moved using a translation stage. Both the rotation and translation stage were controlled by a common driver. An integrated lab view control system was designed for the entire set up and this is discussed in more detail in Appendix B. The laser was supplied by CrystalLaser with a wavelength of 785nm. It is a solid state laser with a coherence length of approximately 30cm and it is linearly polarized. The various cameras used in the thesis are summarized below.

Camera	Manufacturer	Dimensions	Pixel pitch	Interface
cam1	AVT-Dolphin F-145B	1392x1040	$6.45\mu m$	IEEE 1394 (firewire)
cam2	Basler piA1900-32gm/gc	1928 x 1084	$7.4\mu m$	GigE-ethernet
cam3	Basler piA2400-17gm/gc	2448 x 2050	$3.45\mu m$	GigE-ethernet

Table A.1: Cameras used in experiments

The rotation and translation stage, MFA-PPD (translation stage, resolution 7μm), SR50PP (rotational stage, resolution 0.001°) and the controller, (SMC100PP) are from Newport. The piezoactuator (Model PZ38CAP) from Piezosystem Jena was used to implement phase shifting digital holography. This has an accuracy of 0.1nm and a range of 32μm in closed loop operation.

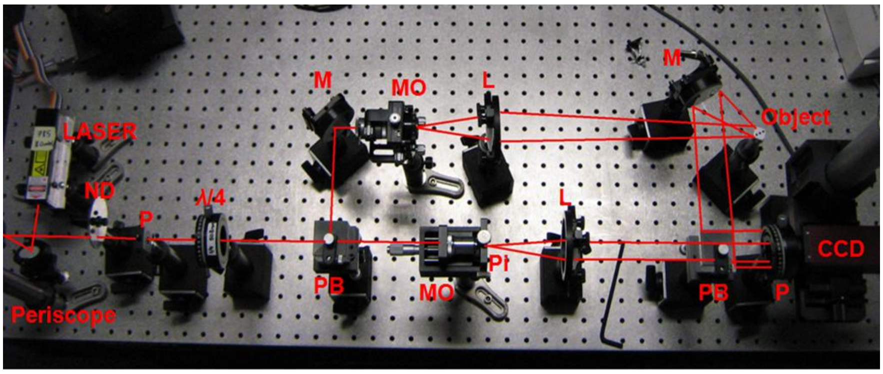

Figure A.1: Experimental setup I First type of holographic recording setup , ND: Neutral Density Filter, P: Polariser, $\lambda/4$: quarter wave plate, MO: Microscope Objective, PB: Polarising Beam splitter, PI: Pinhole, L Lens, M Mirror, PSM Phase Shifting Mirror, D Diffuser, RS rotation Stage, I Iris.

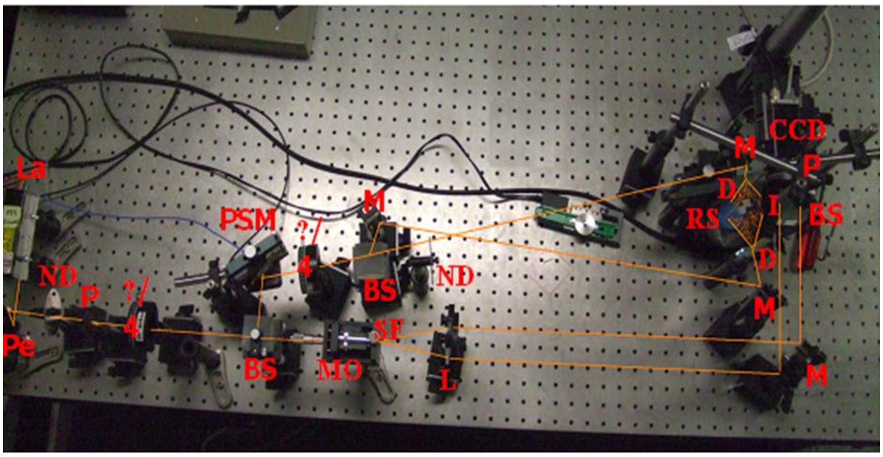

Figure A.2: Experimental setup II Second type of holographic recording setup with object illumination from two sides : ND: Neutral Density Filter, P: Polariser, $\lambda/4$: quarter wave plate, MO: Microscope Objective, PB: Polarising Beam splitter, PI: Pinhole, L Lens, M Mirror, PSM Phase Shifting Mirror, D Diffuser, RS rotation Stage, I Iris.

Appendix B

Calibration for phase shifting using speckled holograms

In a piezoelectric actuator an applied voltage to a piezoelectric material causes a change of the dimensions of the material, thereby generating a motion. These actuators use multilayer ceramics which have a high sensitivity to applied voltage to generate the piezoelectric effect and exhibit qualities like hysteresis and drift. They are sensitive to environmental factors such as temperature. Thus it is important to accurately calibrate the device frequently. This calibration can be done by setting up an interference between near planar waves to get wide fringes on the camera. When a voltage is applied, the fringes 'move' and a region of the bright fringe is selected and the intensity monitored as the voltage changes. This yields the voltage-phase curve for the device. However setting up such interferences regularly is cumbersome and is not a robust design.

Fig. B.1 shows the mirror attached to the piezoactuator device. In a digital holographic imaging setup, it is advantageous to acquire the voltage-phase curve from the speckled hologram of the object present without setting up wide fringes on the camera. It is possible to do this by selecting all the pixels from a narrow band of intensities (e.g all the pixels between 0.7 and 0.8 times the maximum valued pixel) (Fig. B.2)and summing their values for each voltage change. Such a band typically consists of a few thousand pixels. Each band has a different noise distribution. By choosing different such bands different independent signals can be obtained and the voltage-phase curve can be obtained (Fig. B.3).

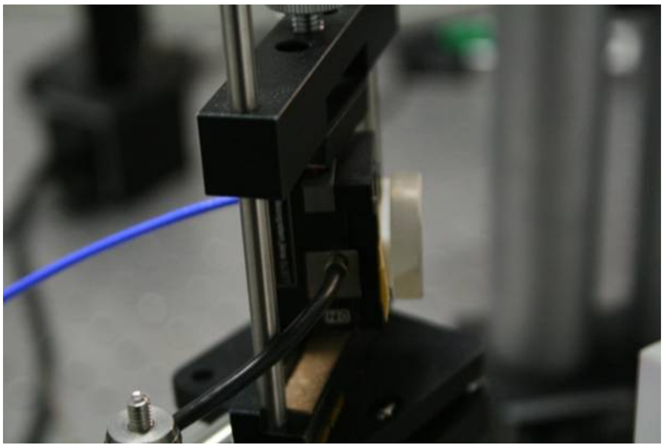

Figure B.1: The mirror attached to the piezoactuator.

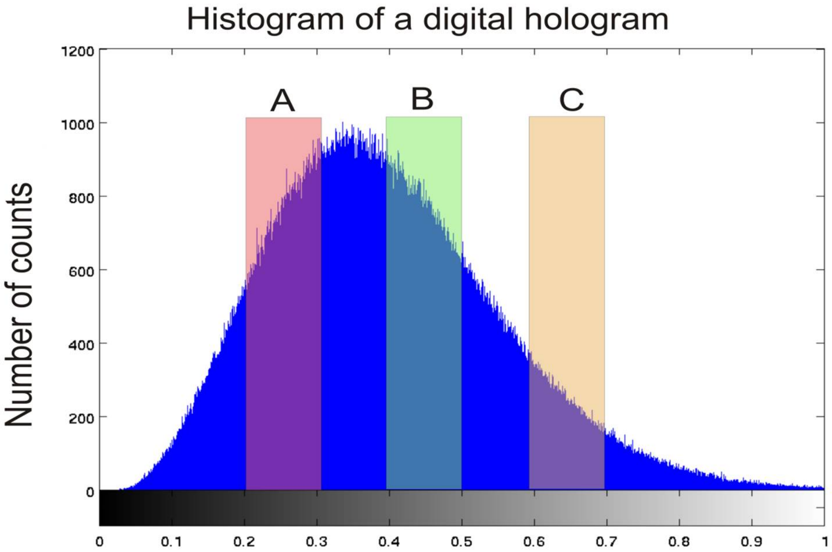

Figure B.2: Histogram of the hologram showing the selected bands of intensities.

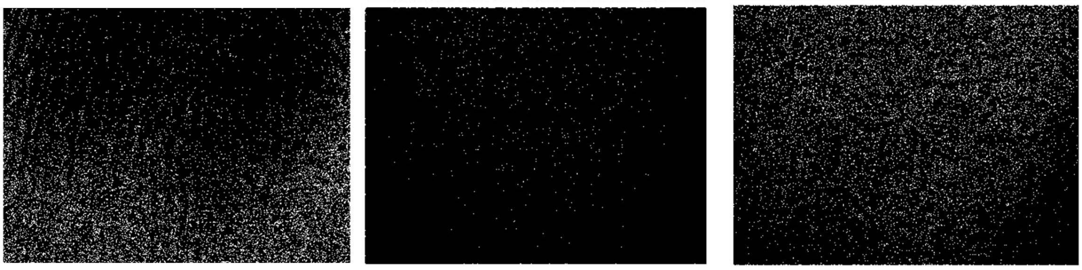

Pixels from Band A

Pixels from Band B

Pixels from Band C

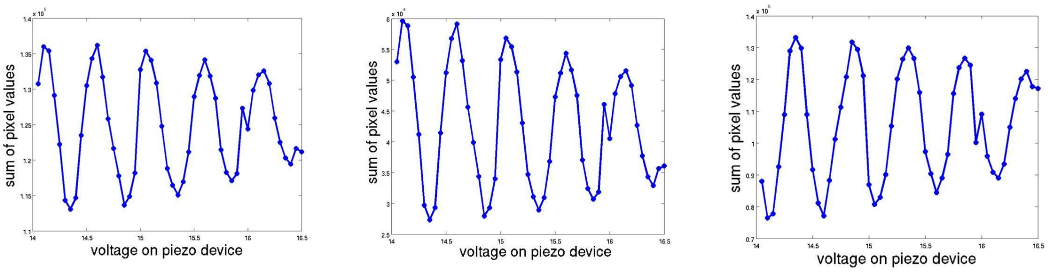

Figure B.3: Calibration curves obtained from different bands.

Appendix C

Computer Interface

We have built a robust program in LabView which can be used with any camera. The phase shifting device and the translation and rotation stages are connected with serial ports and are also integrated into the program. This system is capable of recording high quality digital holograms of a real world 3D object. The object can be rotated on a rotational stage and a full 360° range of perspectives can be recorded. Speckle reduction using moving diffusers can be performed to improve the image quality of the reconstructed images. A LabView based user friendly interface has been developed as shown in Fig. C.1. The main program consists of a number of smaller sub-programs. Here we show the front interface of the LabView program to record a full 360 degree range of perspectives of a 3D object. Since digital holograms are susceptible to vibrations, we do the same range 4 times and take the best quality hologram for each angle.

Our phase shifting program captures 4 interferograms and stores them on a hard disk (Fig. C.2). These files can be sent to our partner universities or can be analyzed by programs such as Matlab. We have also implemented a real time digital hologram recording unit (Fig. C.3) . This uses inline or offaxis architecture for real time capture and replay of holograms. This helps in aligning the system or for initial preview of the objects reconstruction. The hologram and the reconstructed image can be seen on the same screen.

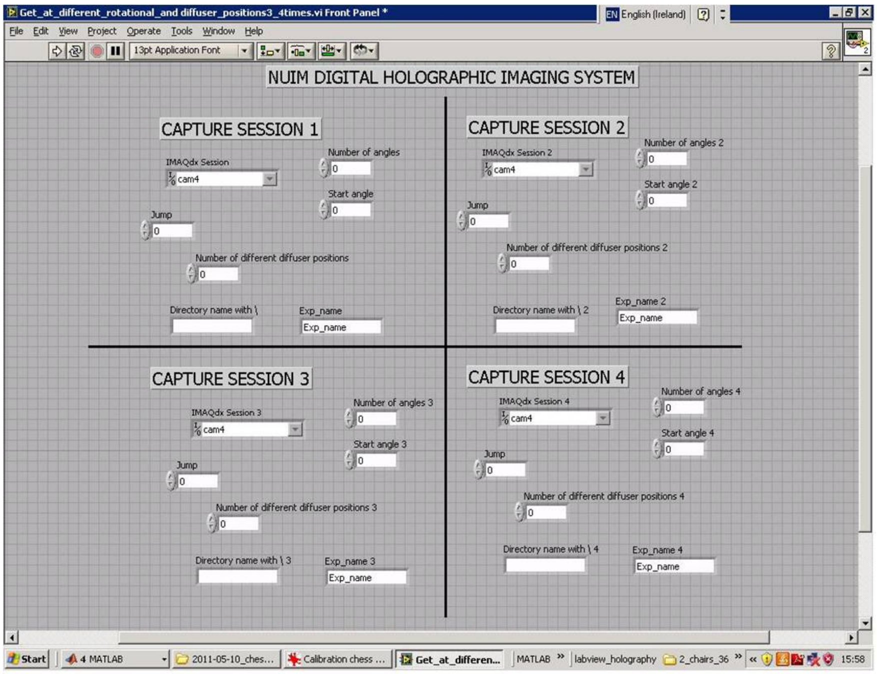

Get_at_different_rotational_and diffuser_positions3_4times.vi Front Panel *

NUIM DIGITAL HOLOGRAPHIC IMAGING SYSTEM

CAPTURE SESSION 1

IMAQdx Session: cam4
Number of angles: 0
Start angle: 0
Jump: 0
Number of different diffuser positions: 0
Directory name with \
Exp_name: Exp_name

CAPTURE SESSION 2

IMAQdx Session 2: cam4
Number of angles 2: 0
Start angle 2: 0
Jump: 0
Number of different diffuser positions 2: 0
Directory name with \ 2
Exp_name 2: Exp_name

CAPTURE SESSION 3

IMAQdx Session 3: cam4
Number of angles 3: 0
Start angle 3: 0
Jump: 0
Number of different diffuser positions 3: 0
Directory name with \ 3
Exp_name 3: Exp_name

CAPTURE SESSION 4

IMAQdx Session 4: cam4
Number of angles 4: 0
Start angle 4: 0
Jump: 0
Number of different diffuser positions 4: 0
Directory name with \ 4
Exp_name 4: Exp_name

Figure C.1: Computer interface for recording 360 degree range of perspectives.

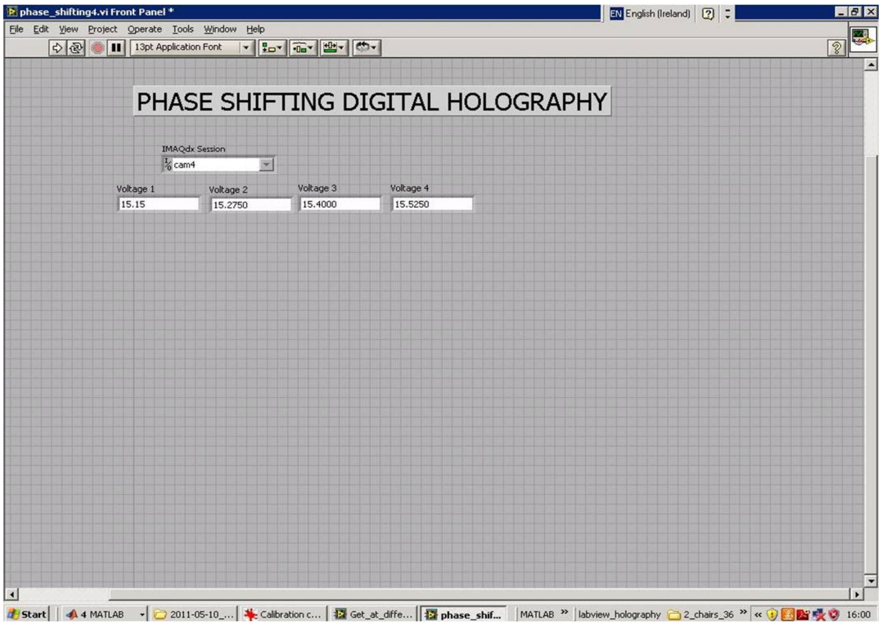

phase_shifting4.vi Front Panel *

PHASE SHIFTING DIGITAL HOLOGRAPHY

IMAQdx Session: cam4
Voltage 1: 15.15
Voltage 2: 15.2750
Voltage 3: 15.4000
Voltage 4: 15.5250

Figure C.2: Program for phase shifting digital holography.

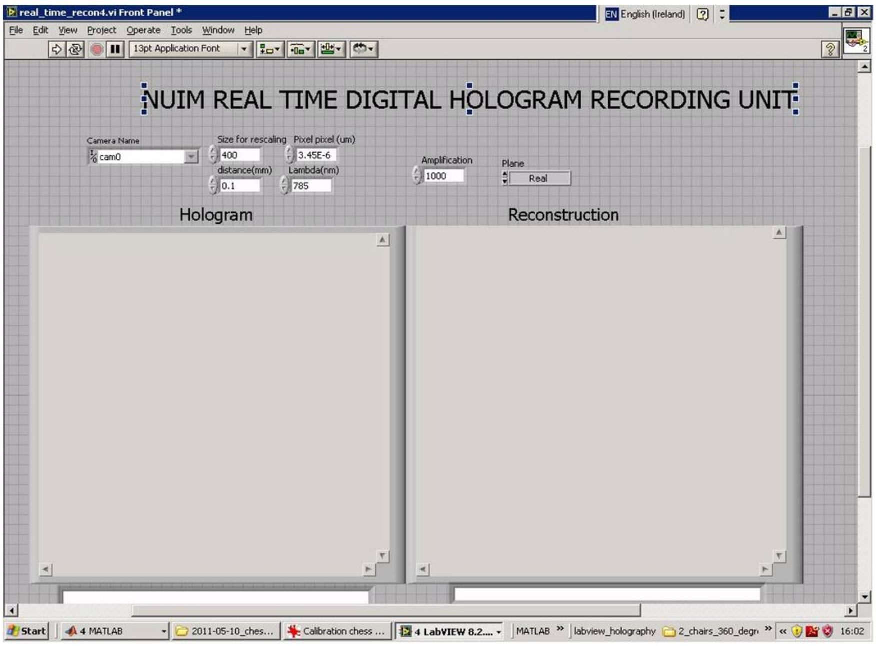

Camera Name: cam0
Size for rescaling: 400
Pixel pixel (um): 3.45E-6
distance(mm): 0.1
Lambda(nm): 785
Amplification: 1000
Plane: Real

Figure C.3: Program for real time digital holography.

Appendix D

Recording of 360 degree scenes of static objects

The experimental system described in Appendix A, together with the software described in Appendix B and C was used to create high quality stop motion videos of a selection of different objects. Many of these objects were printed using 3D printers in NUIM due to the difficulty in finding objects in the desirable size range. The angular jump that we used in recording these videos varied from 1 degree to 4 degrees of rotation and the number of steps taken was given by the number of these angular shifts were required to complete a full circle of 360 degrees.

The higher the number of diffuser positions that we select in the program, the better the speckle reduction that can be achieved. This is assuming that for each object position all of these digital holograms could be displayed in sequence sufficiently quickly to integrate in the aperture time of the human eye. We recorded these holograms with a view to displaying them on SLM as part of the Real3D project. The maximum rate of the SLMs used in the project was 60Hz.The aperture time of the average human eye is approximately 1/30 seconds. Therefore it is possible to integrate approximately three reconstructions over the integration time of the eye. For this reason we record only four PSI digital holograms of different diffuser positions for each object position for all our videos. With this we can achieve approximately 50

In Fig. D.1, Fig. D.2 and Fig. D.3 below we show the numerical reconstruction obtained from videos of PSI digital holograms. For Fig. D.1 we show six reconstructions from angles separated by approximately 60 degrees. Here the reconstructions were calculated numerically using the direct method of simulating Fresnel propagation. The field of view in the figures is identical to the field of view for optical reconstruction using the SLMs. The intensity of the numerical reconstruction is calculated and the four intensities corresponding to the four different diffuser positions are added together in order to simulate what the eye will see when replayed using the SLMs. The two chairs were recorded at a distance of 436 degrees and with an angular step of 1.58 degrees. In total 228 different object positions were recorded of which we show only six here. In Fig. D.2 we show similar reconstructions for the small cube. Here the recording distance is 174.4mm and a step size of 3.93 degrees was taken. In total 92 object positions were recorded. The same parameters were used for the molecule shown in Fig. D.3.

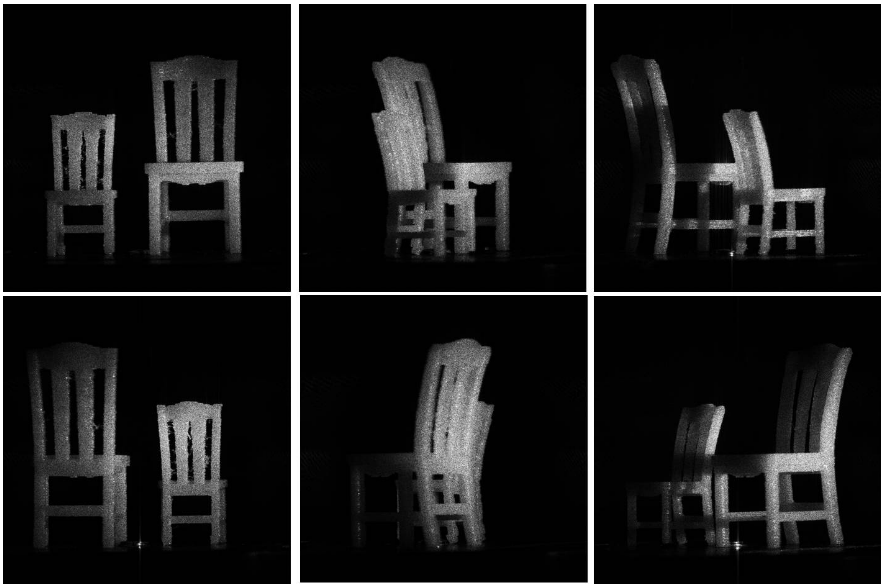

Figure D.1: Numerical reconstructions from NUIMs video I. Rotating set of chairs.

D.1 Recording of holograms of objects under strain - subtraction holography

In addition to the videos of static case digital holograms we also recorded subtraction holograms for display on SLMs. This was achieved by recording PSI digital holograms

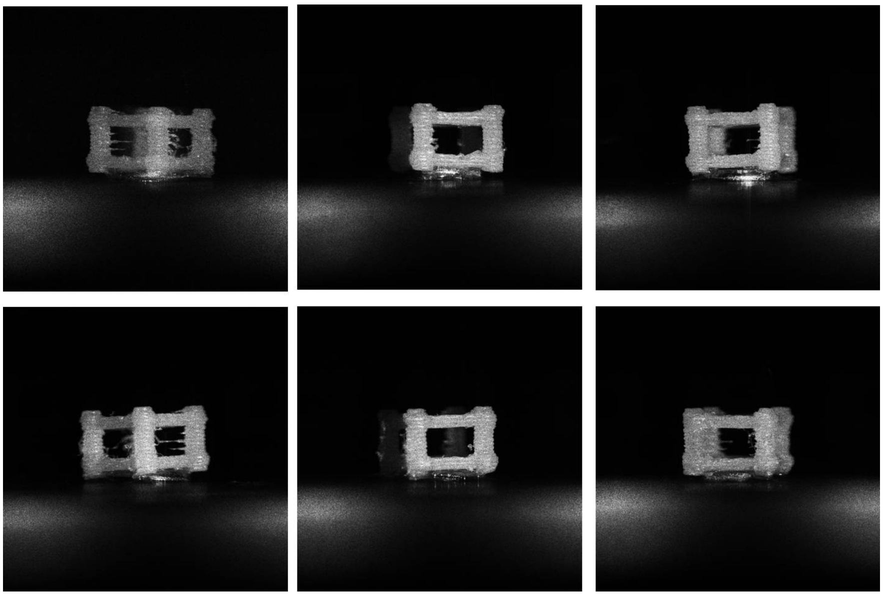

Figure D.2: Numerical reconstructions from NUIMs video II. Rotating cub.

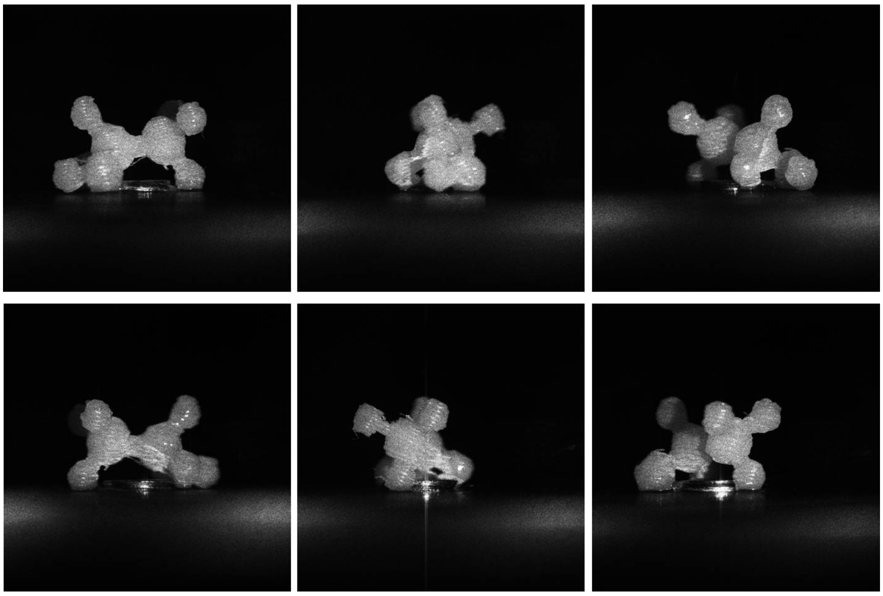

Figure D.3: Numerical reconstructions from NUIMs video III. Rotating molecule.

using the optical recording set up discussed in Appendix A. To record these holograms our objects were mounted in a clamp.

Once the object has been securely mounted a first 'benchmark' PSI digital hologram is recorded using the NUIM Labview program described in Appendix C. The clamp is then tightened manually in order to put a strain on the object. Once the object has come to rest after a few seconds a second PSI digital hologram is recorded and stored. The second complex digital hologram is then subtracted from the benchmark hologram to create a subtraction hologram. This subtraction hologram can be reconstructed numerically or optoelectronically on a SLM by displaying the phase of the subtraction holograms on the SLMs.

The process can be repeated by increasing the strain on the object under investigation and recording another digital hologram which is then subtracted from the benchmark hologram in order to create another subtraction hologram. In creating the subtraction holograms, the reconstructions of which are shown in Fig. D.4 and Fig. D.5, we always used the benchmark hologram in the subtraction process. We note that this is not always necessary and we can create a large number of different subtraction holograms by subtracting any given two holograms rather than always using the first. In Fig. D.4 we show the reconstructions from subtraction holograms of a small metal key under increasing strain by a clamp and in Fig. D.5 we show reconstructions from a small chair figurine under increasing pressure from a manual clamp. The fringes than can be observed in these reconstructions can be directly related to local strain on the object surface, and indeed on the clamp itself. We note that in all cases the numerical reconstructions of the subtraction holograms were obtained by using the direct method of simulating the Fresnel Transform and the intensities were then calculated. No speckle reduction techniques, optical or numerical, were applied to these reconstructions.

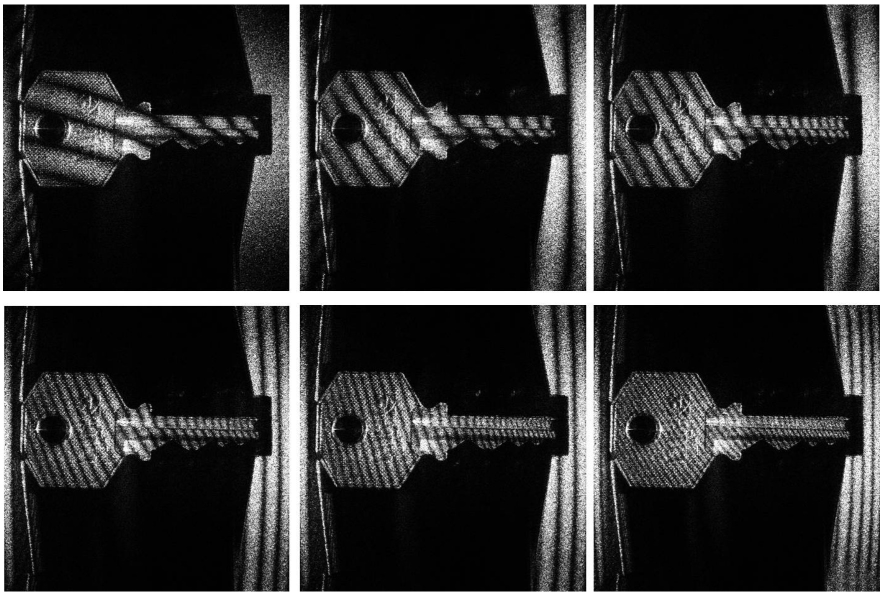

Figure D.4: Subtraction holograms I. Recorded for a key under varying amounts of strain when pressed in a clamp.

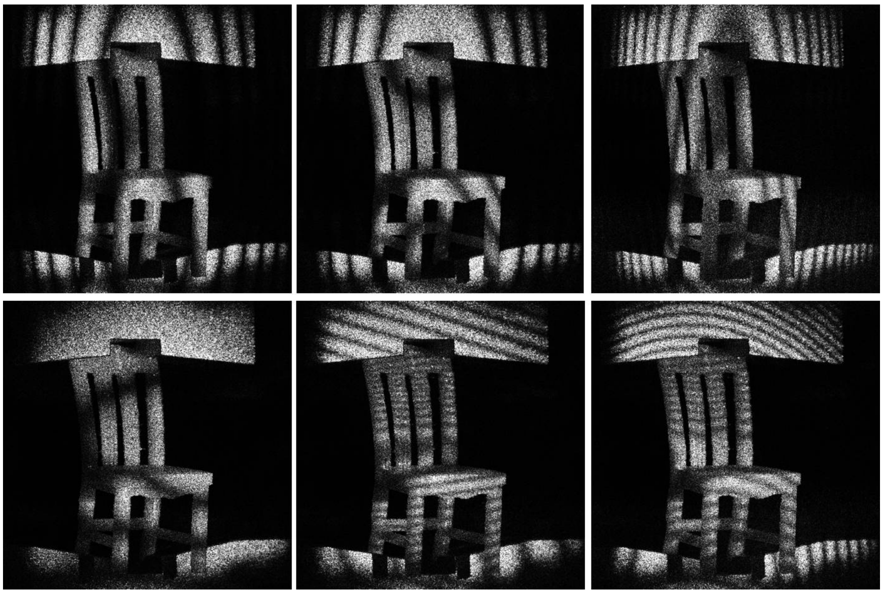

Figure D.5: Subtraction holograms II. Recorded for a plastic chair under varying amounts of strain when pressed in a clamp.

References

[1] N. Pandey and B. Hennelly. **Fixed-point numercial-reconstruction for digital holographic microscopy**. *Opt. Lett.*, **35**(7):1076–1078, 2010. iii, 4, 5, 52, 67, 70, 137, 140

[2] N. Pandey, D.P. Kelly, T.J. Naughton, and B.M. Hennelly. **Speed up of Fresnel transforms for digital holography using pre-computed chirp and GPU processing.** *Proc. SPIE*, **7442**, 2009. iii, 4, 5, 52, 67, 137, 140

[3] N. Pandey and B. Hennelly. **Quantization noise and its reduction in lensless Fourier digital holography**. *Appl. Opt.*, **50**(7):58–70, 2011. iv, 4, 5, 108, 140

[4] N. Pandey and B. Hennelly. **Effect of additive noise on phase measurement in digital holographic microscopy**. *3D Research*, **2**(1), 2010. iv, 4, 5, 138, 140

[5] I.P. Howard and B.J. Rogers. *Seeing in depth, Vol. 2: Depth perception.* University of Toronto Press, 2002. 1

[6] G. Tissandier. *A history and handbook of photography.* Number 1976. Ayer Co Pub, 1878. 1

[7] D.S. Brewster. *The Stereoscope; its History, Theory, and Construction, with its Application to the fine and useful Arts and to Education: With fifty wood Engravings.* John Murray, 1856. 1

[8] P. Surman, K. Hopf, I. Sexton, W.K. Lee, and R. Bates. **Solving the 3D ProblemThe History and Development of Viable Domestic 3DTV Displays**. *Three-Dimensional Television: Capture, Transmission, Display*, page 471, 2007. 1

[9] J.J. McCann. **Color theory and color imaging systems: past, present and future**. *The Journal of imaging science and technology*, **42**(1):70–78, 1998. 1

[10] D.B. Thomas. *The origins of the motion picture.* John Logie Baird Centre, 1973. 1

[11] J. Belloni-Cofler, J. Amblard, J.L. Marignier, and M. Mostafavi. **Photography revealed: the principles of development**. *Endeavour*, **15**(1):2–9, 1991. 1

[12] G. Lippmann. **La photographie des couleurs [deuxième note]**. *CR Hebd. Séances Acad. Sci*, **114**:961–962, 1892. 1

[13] P. Ranson, R. Ouillon, and J.P. Pinan-Lucarré. **A centenary, G. Lippmann, Nobel prize of Physics 1908 for colour photography**. *Europhysics News*, **39**(6):18–22, 2008. 1

[14] D. Collins. *The story of Kodak.* H N Abrams Pub, 1990. 2

[15] W. Matusik and H. Pfister. **3D TV: a scalable system for real-time acquisition, transmission, and autostereoscopic display of dynamic scenes**. *ACM Trans. Graph.*, **23**:814–824, 2004. 2

[16] S. Pastoor and M. Wöpking. **3-D displays: A review of current technologies**. *Displays*, **17**(2):100–110, 1997. 2

[17] P. Benzie, J. Watson, P. Surman, I. Rakkolainen, K. Hopf, H. Urey, V. Sainov, and C. von Kopylow. **A Survey of 3DTV Displays: Techniques and Technologies**. *IEEE Trans. Circuits Syst. Video Technol*, **17**(11):1647–1658, 2007. 2

[18] T.C. Poon. *Digital holography and three-dimensional display: principles and applications.* Springer, 2006. 2, 3

[19] I. Sexton and P. Surman. **Stereoscopic and autostereoscopic display systems**. *IEEE Sig. Proc. Mag.*, **16**(3):85–99, 1999. 2

[20] J.P. Wann, S. Rushton, and M.M. Williams. **Natural problems for stereoscopic depth perception in virtual environments**. *Vision Res.*, **35**(19):2731 – 2736, 1995. 2

[21] D. Gabor. **Microscopy by reconstructed wavefronts**. *Proc. R. Soc. London, Ser. A*, **197**(1051):454–487, 1949. 2, 4

[22] G. Faigel and M. Tegze. **X-ray holography**. *Reports on Progress in Physics*, **62**:355, 1999. 2

[23] M. Tegze and G. Faigel. **X-ray holography with atomic resolution**. *Nature*, **380**:49–51, 1996. 2

[24] H. Lichte. **Electron holography approaching atomic resolution**. *Ultramicroscopy*, **20**(3):293–304, 1986. 2

[25] P. Korecki, G. Materlik, and J. Korecki. **Complex γ-ray hologram: solution to twin images problem in atomic resolution imaging**. *Phys. Rev. Lett.*, **86**(8):1534–1537, 2001. 2

[26] P. Korecki, J. Korecki, and T. Śle, zak. **Atomic resolution γ-ray holography using the Mössbauer effect**. *Phys. Rev. Lett.*, **79**(18):3518–3521, 1997. 2

[27] WL Bragg and G.L. Rogers. **Elimination of the unwanted image in diffraction microscopy**. *Nature*, **167**:190–191, 1951. 2

[28] P. Kirkpatrick and H. El-Sum. **Image formation by reconstructed wave fronts. I. Physical principles and methods of refinement**. *J. Opt. Soc. Am.*, **46**(10):825–830, 1956. 2

[29] B.M. Hennelly, D.P. Kelly, N. Pandey, and D.S. Monaghan. **Review of Twin Reduction and Twin Removal Techniques in Holography**. *Proceedngs of China-Ireland onference on information and communication technology, 2009, NUI Maynooth.* 3

[30] E.N. Leith and J. Upatnieks. **Reconstructed wavefronts and communication theory**. *J. Opt. Soc. Am.*, **52**(10):1123–1128, 1962. 3, 31

[31] A. Lohmann. **Optische Einseitenband ”ubertragung angewandt auf das Gabor-Mikroskop**. *J Mod. Opt*, **3**(2):97–99, 1956. 3

[32] A.W. Lohmann. **A pre-history of computer-generated holography**. *Optics and Photonics News*, **19**(2):36–47, 2008. 3

[33] E.N. Leith and J. Upatnieks. **Wavefront reconstruction with diffused illumination and three-dimensional objects**. *J. Opt. Soc. Am.*, **54**(11):1295–1301, 1964. 3

[34] L. Mandel. **Color imagery by wavefront reconstruction**. *J. Opt. Soc. Am.*, **55**(12):1697–1698, 1965. 3

[35] K.S. Pennington and L.H. Lin. **Multicolor wavefront reconstruction**. *Appl. Phys. Lett.*, **7**:56, 1965. 3

[36] H.I. Bjelkhagen, J. Chang, and K. Moneke. **High-resolution contact Denisyuk holography**. *Appl. Opt.*, **31**(8):1041–1047, 1992. 3

[37] S.A. Benton, S.M. Birner, and A. Shirakura. **Edge-lit rainbow holograms**. In *Proc. SPIE*, **1212**, page 149, 1990. 3

[38] R.F. Vanligten. **Influence of Photographic Film on Wavefront Reconstruction. I. Plane Wavefronts**. *J. Opt. Soc. Am.*, **56**(1):1–6, 1966. 3

[39] D.H. Kelly. **Systems analysis of the photographic process. I. A three-stage model**. *J. Opt. Soc. Am.*, **50**(3):269, 1960. 3

[40] W.K. Smothers, B.M. Monroe, A.M. Weber, and D.E. Keys. **Photopolymers for holography**. *Practical Holography IV*, **1212**(1):20–29, 1990. 3

[41] P. Günter. **Holography, coherent light amplification and optical phase conjugation with photorefractive materials**. *Phys. Rep.*, **93**(4):199–299, 1982. 3

[42] D. Oesterhelt, C. Bruchle, and N. Hampp. **Bacteriorhodopsin: a biological material for information processing**. *Quarterly Reviews of Biophysics*, **24**(04):425–478, 1991. 3

[43] J.W. Goodman and R.W. Lawrence. **Digital image formation from electronically detected holograms**. *Appl. Phys. Lett.*, **11**:77, 1967. 3

[44] M.A. Kronrod, N.S. Merzlyakov, and L.P. Yaroslavskii. **Reconstruction of a hologram with a computer**. *SPIE milestone series*, **144**:645–646, 1998. 3

[45] L.P. Yaroslavskii and N.S. Merzlyakov. *Methods of digital holography*. Consultants Bureau, 1980. 3

[46] U. Schnars and W. Jüptner. **Direct recording of holograms by a CCD target and numerical reconstruction**. *Appl. Opt.*, **33**(2):179–181, 1994. 3, 12, 35, 37

[47] D.H. Close. **Holographic optical elements**. *Opt. Eng.*, **14**:408–419, 1975. 3

[48] J. Ashley, M.P. Bernal, G.W. Burr, H. Coufal, H. Guenther, J.A. Hoffnagle, C.M. Jefferson, B. Marcus, R.M. Macfarlane, and R.M. Shelby. **Holographic data storage**. *IBM J. Res. Develop*, **44**(3):341–368, 2000. 3

[49] A.A. Sawchuk and T.C. Strand. **Digital optical computing**. *Proc. IEEE*, **72**(7):758–779, 1984. 3

[50] G. Pedrini, Y.L. Zou, and H.J. Tiziani. **Digital double-pulsed holographic interferometry for vibration analysis**. *J. Mod. Opt.*, **42**(2):367–374, 1995. 3

[51] G. Pedrini, P. Froning, H. Fessler, and H.J. Tiziani. **In-line digital holographic interferometry**. *Appl. Opt.*, **37**(26):6262–6269, 1998. 3

[52] T. Baumbach, W. Osten, C. von Kopylow, and W. Jüptner. **Remote metrology by comparative digital holography**. *Appl. Opt.*, **45**(5):925–934, 2006. 3

[53] T. Colomb, J. Kühn, F. Charriere, C. Depeursinge, P. Marquet, and N. Aspert. **Total aberrations compensation in digital holographic microscopy with a reference conjugated hologram**. *Opt. Exp.*, **14**(10):4300–4306, 2006. 3

[54] P. Marquet, B. Rappaz, P.J. Magistretti, E. Cuche, Y. Emery, T. Colomb, and C. Depeursinge. **Digital holographic microscopy: a noninvasive contrast imaging technique allowing quantitative visualization of living cells with subwavelength axial accuracy**. *Opt. Lett.*, **30**(5):468–470, 2005. 3, 86

[55] L. Onural. **Television in 3-D: What Are the Prospects?** *Proc. IEEE*, **95**(6):1143–1145, 2007. 3

[56] L. Onural, T. Sikora, J. Ostermann, A. Smolic, R. Civanlar, and J. Watson. **An assessment of 3DTV technologies**. *Proc. NAB*, page 456, 2006. 3

[57] Monaghan D.S. Pandey N. Kozacki T. Michakiewicz A. Finke G. Hennelly B. Kelly, D.P. and M. Kujawinska. **Digital Holographic Capture and Optoelectronic Reconstruction for 3D Displays**. *Int. J. Dig. Multimedia Broadcasting*, **2010**, 2010. 4, 140

[58] D.P. Kelly, B.M. Hennelly, N. Pandey, T.J. Naughton, and W.T. Rhodes. **Resolution limits in practical digital holographic systems**. *Opt. Eng.*, **48**:095801, 2009. 4, 5, 21, 140

[59] D.S. Monaghan, D.P. Kelly, N. Pandey, and B.M. Hennelly. **Twin removal in digital holography using diffuse illumination**. *Opt. Lett.*, **34**(23):3610–3612, 2009. 4, 5, 109, 140

[60] N. Pandey and B. Hennelly. **Compensation of reference beam sphericity in a multi-perspective digital holography based record-display setup.** *Proc. SPIE*, **8082**, 2011. 4, 140

[61] N. Pandey and B. Hennelly. **Memory efficient noise reduction in in-line Fresnel digital holography**. *Proc. SPIE*, **8074**, 2011. 4, 5, 108, 140

[62] J.W. Goodman. *Introduction to Fourier optics.* Roberts & Company Publishers, 2005. 7, 12, 15, 40

[63] M. Born and E. Wolf. *Principles of Optics: Electromagnetic Theory of Propagation, Interference, and Diffraction of Light*. Cambridge University Press, Cambridge, UK, 1999. 8, 10, 34

[64] J.D. Jackson. *Classical electrodynamics*. Wiley, New York, 1975. 8

[65] R.P. Feynman. *Feynman lectures on physics. Volume 2: Mainly electromagnetism and matter*. Addison-Wesley, Reading, MA, 1964. 8

[66] D.A. Fleisch. *A student's guide to Maxwell's equations*. Cambridge Univ Press, 2008. 8

[67] T.L. Dimitrova and A. Weis. **The wave-particle duality of light: A demonstration experiment**. *Am. J. Phys.*, **76**:137, 2008. 8

[68] M. Born, E. Wolf, and A.B. Bhatia. *Principles of optics*, **508**. Pergamon press, Oxford, 1975. 11

[69] E. Hecht and A. Zajac. **Optics (Addison-Wesley series in physics)**. 1974. 11

[70] J.W. Goodman. *Speckle phenomena in optics: theory and applications*. Roberts & Co, 2007. 12, 18, 83, 86, 92, 123, 127

[71] C. Fournier, L. Denis, and T. Fournel. **On the single point resolution of on-axis digital holography**. *J. Opt. Soc. Am. A*, **27**(8):1856–1862, 2010. 21

[72] C. Van Loan. *Computational frameworks for the fast Fourier transform*. Society for Industrial Mathematics, 1992. 24, 54, 55

[73] J.C. Dainty. **Laser speckle and related phenomena**. In *Berlin and New York, Springer-Verlag (Topics in Applied Physics. Volume 9), 1975. 298 p*, **9**, 1975. 35, 37

[74] R. Jones and C. Wykes. **Holographic and speckle interferometry**. *Holographic and Speckle Interferometry, by Robert Jones and Catherine Wykes, pp. 368. ISBN 0521348781. Cambridge, UK: Cambridge University Press, March 1989.*, **1**, 1989. 35

[75] J. Dainty. **Stellar speckle interferometry**. *Laser speckle and related phenomena*, pages 255–280, 1975. 35

[76] L.H. Tanner. **Camera testing by use of speckle patterns**. *Appl. Opt.*, **13**(9):2026–2034, 1974. 35

[77] P. Castellini, G.M. Revel, and E.P. Tomasini. **Laser Doppler vibrometry: a review of advances and applications**. *Shock Vib. Digest*, **30**(6):443–456, 1998. 35

[78] J.W. Goodman. *Speckle phenomena in optics: theory and applications*. Roberts & Company, 2007. 35, 99

[79] J.S. Lim and H. Nawab. **Techniques for speckle noise removal**. *Opt. Eng.*, **20**:472–480, 1981. 37, 108

[80] T.R. Crimmins. **Geometric filter for speckle reduction**. *Appl. Opt.*, **24**(10):1438–1443, 1985. 37, 108

[81] J. Maycock, B.M. Hennelly, J.B. McDonald, Y. Frauel, A. Castro, B. Javidi, and T.J. Naughton. **Reduction of speckle in digital holography by discrete Fourier filtering**. *J. Opt. Soc. Am.*, **24**(6):1617–1622, 2007. 37, 108

[82] I. Yamaguchi and T. Zhang. **Phase-shifting digital holography**. *Opt. Lett.*, **22**(16):1268–1270, 1997. 43

[83] A.J. Page, L. Ahrenberg, and T.J. Naughton. **Low memory distributed reconstruction of large digital holograms**. *Opt. Exp.*, **16**(3):1990–1995, 2008. 51

[84] L. Ahrenberg, A.J. Page, B.M. Hennelly, J.B. McDonald, and T.J. Naughton. **Using commodity graphics hardware for real-time digital hologram view-reconstruction**. *J. Disp. Tech.*, **5**(4):111–119, 2009. 51

[85] H. Kang, F. Yaraş, and L. Onural. **Graphics processing unit accelerated computation of digital holograms**. *Appl. Opt.*, **48**(34):H137–H143, 2009. 51

[86] K.B. Cullen, G.C.M Silvestre, and N. Hurley. **Simulation of DSP algorithms on fixed point architectures**. In *Acoustics, Speech ans Signal Processing,. Proceedings of.(ICASSP' 05)*, **5**. IEEE, 2005. 52

[87] J.G. Sucerquia, W. Xu, S.K. Jericho, P. Klages, M.H. Jericho, and H. J. Kreuzer. **Digital in-line holographic microscopy**. *Appl. Opt.*, **45**(5):836–850, 2006. 52

[88] S. Seo, T.W. Su, D.K. Tseng, A. Erlinger, and A. Ozcan. **Lensfree holographic imaging for on-chip cytometry and diagnostics**. *Lab on a Chip*, **9**(6):777–787, 2008. 52

[89] E. Malkiel, O. Alquaddoomi, and J. Katz. **Measurements of plankton distribution in the ocean using submersible holography**. *Meas. Sci. Technol.*, **10**:1142, 1999. 52

[90] D. Hough. **Applications of the Proposed IEEE 754 Standard for Floating-Point Arithetic**. *Computer*, **14**(3):70–74, 1981. 52

[91] D. Goldberg. **What every computer scientist should know about floating-point arithmetic**. *ACM Comput. Surveys.*, **23**(1):5–48, 1991. 53

[92] T.J. Naughton, Y. Frauel, B. Javidi, and E. Tajahuerce. **Compression of digital holograms for three-dimensional object reconstruction and recognition**. *Appl. Opt.*, **41**(20):4124–4132, 2002. 54, 70

[93] G.A. Mills and I. Yamaguchi. **Effects of quantization in phase-shifting digital holography**. *Appl. Opt.*, **44**(7):1216–1225, 2005. 54, 71

[94] D. Kerr, G.H. Kaufmann, and G.E. Galizzi. **Unwrapping of interferometric phase-fringe maps by the discrete cosine transform**. *Appl. Opt.*, **35**(5):810–816, 1996. 55

[95] A.V. Aho and J.E. Hopcroft. *Design & Analysis Of Computer Algorithms*. Pearson Education India, 1974. 55

[96] E. Buckley. **Holographic laser projection technology**. *SID Int. Symp. Digest Tech*, pages 1074–1079, 2008. 62

REFERENCES

[97] A. Feldspar. **An explanation of the deflate algorithm**. *URL: http://www. gzip. org/zlib/feldspar. html.* 64

[98] T.J. Naughton, J.B. McDonald, and B. Javidi. **Efficient compression of Fresnel fields for Internet transmission of three-dimensional images**. *Appl. Opt.*, **42**(23):4758–4764, 2003. 70

[99] T.J. Naughton and B. Javidi. **Compression of encrypted three-dimensional objects using digital holography**. *Opt. Eng.*, **43**:2233, 2004. 70

[100] O. Matoba, T.J. Naughton, Y. Frauel, N. Bertaux, and B. Javidi. **Real-time three-dimensional object reconstruction by use of a phase-encoded digital hologram**. *Appl. Opt.*, **41**(29):6187–6192, 2002. 70

[101] A.E. Shortt, T.J. Naughton, and B. Javidi. **A companding approach for nonuniform quantization of digital holograms of three-dimensional objects**. *Opt. Exp.*, **14**(12):5129–5134, 2006. 71

[102] A.E. Shortt, T.J. Naughton, and B. Javidi. **Compression of Optically Encrypted Digital Holograms Using Artificial Neural Networks**. *J. Disp. Tech.*, **2**(4):401–410, 2006. 71

[103] A. Shortt, T.J. Naughton, and B. Javidi. **Compression of digital holograms of three-dimensional objects using wavelets**. *Opt. Exp.*, **14**(7):2625–2630, 2006. 71

[104] E. Darakis and J.J. Soraghan. **Reconstruction domain compression of phase-shifting digital holograms**. *Appl. Opt.*, **46**:351–356, 2007. 71

[105] E. Darakis, T.J. Naughton, and J.J. Soraghan. **Compression defects in different reconstructions from phase-shifting digital holographic data**. *Appl. Opt.*, **46**(21):4579–4586, 2007. 71

[106] A. Gotchev and L. Onural. **A survey on sampling and quantization in diffraction and holography**. In *Workshop on Spectral Methods and Multirate Signal Processing, SMMSP*, pages 179–190, 2006. 71

[107] D. Psaltis, E.G. Paek, and S.S. Venkatesh. **Optical image correlation with a binary spatial light modulator**. *SPIE Milestone Series*, **156**:482–488, 1999. 71

[108] B. Javidi and J.L. Horner. **Single spatial light modulator joint transform correlator**. *Appl. Opt.*, **28**(5):1027–1032, 1989. 71

[109] A. Bourquard, F. Aguet, and M. Unser. **Optical imaging using binary sensors**. *Opt. Exp.*, **18**(5):4876–4888, Mar 2010. 71

[110] W.J. Dallas and A.W. Lohmann. **Phase quantization in holograms-depth effects**. *Appl. Opt.*, **11**(1):192–194, 1972. 71

[111] A.W. Lohmann and D.P. Paris. **Binary Fraunhofer Holograms, Generated by Computer**. *Appl. Opt.*, **6**(10):1739–1748, 1967. 71

[112] F. Wyrowski. **Iterative quantization of digital amplitude holograms**. *Appl. Opt.*, **28**(18):3864–3870, 1989. 71

[113] R.S. Powers and J.W. Goodman. **Error rates in computer-generated holographic memories**. *Appl. Opt.*, **14**(7):1690–1701, 1975. 71

[114] P.S. Naidu. **Quantization noise in binary holograms**. *Opt. Comm.*, **15**(3):361–365, 1975. 71

[115] M.A. Seldowitz, J.P. Allebach, and D.W. Sweeney. **Synthesis of digital holograms by direct binary search**. *Appl. Opt.*, **26**(14):2788–2798, 1987. 71

[116] A.V. Oppenheim and R.W. Schafer. *Discrete-time signal processing.* Upper Saddle River, NJ: Prentice-Hall, 1999. 75

[117] L. Schuchman. **Dither signals and their effect on quantization noise**. *IEEE Trans. Commun.*, **12**(4):162–165, 1964. 79

[118] A. Sripad and D. Snyder. **A necessary and sufficient condition for quantization errors to be uniform and white**. *IEEE Trans. Acoust, Sp. Sig. Proc.*, **25**(5):442–448, 1977. 79

[119] J. Schoukens and J. Renneboog. **Modeling the noise influence on the Fourier coefficients after a discrete Fourier transform**. *IEEE Trans. Instrum. Meas.*, **35**(3):278–286, 1986. 83

[120] R. Shiavi. *Introduction to applied statistical signal analysis: guide to biomedical and electrical engineering applications.* Academic Press, 2007. 83

[121] O.A. Skydan, F. Lilley, M.J. Lalor, and D.R. Burton. **Quantization Error of CCD Cameras and Their Influence on Phase Calculation in Fringe Pattern Analysis**. *Appl. Opt.*, **42**(26):5302–5307, 2003. 84

[122] H. Gudbjartsson and S. Patz. **The Rician distribution of noisy MRI data**. *Mag. Res. Med.*, **34**(6):910–914, 1995. 86, 100

[123] D. Middleton. *An introduction to statistical communication theory.* McGraw-Hill New York, 1960. 87, 99

[124] J. Maycock, C.M. Elhinney, B.M. Hennelly, T.J. Naughton, J. McDonald, and B. Javidi. **Three-dimensional scene reconstruction of partially occluded objects using digital holograms**. *Appl. Opt.*, **45**:2975–2985, 2006. 92

[125] E. Buckley. **Holographic laser projection technology**. *SID Int. Symp. Digest Tech*, pages 1074–1079, 2008. 92, 109

[126] W.B. Davenport Jr, W.L. Root, and G. Weiss. *An introduction to the theory of random signals and noise.* McGraw-Hill Book Company, New York. 93, 102

[127] F. Charrière, T. Colomb, F. Montfort, E. Cuche, P. Marquet, and C. Depeursinge. **Shot-noise influence on the reconstructed phase image signal-to-noise ratio in digital holographic microscopy**. *Appl. Opt.*, **45**(29):7667–7673, 2006. 93, 101, 103, 105, 139

[128] F. Charrière, B. Rappaz, J. Kuhn, T. Colomb, P. Marquet, and C. Depeursinge. **Influence of shot noise on phase measurement accuracy in digital holographic microscopy**. *Opt. Exp.*, **15**(14):8818–8831, 2007. 93, 94, 101

[129] M. Gross and M. Atlan. **Digital holography with ultimate sensitivity**. *Opt. Lett.*, **32**(8):909–911, 2007. 94

[130] M. Yamamoto, H. Yamamoto, and Y. Hayasaki. **Photon-counting digital holography under ultraweak illumination**. *Opt. Lett.*, **34**(7):1081–1083, 2009. 94

[131] T. Colomb, F. Montfort, and C. Depeursinge. **Small Reconstruction Distance in Convolution Formalism**. *Digital Holography and Three-Dimensional Imaging, OSA Technical Digest, paper DMA4*, 2008. 97

[132] B.M. Hennelly and J.T. Sheridan. **Generalizing, optimizing, and inventing numerical algorithms for the fractional Fourier, Fresnel, and linear canonical transforms**. *J. Opt. Soc. Am. A*, **22**(5):917–927, 2005. 97

[133] B.P. Lathi. *Modern digital and analog communication systems*. Oxford University Press, Inc. New York, NY, USA, 1995. 100

[134] J.H. Ahrens and U. Dieter. **Computer methods for sampling from gamma, beta, poisson and bionomial distributions**. *Computing*, **12**(3):223–246, 1974. 102

[135] J. Lukas, J. Fridrich, and M. Goljan. **Digital camera identification from sensor pattern noise**. *IEEE Trans. Inform. Forensics Security.*, **1**(2):205–214, 2006. 107

[136] M. Ryle, A. Hewish, and J. Shakeshaft. **The synthesis of large radio telescopes by the use of radio interferometers**. *IRE Trans. Antennas Propag.*, **7**(5):120–124, 1959. 120

[137] P.A. Rosen, S. Hensley, I.R. Joughin, F.K. Li, S.N. Madsen, E. Rodriguez, and R.M. Goldstein. **Synthetic aperture radar interferometry**. *Proc. IEEE*, **88**(3):333–382, 2000. 120

[138] T. Sato, M. Ueda, and S. Fukuda. **Synthetic aperture sonar**. *J. Acoust. Soc. Am.*, **54**(3):799–802, 1973. 120

[139] J. Vrba and S.E. Robinson. **Signal Processing in Magnetoencephalography**. *Methods*, **25**(2):249–271, 2001. 120

[140] J.W. Goodman. **I. Synthetic-Aperture Optics**. *Progress in Optics*, **8**:1 – 50, 1970. 120

[141] J.H. Massig. **Digital off-axis holography with a synthetic aperture**. *Opt. Lett.*, **27**(24):2179–2181, 2002. 120, 131

[142] R. Binet, J. Colineau, and J.C. Lehureau. **Short-Range Synthetic Aperture Imaging at 633 nm by Digital Holography**. *Appl. Opt.*, **41**(23):4775–4782, 2002. 120

[143] B.M. Hennelly, T.J. Naughton, J.B. McDonald, Y. Frauel, and B. Javidi. **A method for super-resolution in digital holography**. **6311**, page 63110J. SPIE, 2006. 120, 122

[144] J. Di, J. Zhao, H. Jiang, P. Zhang, Q. Fan, and W. Sun. **High resolution digital holographic microscopy with a wide field of view based on a synthetic aperture technique and use of linear CCD scanning**. *Appl. Opt.*, **47**(30):5654–5659, 2008. 121

[145] T. Kreis and K. Schlüter. **Resolution enhancement by aperture synthesis in digital holography**. *Opt. Eng.*, **46**(5):055803, 2007. 121

[146] S. A. Alexandrov, T. R. Hillman, T. Gutzler, and David D. Sampson. **Synthetic Aperture Fourier Holographic Optical Microscopy**. *Phys. Rev. Lett.*, **97**(16):168102, 2006. 121

[147] Y. Zhang, X. Lu, Y. Luo, L. Zhong, and C. She. **Synthetic aperture holography by movement of object**. *Proc. SPIE*, **5636**, 2005. 122

Declaration

I herewith declare that I have produced this thesis without the prohibited assistance of third parties and without making use of aids other than those specified; notions taken over directly or indirectly from other sources have been identified as such. This thesis has not previously been presented in identical or similar form to any other Irish or foreign examination board.

The thesis work was conducted from October 2008 to June 2011 under the supervision of Dr.Bryan Hennelly at National University of Ireland.

Maynooth, Co.Kildare, Ireland